

Copyright

by

Hong Liu

2012

The Dissertation Committee for Hong Liu certifies that this
is the approved version of the following dissertation:

**Simple and Inexpensive Biosensors for Point-of-Care
Diagnostics**

Committee:

Richard M. Crooks, Supervisor

Allen J. Bard

Keith J. Stevenson

Eric V. Anslyn

John X.J. Zhang

**Simple and Inexpensive Biosensors for Point-of-Care
Diagnostics**

by

Hong Liu, B.S.; M.S.

Dissertation

Presented to the Faculty of the Graduate School of

The University of Texas at Austin

in Partial Fulfillment

of the Requirements

for the Degree of

Doctor of Philosophy

The University of Texas at Austin

December, 2012

Dedication

To my wife,
Ningyan Miao
and my daughter,
Yi Liu

Acknowledgements

I would like to sincerely thank my research advisor, Dr. Richard M. Crooks for his generous support over my entire graduate study. It has been great privilege for me to work in his laboratory. This experience is invaluable to me and my future career. His encouragement was the most important factor leading to many fruitful developments.

I would also like to thank Dr. Allen J. Bard, Dr. Keith J. Stevenson, Dr. Eric V. Anslyn, and Dr. John X. J. Zhang for being my committee members and helping me to finish my graduate study.

My gratitude goes to Dr. Kwok-Fan Chow, Stephen Fosdick, Dr. Christophe Renault, Dr. Xiaole Chen, Dr. Damon Smith, Dr. Ian Richards, Dr. Antonio Ricco, Dr. Bingling Li, Dr. Xiang Yu, Alexandra Gade and Angie Missildine for assisting me in my graduate research. Special thanks go to my fellow Crooks group members for their assistance in the laboratory.

Last but not least, I want to thank my lovely wife, daughter as well as our family for their undying support throughout my studies.

**Simple and Inexpensive Biosensors for Point-of-Care
Diagnostics**

Publication No. _____

Hong Liu, Ph. D.

The University of Texas at Austin, 2012

Supervisor: Richard M. Crooks

In this dissertation, three types of paper-based analytical devices for point-of-care biosensing, a potentiometric method for analyzing percent hemoglobin A1c (%HbA1c) and a PDMS-glass microelectrochemical device for highly reproducible amperometric measurement in microdroplet, are described.

The first paper-based sensing device is fabricated using the principles of origami (paper folding). The three-dimensional origami paper analytical device (oPAD) is fabricated on a single sheet of flat paper in a single photolithographic step and assembled by simply folding the paper by hand. Following analysis, the device can be

unfolded to reveal each layer for optical and fluorescent read-out.

The second type of paper-based device has an integral aluminum/air battery as the power source and reports its output using Prussian blue as an electrochromic indicator. The integrated aluminum/air battery powers both the electrochemical sensor and the electrochromic read-out. The applicability of the device to point-of-care sensing is demonstrated by qualitative detection of glucose and H_2O_2 in artificial urine.

The third type of paper-based device (oPAD 2) uses an aptamer to recognize the analyte, adenosine, a glucose oxidase tag to modify the relative concentrations of an electroactive redox couple, and a digital multimeter to transduce the result of the assay. Adenosine is quantitatively determined using this device with a detection limit of 11.8 μM .

The method for measuring HbA1c concentration, hemoglobin concentration, and thus %HbA1c in human blood is based on potentiometry. We use Alizarin red s (ARS) as a redox indicator. The potential shift of ARS owing to diol-boronic acid complexation is used to determine the HbA1c, which is a competitor of ARS for the complexation reaction. The concentration of Hb is determined by reacting it with

$\text{Fe}(\text{CN})_6^{3-}$ and measuring the potential shift arising from the reduction of $\text{Fe}(\text{CN})_6^{3-}$ by Hb. The results obtained for %HBA1c in human blood are in good agreement with those determined using a reference method.

The method for highly reproducible chronoamperometric analysis of the contents of microdroplets is developed. Aqueous microdroplets (~ 1 nL) and separated by a fluorocarbon solvent are generated within a microfluidic device using a T-shaped junction. Highly reproducible quasi-steady-state currents (relative standard deviations = ~ 2%) are observed when the microdroplets are stretched by a factor of 10 in a narrowed segment of a microchannel, which leads to desirable intradroplet mass transfer characteristics. Importantly, the design of the microelectrochemical device ensures direct contact between intradroplet redox molecules and the electrode surface to study inner-sphere electrocatalytic processes such as the oxygen reduction reaction. Finite-element simulations are presented that are in accord with the experimental findings.

Table of Contents

Chapter 1: Introduction.....	1
1.1 Paper-based analytical devices.....	1
1.2 Point-of-care diagnosis of diabetes.....	5
1.3 Microdroplets.....	7
1.4 Research summary and accomplishments.....	10
Chapter 2: Experimental.....	13
2.1 Chemicals.....	13
2.2 Techniques.....	13
Chapter 3: Fabrication of three-dimensional paper fluidic device using the principle of origami.....	16
3.1 Synopsis.....	16
3.2 Introduction.....	16
3.3 Experimental.....	20
3.4 Results and Discussion.....	24
3.5 Summary and Conclusion.....	37
Chapter 4: Paper-Based Electrochemical Sensing Platform with Integral Battery and Electrochromic Read- Out.....	38
4.1 Synopsis.....	38
4.2 Introduction.....	38
4.3 Experimental.....	43
4.4 Results and Discussion.....	46

4.5	Summary and Conclusion.....	57
Chapter 5: Aptamer-based Origami Paper Analytical Device for		
	Electrochemical Detection of adenosine.....	59
5.1	Synopsis.....	59
5.2	Introduction.....	60
5.3	Experimental.....	64
5.4	Results and Discussion.....	71
5.5	Summary and Conclusion.....	83
Chapter 6: Determination of Percent Hemoglobin A1c Using a		
	Potentiometric Method.....	85
6.1	Synopsis.....	85
6.2	Introduction.....	85
6.3	Experimental.....	88
6.4	Results and Discussion.....	91
6.5	Summary and Conclusion.....	112
Chapter 7: Highly Reproducible Chronoamperometric Analysis		
	in Microdroplets.....	113
7.1	Synopsis.....	113
7.2	Introduction.....	114
7.3	Experimental.....	119
7.4	Results and Discussion.....	121
7.5	Summary and Conclusion.....	143
Chapter 8: Summary and Conclusion.....		
		145
References.....		
		148

Vita.....	167
-----------	-----

Chapter 1: Introduction

1.1 Paper-based analytical devices

Paper is a thin material made by pressing moist fibers (e.g., cellulose pulp) and drying them into flexible sheets. The making process of the material recognizable as paper in modern times was invented by a Chinese named Lun Cai in the early 2nd century AD.¹ Now it has been widely used in almost all aspects of human life, for example, writing, printing, cleaning, packaging. Paper made from cellulose is a renewable material with annual production of 1.5×10^{12} tons.² It is also one of the cheapest materials all over the world.

The unique features of paper in terms of analytical chemistry are: (1) Paper is a porous hydrophilic material so that it wicks fluid, which facilitates the manipulation of liquid sample without using a pump or a pipette. (2) Due to well-established printing techniques, patterning paper is much easier than patterning other thin materials. This makes mass production of paper-based analytical devices practically feasible. (3) Paper is a biocompatible material so that biomolecule probes are more stable and less likely to denature on paper. (4) Paper is also chemically inert so that it doesn't interfere with most analytical processes.

The simplest and earliest paper-based analytical devices is probably litmus paper, which was invented by a French chemist, J.L. Gay-Lussac, in the 1800s.³ The working principle of the litmus paper is quite similar to that of the microfluidic paper analytical devices (μ PADs) recently invented by Whitesides and coworkers.⁴ The filter paper,³ or patterned chromatography paper,⁴ is dipped into a liquid sample, the preloaded reagents on the paper are dissolved by the sample, and the reagents react with the analyte (e.g. protons or glucose) to develop colors which are correlate to the concentration of the analyte. Owing to the simple users' experience of "dip-and-read", paper-based analytical devices are especially suitable for point-of-care diagnostics.⁵ By careful engineering of the paper-based analytical devices, more sophisticated bioassays that involve specific binding reaction have also been achieved on paper with high sensitivity (i.e., sub-nM) and good reproducibility. For example, in 1988, a nitrocellulose-based lateral-flow immunochromatographic assay was developed by Unipath for point-of-care pregnancy testing, which turns out to be a great commercial success.⁵

The origin of using patterned paper as a platform for analytical chemistry is probably the work reported by Müller and coworkers.⁶ In 1949, they studied the elution of a

pigment mixture along a fluidic channel of filter paper which was patterned using paraffin wax. The paraffin wax was patterned on the filter paper by selectively applying heat to melt wax and the wax wicked into the paper. After cooling to room temperature, the wax formed a hydrophobic barrier to guide the wicking of sample liquid in the remaining paper channel. In 2007, Whitesides and coworkers developed a photolithographic method to pattern chromatography paper and the resulting two-dimensional (2-D) μ PADs were used for colorimetric detection of glucose and bovine serum albumin.⁴ Since then, a wide range of paper-patterning techniques have been developed for fabricating 2-D μ PADs, including plotting,⁷ ink-jet etching,⁸ plasma treatment,⁹ wax printing,^{10,11} inkjet printing,¹² Flexography printing,¹³ screen printing¹⁴ and laser treatment.¹⁵

In 2009, Whitesides and coworkers fabricated three-dimensional (3-D) μ PADs by stacking of 2-D μ PADs using double sided tape.¹⁶ A laser cutter was used to punch holes and the holes were filled with cellulose powders to enable vertical connections between paper channels on adjacent layers. However, the fabrication of this 3-D device is very complicated, and it involves the use of an expensive laser

cutter, which limits the mass production capability of this device.

According to World Health Organization, point-of-care analytical devices for developing world need to be ASSURED, which is Affordable, Sensitive, Specific, User-friendly, Rapid and robust, Equipment-free and Deliverable to end-users.¹⁷ Due to the requirement of equipment-free, colorimetric read-out, which enables naked-eye detection, was exclusively used at the beginning of this technique.^{4 16-}
¹⁸ However, the key limitation of the colorimetric read-out for a paper-based analytical device is the poor sensitivity and the difficulty of achieving quantitative analysis. The poor sensitivity is partially due to the short optical path of paper (e.g. $\sim 180 \mu\text{m}$) so that the absorption of light is very small and can not be seen by human eyes unless a high concentration of chromophore is generated. To achieve quantitative analysis, an additional optical device (i.e., camera, scanner or colorimeter), appropriate image-processing software, and certain expertise is required, which highly limits the practical application in point-of-care diagnostics.

Electrochemical methods, due to their low cost, low power consumption and simple instrumentation, are especially useful in point-of-care diagnostics.¹⁹ For example, glucose

biosensors, which are mainly electrochemical sensors, account for 85% of the entire biosensor market.²⁰ Unlike colorimetric methods, electrochemical methods are intrinsically quantitative. The first electrochemical paper-based analytical device was reported by Henry and coworkers.²¹ They fabricated three-electrode system on a paper fluidic device by screen printing of carbon and Ag/AgCl conductive ink. Glucose, lactate and uric acid were quantitatively determined on a single device using a traditional electrochemical read-out, a potentiostat. Therefore, the practical application in point-of-care sensing of their device is highly limited by the potentiostat which requires expertise to use. Accordingly, Whitesides and coworkers developed a paper-based electrochemical sensing device that only requires a personal glucose meter (PGM) for readout.²² However, the PGM is engineered to detect blood glucose at physiological concentration (4.4 -6.6 mM).²⁰ The concentration of most biochemical analytes is much smaller than that of glucose (e.g., nM or pM) so that considerable signal amplification is required.

1.2 Point-of-care diagnosis of diabetes

Diabetes, as a group of metabolic diseases, is a

growing worldwide health problem.²³ It is also one of leading causes of death and disability around the world. The metabolic disorder of diabetes is reflected by blood glucose concentrations higher or lower than the normal range of 80-120 mg/dL (4.4-6.6 mM).²⁰ Poor management of blood glucose usually results in numerous complications, including heart attack, renal failure and blindness. Therefore, continuous monitoring blood glucose concentration is crucial for the diagnosis and treatment of diabetes.²⁴

The use of PGM for blood glucose determination requires three to four tests a day due to the large fluctuation of blood glucose concentration.²⁴ For effective diagnosis and management of diabetes, the analysis of percent hemoglobin A1c (%HbA1c), which is the ratio of HbA1c to total hemoglobin (Hb) concentration, is more appropriate.^{25 26} Specifically, the 2010 American Diabetes Association Standards of Medical Care in Diabetes has included %HbA1c \geq 6.5% as a criterion for the diagnosis of diabetes mellitus.²⁷

HbA1c is formed by a nonenzymatic reaction between N-terminal valine of Hb β chain and plasma glucose, followed by an Amadori rearrangement reaction.²⁸ The %HbA1c reflects the average blood glucose concentration over the entire half life of erythrocytes (i.e. 60 days).²⁶

Because of the huge market of diabetes diagnostics (millions of diabetes patients test their blood glucose several times daily),²⁰ the %HbA1c becomes a very attractive model analyte for the development of lots of sensing concepts. A wide range of analytical methods have been developed for the analysis of %HbA1c, including boronate affinity chromatography,^{29,30} ion-exchange chromatography,³¹ electrophoresis,³² fluorescence,^{33,34} UV-vis absorption,³⁴ chemiluminescence,²⁸ electrochemical methods,³⁵⁻³⁹ and immunoassays.^{40,41}

However, most of these methods are based on chromatographic separations. Other methods usually require antibody reagents or commercially unavailable derivatives of boronic acid, which render these methods relatively vulnerable and expensive.^{28,33,34,38,40,41} Moreover, some of these methods only determine the absolute concentration of HbA1c rather than %HbA1c. Finally, it has recently been reported that the majority of commercially available HbA1c analyzers are unreliable.⁴²

1.3 Microdroplets

Microfluidics, as a convenient way to manipulate or process small amounts of liquids (nL to aL) in a microchannel of tens of micrometers, has found a wide range

of applications in chemical and biological research.^{43,44} A decade ago, microdroplets for applications to microfluidics was reported by Quake and coworkers.⁴⁵ Since then, microdroplets have found a myriad of applications solving a number of problems associated with analytical applications of microfluidic systems. For example, due to laminar flow in standard fluidic microchannels, the rate of mixing is limited by diffusional mass transport.^{46,47,48} However, mixing can be accelerated by internal recirculating convection in a flowing microdroplet.⁴⁹ Moreover, the parabolic profile of pressure-driven flow in a microchannel leads to axial Taylor dispersion and thus dilution of reagents.⁵⁰ In contrast, the reagents in a microdroplet are encapsulated in an immiscible organic phase, thereby avoiding dilution. Furthermore, nonspecific adsorption of reagents onto the traditional microfluidic channel walls can be problematic,⁵¹ but this problem is avoided with segmented flow since the aqueous microdroplet does not contact the channel wall. Finally, poly(dimethylsiloxane) (PDMS) is a common material used for fabricating microfluidic devices. The PDMS is vapor permeable and thus may lead to solvent evaporation problems.⁴⁷ This problem can also be solved by the encapsulation of microdroplet using an immiscible liquid.

A number of methods have been reported for analyzing the contents of microdroplets: fluorescence spectroscopy,^{49,52,53} Raman spectroscopy,^{54,55} mass spectrometry,^{56,57} and electrochemical methods.⁵⁸⁻⁶⁰ Compared with the other methods, electrochemistry is relative simple and low cost, and it provides information about mass transfer, electron transfer, and coupled chemical processes that are difficult or impossible to study using the aforementioned approaches.⁶¹ For example, Han et al.⁵⁸ reported on the enzymatic kinetics of catalase confined within microdroplets by detecting H₂O₂ using wire electrodes inserted into the microchannel. In this case, the contact time between the electrodes and the droplets was short, and so the faradaic current was short and convoluted with a large capacitive current. Moreover, the electrode wires were forced to penetrate each droplet, and this resulted in a significant degree of droplet instability. The same group also reported a potentiometric method, using an ion-selective electrode, for studying rapid binding kinetics of Mg²⁺ to RNA in microdroplets.⁶² However, potentiometric measurements were not carried out in droplets, but rather under continuous flow conditions.

Electrochemical measurements in larger (millimeter-scale) droplets have also been reported. For example, Liu et

al.⁵⁹ used chronoamperometry to study droplet size, frequency of droplet generation, and flow velocity of droplets in organic fluid containing redox species. Sassa et al.⁶⁰ used electrode arrays to enhance the sensitivity of coulometric detection of H₂O₂ and L-glutamate in aqueous droplets. However, it would be challenging to do these experiments when the size of the droplets decreased to micrometer scale.

1.4 Research Summary and Accomplishments

My dissertation focuses on the development of simple and inexpensive biosensors for point-of-care diagnostics. Chapters 3, 4, and 5 describe three types of paper-based analytical devices fabricated for biochemical analysis. These paper-based biosensors are very cheap to fabricate and they are all "dip-and-read" sensors which means only two steps are involved for using these sensors. First, dip the device into liquid sample, second, read the results. Therefore, no expertise is required to use these sensors.

Specifically, chapter 3 discusses the fabrication of 3-D paper fluidic analytical devices using the principle of origami. The 3-D origami paper analytical device (oPAD) is fabricated on a single sheet of flat paper in a single photolithographic step and assembled by simply folding the

paper by hand. Following analysis, the device can be unfolded to reveal each layer for optical assays.

Chapter 4 discusses the second type of paper-based device has an integral aluminum/air battery as the power source and reports its output using Prussian blue as an electrochromic indicator. The integrated aluminum/air battery powers both the electrochemical sensor and the electrochromic read-out. The applicability of the device to point-of-care sensing is demonstrated by qualitative detection of 0.1 mM glucose and H_2O_2 in artificial urine.

Chapter 5 discusses the third type of paper-based device (oPAD 2) that uses an aptamer to recognize the analyte, adenosine, a glucose oxidase tag to modify the relative concentrations of an electroactive redox couple, and a digital multimeter to transduce the result of the assay. Adenosine is quantitatively determined using this device with a detection limit of 12 μM .

Chapter 6 describes a method for measuring HbA1c concentration, Hb concentration, and %HbA1c in human blood for diagnosis and management of diabetes mellitus. Alizarin red s (ARS) is used as a potentiometric indicator. Phenylboronic acid (PBA) binds to both ARS and HbA1c via diol-boronic acid complexation. The binding of PBA to ARS shifts its redox potential negative. However, when HbA1c

competes with ARS for PBA binding, the solution potential shifts positive. This shift is linked to the HbA1c concentration. To determinate the concentration of Hb, Hb is allowed to react with $\text{Fe}(\text{CN})_6^{3-}$. The potential shift arising from the reduction of $\text{Fe}(\text{CN})_6^{3-}$ by Hb is proportional to the logarithm of the Hb concentration. The results obtained for %HbA1c in human blood are in good agreement with those determined using a reference method.

Chapter 7 describes a method for highly reproducible chronoamperometric analysis of the contents of microdroplets (~ 1 nL). The key finding is that stable and reproducible quasi-steady-state currents ($\pm \sim 2\%$) are observed if the electrochemical measurements are made in a narrowed segment of a microchannel where the microdroplets are stretched a factor of 10. Importantly, the design of the microelectrochemical device ensures direct contact between intradroplet redox molecules and the electrode surface that enables the study of inner-sphere electrocatalytic processes such as the oxygen reduction reaction. Finite-element simulations are presented that are in accord with the experimental findings.

Chapter 2: Experimental

2.1 Chemicals

All chemicals used in this work are separately described in each chapter.

2.2 Techniques

Photolithography Photolithography uses UV photons to cross link photoresist and generate two-dimensional patterns on a flat substrate.⁶³ The microelectrochemical devices for microdroplet experiments and the oPADs used in this work were fabricated by a contact-mode photolithography.

For fabricating the microelectrochemical device, a conformal photoresist (AZ4670) layer is first spin-coated onto a gold slide having a Cr adhesion layer, and prebaked to remove some solvent. Next, a transparency mask is brought into direct contact with the photoresist layer under a vacuum so that the mask and the photoresist layer on the substrate are in close proximity (e.g. $\sim 1\ \mu\text{m}$). The photoresist is exposed to incident UV light (365 nm, 350 W) so that cross-link reactions is initiated. After rinsing with developing solution, the remaining unexposed photoresist is removed, and the underlying substrate is allowed for further processing. The Au and Cr adhesion

layers are etched subsequently.⁶⁴ All remaining photoresist is then removed by acetone.

For *o*PADs, SU-8 photoresist is patterned on chromatography paper based on a previously reported procedure.⁴ Briefly, the chromatography paper is soaked in diluted photoresist for 5 min. After soft baking at 130 °C for 10 min on a hot plate and cooling to room temperature, the paper is exposed to 365 nm UV light (350 W lamp) for 30 s under a transparency mask. Next, the paper was post baked at 130 °C for 10 min on a hotplate. Finally, the paper was immersed in acetone for 1 min to remove the unexposed photoresist.

Soft lithography The microchannels used in this work are fabricated by soft lithography.⁶³ The mold having the dimensions of the microchannel fabricated by photolithographically cross-linking photoresist coated on a glass slide. The mold is then silanized for microchannel fabrication.

To fabricate the microchannel, the PDMS precursor is first poured onto the photoresist mold. After curing at ~65 °C for 3 h, the PDMS is peeled off from the mold. A hole puncher is used to form the reservoirs at each end of the microchannel. For irreversible binding of the PDMS slab on the glass surface, the PDMS and glass slide are first

treated with air plasma for 15 s. After attachment of the PDMS on the glass slide, the whole device is heated at ~80 °C for 1 min.

Wax printing The patterning of paper using wax printer is based on a slight modification of a procedure reported previously.¹¹ Briefly, a Xerox 8570DN inkjet printer is used to print wax-based solid ink on Whatman chromatography paper. The paper is then placed on a hot plate with the wax side up for 15 s at 120 °C, and then cooled to 20 °C.

Screen printing For fabricating electrodes on a paper-based device, the paper is placed on a flat glass surface, and then covered with a home-made screen with an impermeable pattern on it. An aliquot of carbon ink is dropcast on the paper. A coating blade or rod is used to coat the carbon ink uniformly onto the paper through the screen. To cure the carbon ink, the paper is placed in an oven at 80 °C for 30 min.

Chapter 3: Three-Dimensional Paper Microfluidic Devices Assembled Using the Principles of Origami

3.1 Synopsis

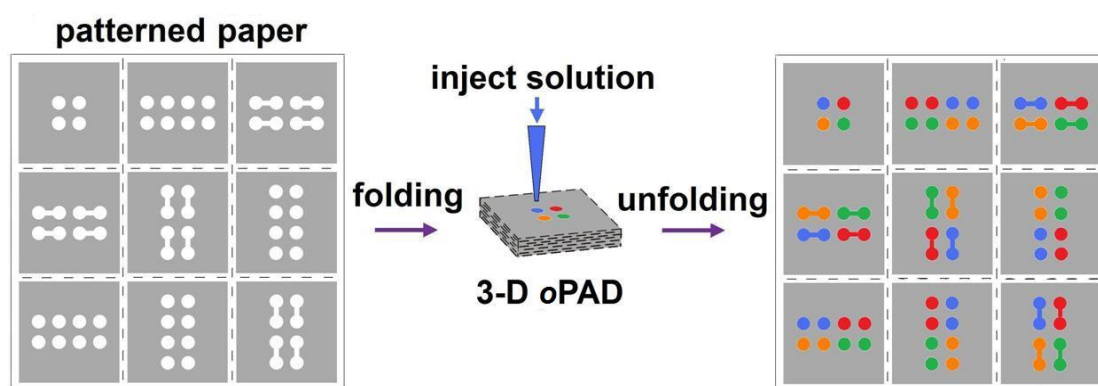
In this chapter we report a method, based on the principles of origami (paper folding), for fabricating three-dimensional (3-D) paper microfluidic devices. The entire 3-D device is fabricated on a single sheet of flat paper in a single photolithographic step. It is assembled by simply folding the paper by hand. Following analysis, the device can be unfolded to reveal each layer. The applicability of the device to chemical analysis is demonstrated by colorimetric and fluorescence detection using multilayer microfluidic network.

3.2 Introduction

In this chapter we report a method for fabricating three-dimensional (3-D) paper microfluidic devices that is based on the principles of origami (paper folding). The concept is illustrated in Scheme 3.1. Using this method, the entire device is fabricated on a single sheet of flat paper, and then it is assembled by simple paper folding. This method is important for several reasons. First, instead of sequential layer-by-layer fabrication, which is the usual

approach for preparing 3-D microfluidic systems,^{16,65,66} the entire device is fabricated on one piece of paper in a single photolithographic step. This speeds the fabrication process and reduces cost. Second, the multilayer device is assembled by simple paper folding, which can be completed in less than 1 min without tools or special alignment techniques. Third, the device can be easily unfolded so that all layers, rather than just the surface, can be used for parallel analysis. Fourth, incorporation of additional intermediate layers should not result in much additional fabrication overhead.

Scheme 3.1



The principles of 2-D and 3-D microfluidic paper analytical devices (μ PADs) have been described by Whitesides and co-workers,^{4,16,18,67,68} and a number of interesting applications have been reported.^{17,18,21,22,67,69,70} Briefly, for 2-D μ PADs, microfluidic channels and reservoirs are fabricated by patterning channel walls on chromatography paper using a hydrophobic material, such as photoresist (PR) or wax. Aqueous solutions are then driven along the hydrophilic paper channels by capillary action. For 3-D μ PADs,^{16,18} individual layers are patterned sequentially by photolithography and then stacked using double-side tape. Holes are punched in the tape using a laser cutter, and the resulting holes are filled with cellulose powder¹⁶ or compressed¹⁸ to provide vertical connections between adjacent layers. The results of an analysis are determined using colorimetric detection on one of the two surface layers. The 3-D μ PADs show great promise for applications such as power-free, point-of-care detection and diagnosis, particularly in underdeveloped or remote areas. However, as presently practiced, device fabrication requires a photolithographic step for each layer and then laser cutting of vias to establish fluidic connections between layers. Moreover, assembly of the device, using double-side tape, is

irreversible so that only the surface layer can be used for colorimetric detection. The approach we describe addresses these points.

As previously discussed, 3-D μ PADs are fabricated by stacking 2-D layers. An alternative approach is based on the principles of origami. Origami is the traditional Japanese art of paper folding, and it has been in use for ~400 years to construct 3-D geometries starting with a single piece of flat paper. Within the context of modern science and engineering, there has not been much interest in origami. However, there is one report in which it was used to fabricate 3-D printed circuit boards in the shapes of airplanes and cranes.⁷¹ With that as a starting point, we show here that origami can be used to fabricate simple and functional microfluidic devices, which we call origami paper analytical devices (μ PADs), having several highly desirable characteristics.

3.3 Experimental

Chemicals Colorimetric glucose (GAGO-20), protein (TP0100) and fluorescent protein assay kits (FP0010) were purchased from Sigma-Aldrich. SU-8 2025 photoresist was obtained from MicroChem Corp. (Newton, MA), and diluted using propylene glycol methyl ether acetate ($\geq 99.5\%$, Sigma-

Aldrich) to 75% v/v for photolithographic patterning on the chromatography paper (Whatman, 1 CHR, 100 μ m thick).

Rhodamine 6G (99%) and erioglaucine disodium salt were purchased from Acros Organics. Tatraine were obtained from MP Biomedicals (Solon, OH). All solutions were prepared with deionized water (18.0 M Ω -cm, Milli-Q Gradient System, Millipore). All reagents were used as received without further purification.

Experimental procedure The patterning of SU-8 photoresist on chromatography paper was based on a previously reported procedure (Martinez, A. W.; Phillips, S. T.; Whitesides, G. M. Proc. Natl. Acad. Sci. U.S.A., 2008, 105, 19606-19611.). Briefly, the chromatography paper was soaked in the photoresist for 5 min. After soft baking at 130 °C for 10 min on a hot plate and cooling to room temperature, the paper was exposed to 365 nm UV light (350 W lamp) for 30 s under a transparency mask. Next, the paper was post baked at 130 °C for 10 min on a hotplate. Finally, the paper was immersed in acetone for 1 min to remove the unexposed photoresist. All channels patterned on the paper were 900 μ m wide, and the reservoirs were 2.5 mm in diameter. Individual layers of the paper device were 2 cm x 2 cm.

Paper folding was carried out using the sequence illustrated in Figure 3.1. After folding, the four corners

of the folded paper were removed using scissors so the paper device could be accommodated by the aluminum clamp shown in Figure 3.2d. Pressure was applied evenly by the screws to ensure that the paper layers contacted each other. Four 1.25 mm-diameter holes were drilled into the top plate of the clamp so that test solutions could be injected into the device.

Fluorescence analysis of the *o*PADs was carried out using a Typhoon Trio fluorescent imager (GE Healthcare, Piscataway, NJ). Each paper layer was scanned at a lateral resolution of 100 μm using a 532 nm, 20 mW solid-state laser as the light source and a 640 nm emission filter. The scan was complete within 1 min.

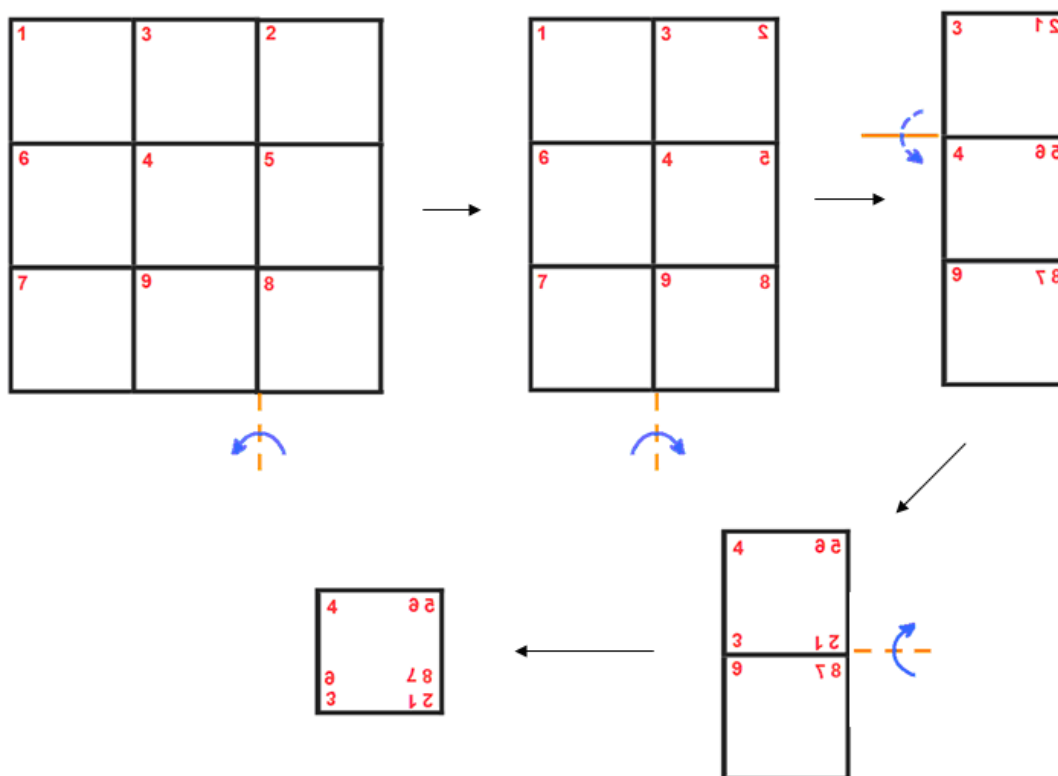


Figure 3.1. The procedure used for folding a piece of paper into a 9-layer oPAD. The numbers in the corners of each square indicate the sequential ordering of the folded device.

3.4 Results and Discussion

Figure 3.2a shows a piece of chromatography paper that has been patterned with channels, reservoirs, and a frame (to provide a template for subsequent folding) fabricated in a single photolithographic step. The fabrication process is based on previously reported procedures¹⁶ and is described in the Experimental Section. As reported previously,¹⁶ the entire photolithographic process can be performed without a cleanroom, using just a hot plate, UV lamp, and a mask produced on a printer. Following photolithography, the 3-D device was assembled by folding the paper along the lithographically defined frame. The frame ensures that the channels and reservoirs are properly aligned after folding into the 3-D assembly. The folding sequence is provided in Figure 3.1. The four corners of the folded paper were trimmed, as shown in Figures 3.2b and 3.2c, to accommodate an aluminum clamp (Figure 3.2d). Solutions could then be injected into the four holes drilled into the top aluminum plate of the clamp (Figure 3.2d).

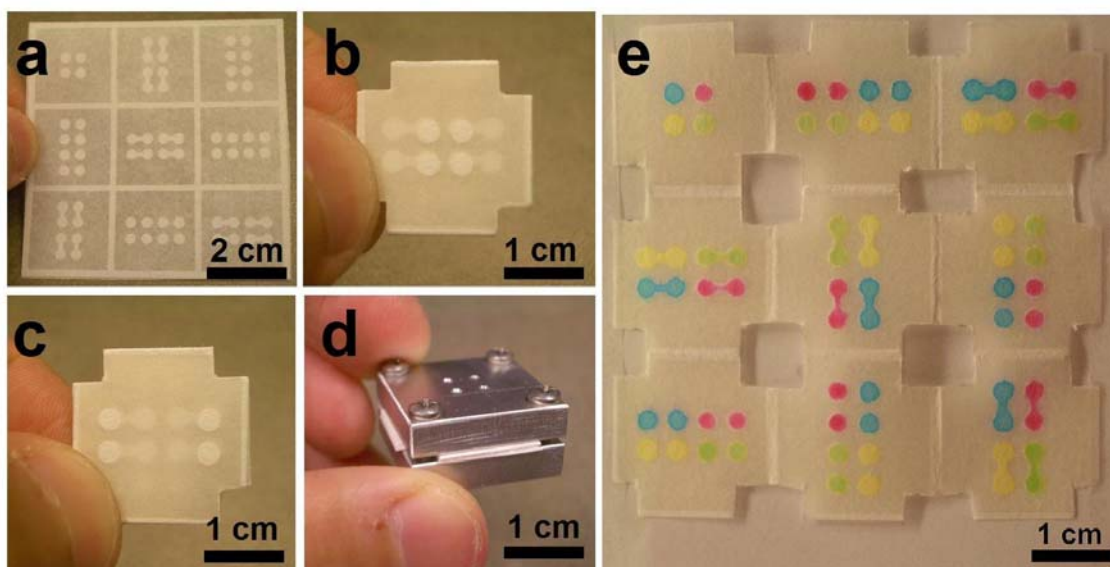


Figure 3.2. (a) A piece of chromatography paper (100 μm thick) having photolithographically patterned channels, reservoirs, and folding frames. All channels were 900 μm wide, and the reservoirs were 2.5 mm in diameter. (b) Top layer of the folded paper revealing four inlet reservoirs in the center of the device. The four flanking circular features are present within the 3-D structure of the device but are visible due to the transparency of the paper. Four corners of the folded paper were cut so it could be clamped in the aluminum housing shown in (d). (c) Bottom layer of the folded paper. (d) The aluminum housing used to support the 3-D paper microfluidic system. The four holes drilled in the top of the housing are used for injecting solutions. (e) An unfolded, 9-layer paper microfluidic device after

injecting four 1.0 mM, aqueous, colored solutions (rhodamine 6G, red; erioglaucine, blue; tatrazine, yellow; and a mixture of erioglaucine and tatrazine, 1:10, green) through the four injection ports in the aluminum clamp. The colored solutions passed through their designated channels and reservoirs without mixing.

Importantly, this origami assembly method does not require adhesive tape, which can lead to contamination and nonspecific adsorption.¹⁶ Avoiding tape also speeds the assembly of the device and eliminates the need for laser cutting. The photoresist pattern serves as the channel wall to separate solutions into different channels in all three dimensions. As described previously,¹⁸ the vertical connections are made by direct contact of paper channels or reservoirs on adjacent layers, and this avoids the use of cellulose powders.¹⁶

The 9-layer device shown in Figure 3.2 was used to demonstrate the ability of the origami device to direct the flow of fluids in three dimensions. Specifically, 10.0 μL of the following four 1.0 mM aqueous solutions were injected through the openings in the top plate of the clamp: rhodamine 6G (red), eriochlorine (blue), tetracycline (yellow), and eriochlorine mixed with tetracycline (1:10, green). After 5 min, the device was unfolded, and, as shown in Figure 3.2e, the solutions flowed through their designated channels and reservoirs without mixing. Moreover, there was no observable nonspecific adsorption of dyes on the channel walls.

As mentioned earlier, every layer of the device can be used for parallel colorimetric analysis of multiple analytes.

This is because the paper can be unfolded after analysis to reveal a permanent record of the assay. This aspect of the method might be useful for multiplexed detection and high-throughput screening. To demonstrate this principle, a two-analyte colorimetric assay of glucose and protein (bovine serum albumin, BSA) was carried out using a single 3-D *o*PAD device comprised of five layers and assembled by origami. The experiment was performed as follows. First, the detection reservoirs (Figures 3.3a and 3.3c) were preloaded with commercially available reagents for the colorimetric detection of glucose and BSA, and then the device, including the reagents, was dried at 20 °C for 30 min. The specific reactions leading to colorimetric detection are provided in Figure 3.4. Second, four 5.0 μ L aliquots containing different amounts of glucose and BSA were injected into the four inlets at the top of the device (Figure 3.3b). The samples flowed toward the detection reservoirs, and a portion of these samples were allowed to react with the preloaded reagents for 10 min. Finally, the paper was unfolded so that both layers having detection reservoirs were accessible for colorimetric analysis. The degree of color change is directly related to the concentration of glucose or protein in the samples.

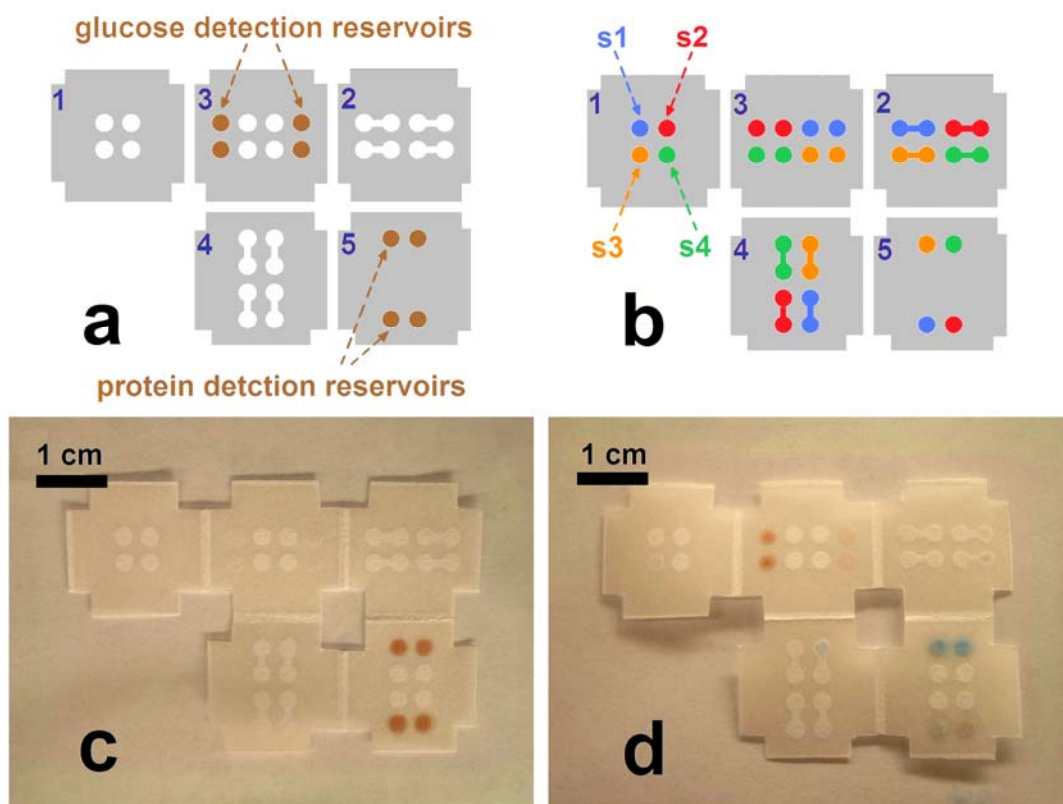


Figure 3.3. (a) A schematic diagram illustrating the design of the network used for assaying glucose and BSA. Note that the detection reservoirs for glucose and BSA are on different levels of the device. (b) A schematic diagram of the same network showing where the four samples were injected. Sample s1 was deionized water used as a control, sample s2 contained 5.6 mM glucose, sample s3 contained 4.5 μ M BSA, and sample s4 contained 5.6 mM glucose plus 4.5 μ M BSA. The numbers at the upper-left corner of the individual layers in (a) and (b) indicate the folding sequence for the

device. (c) Photograph of an unfolded device showing the assay reagents dried in the detection reservoirs. (d) The unfolded 3-D device after completion of the assay. The color change from colorless to brown indicated the presence of glucose in samples s2 and s4. The color change from brown to blue indicated the presence of BSA in samples s3 and s4. No color change was observed for control sample s1.

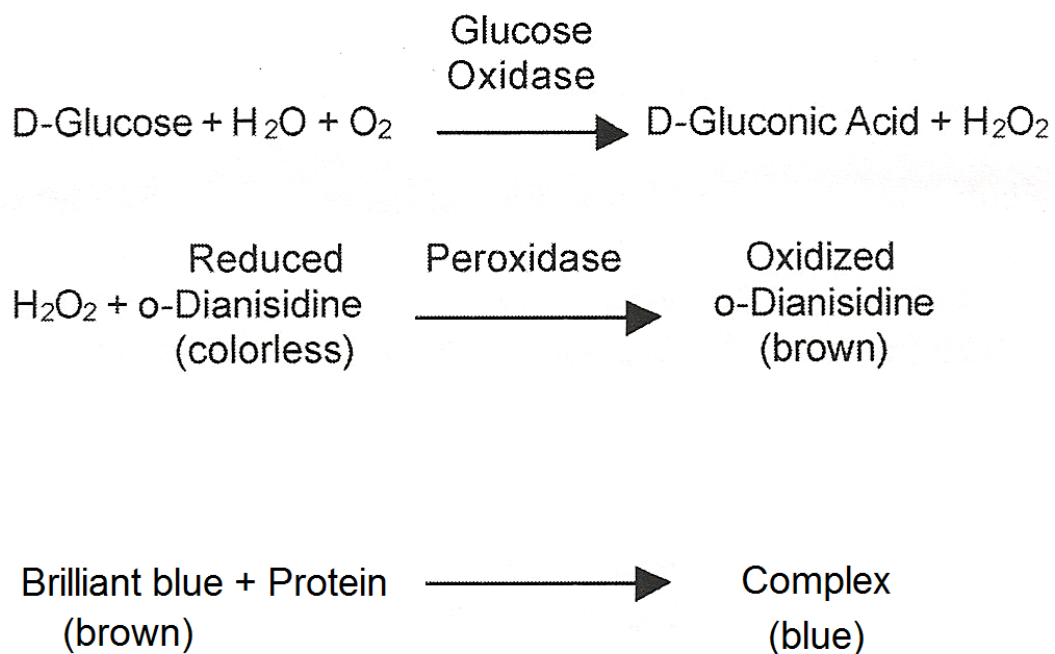


Figure 3.4. The reaction steps for the colorimetric detection of glucose and protein described in the main text.

Comparison of Figures 3.3c and 3.3d indicate that the assay was successful and that there was no mixing between channels or reservoirs. Specifically, the color of the solution in the detection reservoirs exposed to glucose (samples s2 and s4, Figure 3.3b) or BSA (samples s3 and s4) changed from colorless to brown or from brown to blue, respectively. Although only two layers on the device were required for this very simple colorimetric assay, it is obvious that more complex analyses could be performed. To scale up the device for analyzing more analytes or more samples, additional layers might be required. However, all layers of the multilayer network are fabricated simultaneously, so the addition of more layers or more complex structures does not present much of a practical barrier.

Fluorescence detection usually provides substantially higher sensitivity and lower detection limits than simple colorimetric measurements. However, to the best of our knowledge, fluorescence detection has not thus far been used for 3-D μ PAD-based assays. Accordingly, we fabricated 3-layer μ PADs (similar to the device illustrated in Figure 3.3, but with just 3 layers) that could be used to carry out four simultaneous BSA assays using fluorescence detection. The

assay is based on the dye epicocconone, which exhibits enhanced fluorescence in the presence of BSA (Figure 3.5).⁷² The assay for BSA using the paper device was carried out as follows. First, 1.0 μL of a buffered epicocconone solution was spotted onto each detection reservoir and then dried at 20 °C for 5 min. Second, 3.0 μL aliquots of buffered BSA solutions were injected into the four inlets at the top of the device. Third, the *o*PAD was placed in a humidity chamber for 30 min, during which time the BSA solutions passed to the detection reservoirs and reacted with the preloaded fluorescent dye. Finally, the bottom layer of the device was scanned using a fluorescence imager. Each scan was performed at 100 μm resolution and was complete within 1 min.

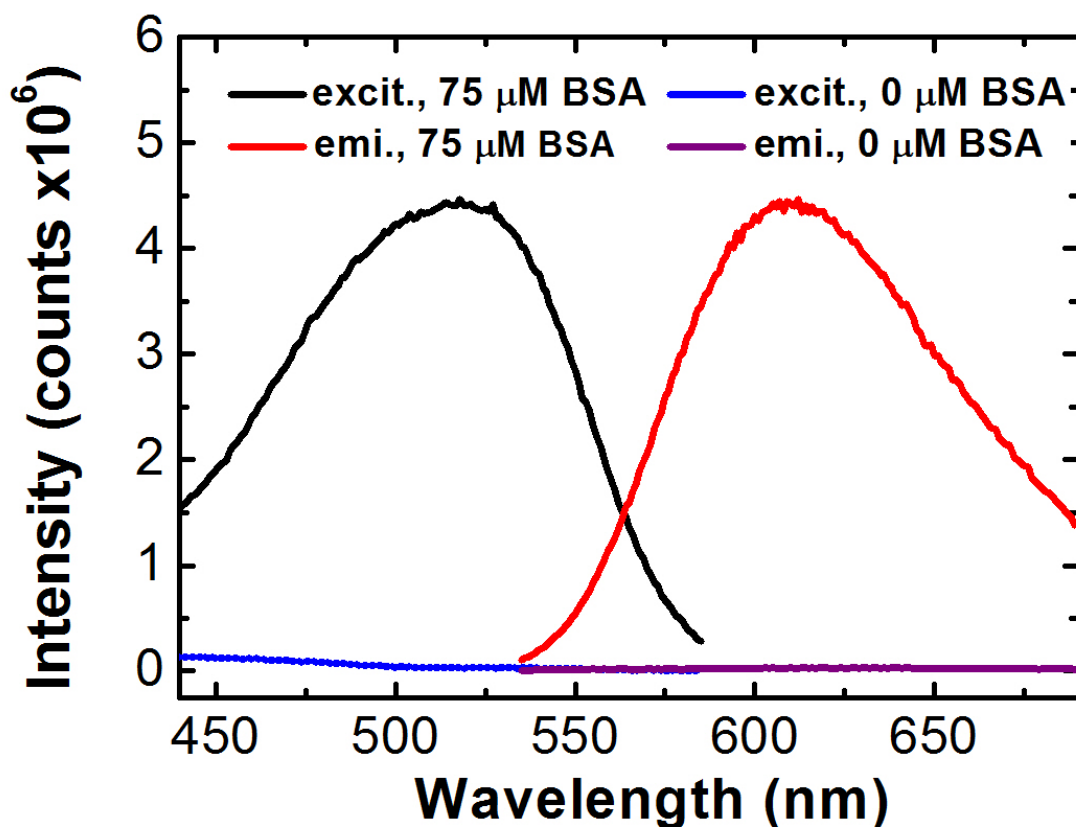


Figure 3.5. Fluorescence excitation and emission spectra of the dye epicocconone in the presence and absence of BSA. The excitation spectrum was normalized so that it has the same maximum intensity as the emission spectrum. The spectra were obtained using a Fluorolog3 fluorometer (HORIBA Jobin Yvon Inc. Edison, NJ). 2.5 mL of the sample solutions, containing 0 or 75 μ M BSA, were mixed with epicocconone and quantification buffer solution and allowed to react for 30 min before the spectra were obtained.

Figure 3.6a shows the result of an assay in which all four BSA aliquots were of the same concentration ($3.0\ \mu\text{M}$), while in Figure 3.6b the concentrations of BSA were different (0 , 0.75 , 1.50 and $3.00\ \mu\text{M}$). Qualitatively, Figure 3.6b shows that the color of the detection reservoirs becomes darker as the concentration of BSA increases. To quantify these results, the images were imported into Adobe Photoshop CS2 and transferred to grayscale mode. The mean fluorescence intensity was determined from the image histogram for each detection reservoir, and then it was background-corrected by subtracting the average intensity measured at the center of the paper where no BSA was present. These data constitute a calibration curve, which is shown in Figure 3.6c. The error bars represent the standard deviation of at least 3 independent measurements. The detection limit, defined as three times the standard deviation of the sample containing no BSA ($0\ \mu\text{M}$) divided by the slope of the calibration curve, is $0.14\ \mu\text{M}$ BSA. Because the fluorescence intensity, rather than the color change, is directly proportional to protein concentration, quantification by fluorescence is more straightforward than colorimetric detection.

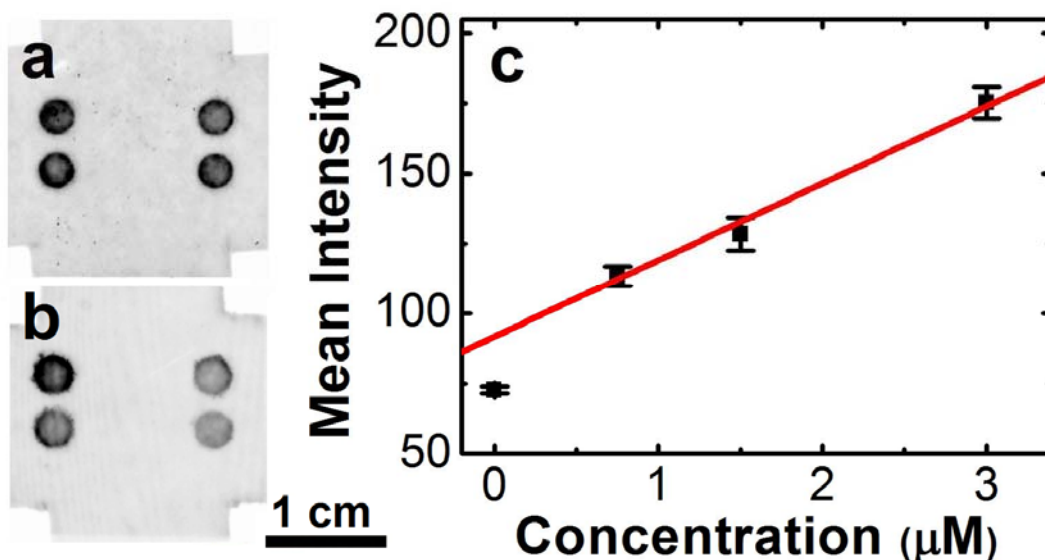


Figure 3.6. (a) and (b) Fluorescence images of the bottom layer of the unfolded oPAD revealing the four detection reservoirs. In (a) all four injected samples contained 3.00 μM BSA, while in (b) the BSA concentrations were 0 (bottom right), 0.75 μM (top right), 1.50 μM (bottom left), and 3.00 μM (top left), respectively. (c) Calibration curve for quantification of BSA. The mean fluorescence intensity was corrected for the background fluorescence of the paper. The error bars represent the standard deviation of at least 3 independent measurements. The data point corresponding to 0 BSA was not included in the fit (red line) as it is outside the linear detection range.

3.5 Summary and Conclusion

To summarize, we have reported an origami-based method for fabricating 3-D paper microfluidic devices. This method provides a number of key advantages compared to previously reported approaches that rely on stacking individual layers and holding them in place with double-sided tape. First, origami fabrication only requires one photolithographic patterning step, regardless of the number of layers. Therefore, the devices can be made arbitrarily complex without much additional fabrication overhead. Second, *o*PADs can be produced by automated printing techniques and subsequently assembled without tools. Third, detection points can be placed on any layer of *o*PADs, because the paper can be easily unfolded to reveal them. Fourth, the resulting permanent record of an assay can be qualitatively analyzed using the naked eye, or the results can be quantified using a high-throughput automated scanner. We believe *o*PADs will prove promising for applications that involve low cost and simplicity.

Chapter 4: A Paper-Based Electrochemical Sensing Platform with Integral Battery and Electrochromic Read-out

4.1 Synopsis

In this chapter we report a battery-powered, microelectrochemical sensing platform that reports its output using an electrochromic display. The platform is fabricated based on paper fluidics, and uses a Prussian blue spot electrodeposited on an indium-doped tin oxide thin film as the electrochromic indicator. The integrated metal/air battery powers both the electrochemical sensor and the electrochromic readout, which are in electrical contact via a paper reservoir. The sample activates the battery and the presence of analyte in the sample initiates the color change of the Prussian blue spot. The entire system is assembled on the lab bench, without the need for cleanroom facilities. The applicability of the device to point-of-care sensing is demonstrated by qualitative detection of 0.1 mM glucose and H_2O_2 in artificial urine samples.

4.2 Introduction

In this chapter, we report a versatile microelectrochemical biosensing platform that is based on

paper fluidics and powered by an integral metal/air battery. The battery powers both the sensing chemistry and an electrochromic display that provides an optical indication of the state of the system. The operating voltage of the device is controlled by the identity of the metal foil used in the battery. The sensor is activated by application of artificial urine (AU), which acts both as the matrix for the analyte and the electrolyte for the battery. The entire system is assembled on the lab bench without the need for cleanroom facilities. Taken together, these characteristics suggest the approach described here is appropriate for point-of-care (POC) diagnosis and resource-limited sensing.⁵

Electrochemical methods are widely used for chemical sensing due to their low cost, low power requirements, and simplicity.⁷³ Most such devices are based on electrolytic reactions and hence require a reader powered by either a battery or line voltage. However, a few self-powered sensors have also been reported.⁷⁴⁻⁷⁶ The operational basis of the latter devices is a galvanic reaction that is initiated by the presence of an analyte which may or may not itself be redox active. For example, we recently reported a self-powered sensor in which a galvanic reaction is triggered by the presence of non-electroactive trypsin.⁷⁶

Recently, microfluidic paper analytical devices (μ PADs) have emerged as a promising solution to the need for low-cost diagnostic systems.¹⁷ The success of μ PADs arises from two main factors: low cost and visual (colorimetric) readout. However, there is a problem with colorimetric detection: a unique chemistry must be devised and optimized for every reaction. Electrochemical systems provide some relief for this situation, because current replaces the visual readout signal. This fact has driven the development of microfluidic paper electrochemical devices (μ PEDs), which now have the capability of detecting multiple analytes via amperometry.^{21,22} However, the design principle for μ PEDs that have been reported thus far involves a disposable paper fluidic system that is controlled and read out using a conventional potentiostat^{21,68} or commercial reader.^{22,77} Note, however, that in parallel with the development of μ PEDs, research in the field of energy storage has resulted in paper-based batteries.^{78,79}

The principal advance reported in the present article is a broadly applicable means for fully integrating μ PEDs with an inexpensive, on-board power source without giving up the convenience of visual color-based read-out that has driven the field of μ PADs. The operational principles of the device are illustrated in Figure 4.1. The sensor is powered

by a metal/air battery that drives electrolytic reactions in a paper reservoir defined by a wax frame. Electrical contact is made to the paper via a pair of transparent indium-doped tin oxide (ITO) electrodes. The paper is preloaded with a dried enzyme and $\text{Fe}(\text{CN})_6^{3-}$ or $\text{Fe}(\text{CN})_6^{4-}$. The analysis of glucose in AU is carried out as follows. First, glucose in AU is applied to the paper fluidic system, which directs the sample to the reaction zone. Second, glucose oxidase (GOx) present in the paper reaction zone catalyzes glucose oxidation with simultaneous reduction of $\text{Fe}(\text{CN})_6^{3-}$ to $\text{Fe}(\text{CN})_6^{4-}$. This process activates conversion of electrochromic Prussian blue (PB) on the ITO electrode to colorless Prussian white (PW). As discussed later, a similar approach is used to detect peroxide.

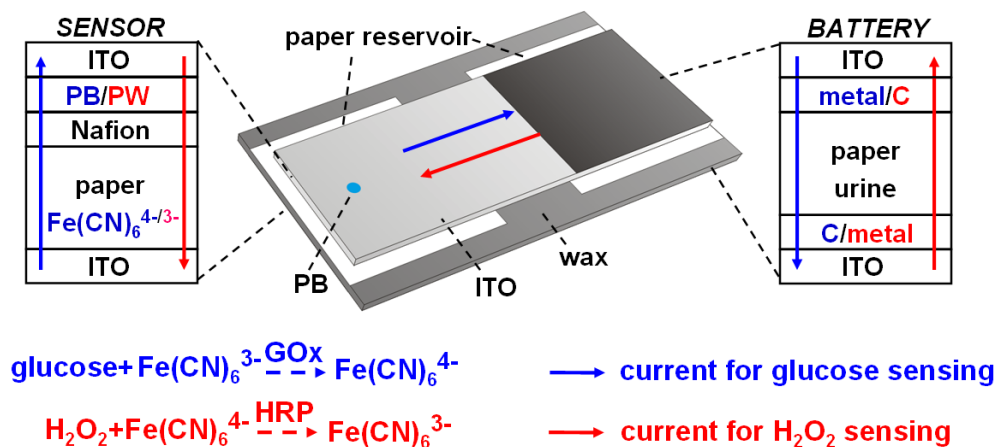


Figure 4.1. A drawing illustrating the operational principles of the device. The device consists of two parts: a sensor section and an Al/air battery section, which are separated by a wax barrier. For glucose detection, the paper reservoir of the sensor section is preloaded with dried GOx and Fe(CN)_6^{3-} . The catalytic oxidation of glucose by GOx results in conversion of Fe(CN)_6^{3-} to Fe(CN)_6^{4-} . Fe(CN)_6^{4-} is then oxidized back to Fe(CN)_6^{3-} on the lower ITO electrode, which results in reduction of PB to colorless PW on the upper ITO electrode. The H_2O_2 sensor operation is similar, except that HRP catalyzes the oxidation of Fe(CN)_6^{4-} to Fe(CN)_6^{3-} in the presence of H_2O_2 . The resulting Fe(CN)_6^{3-} is then reduced at the lower ITO electrode, while PW is oxidized to PB at the upper ITO electrode. The battery section of the device drives the electrochemical reactions in the sensor section.

4.3 Experimental

Chemicals and materials. ITO electrodes were obtained from Delta Technologies (Loveland, CO), and cut into 25 mm x 10 mm pieces using a glass cutter. Conductive carbon ink, thinning solution (Creative Materials, Inc. Tyngsboro, MA), and activated carbon (Sigma-Aldrich) were used to fabricate the battery cathode. Zn, Co, Pb (Alfa Aesar), Cu (Sigma Aldrich), and Al (Reynolds Wrap, Fisher Scientific) foils were used to fabricate the battery anode. A Sharpie wax pencil (Fisher Scientific) was used for patterning the sensing area on chromatographic paper (Grade 1, Whatman). Glucose oxidase was obtained from MP Biomedicals (Solon, OH) and horseradish peroxidase was purchased from Sigma Aldrich. D-glucose and 30% H_2O_2 solution were obtained from Fisher Scientific. $\text{FeCl}_3 \cdot 6\text{H}_2\text{O}$, $\text{K}_3\text{Fe}(\text{CN})_6$, and $\text{K}_4\text{Fe}(\text{CN})_6$ were obtained from Acros Organics. All chemicals necessary for preparing the AU were from Sigma-Aldrich. A Nafion membrane (N-115, Fuel Cell Store, Inc., Boulder, CO) was used to separate the anodic and cathodic reactions in the sensing reservoir while maintaining ionic conductivity. All solutions were prepared with deionized water (18.0 $\text{M}\Omega \cdot \text{cm}$, Milli-Q Gradient System, Millipore). All reagents were used as received.

Artificial urine. AU was prepared according to a previously published procedure.¹⁶ It contained 1.1 mM lactic acid, 2.0 mM citric acid, 25 mM sodium bicarbonate, 170 mM urea, 2.5 mM calcium chloride, 90 mM sodium chloride, 2.0 mM magnesium sulfate, 10 mM sodium sulfate, 7.0 mM potassium dihydrogen phosphate, 7.0 mM dipotassium hydrogen phosphate, and 25 mM ammonium chloride. The pH was adjusted to 6.0 using 1.0 M HCl.

Prussian blue. Electrodeposition of PB on an ITO electrode was carried out as follows. First, a 1-mm thick poly(dimethylsiloxane) (PDMS) slab was prepared by pouring premixed PDMS precursor (Sylgard 184, Dow Corning, Midland, MI) into a plastic petri dish (Fisher Scientific) and curing at 80 °C in a convection oven for 2 h. Second, a 1.2 mm-diameter hole was punched into the slab using a 16-gauge syringe needle to yield a mask. Third, electrodeposition of PB through the mask and onto the ITO was carried out using a previously reported procedure.⁸⁰ Briefly, a plating solution containing 2.6 mM HCl, 10 mM $\text{K}_3\text{Fe}(\text{CN})_6$, and 10 mM FeCl_3 was freshly prepared, and then a 100 μL aliquot was dropcast into the hole in the mask. Electrodeposition was carried out for 60 s at a constant cathodic current of 0.4 $\mu\text{A}/\text{mm}^2$ using a Ag/AgCl reference electrode, a Pt counter electrode, and a CHI 760B potentiostat (CH Instruments, Austin, TX).

After deposition, the mask was removed, the ITO electrode was, washed with deionized water, and then it was dried under nitrogen gas.

Battery. The battery cathode was fabricated using a mixed carbon material containing 1 g of activated carbon, 4 g of conductive carbon ink, and 2 g of thinning solution. The carbon material was coated onto half of an ITO electrode using a Meyer rod (R.D. Specialties, Inc. Webster, NY). The carbon electrode was then cured at 80 °C in a convection oven for 30 min. The battery anode was fabricated by attaching a piece of metal foil (5 mm x 5 mm) onto an ITO electrode. The open-circuit voltage (OCV) and short-circuit current (SCC) of the batteries were measured using a CHI 760B potentiostat in a two-electrode mode. The SCC was measured with one electrode held at 0 V relative to the other.

Sensors. The paper reservoirs (10 mm x 10 mm) for the sensing and battery modules were fabricated using a wax pencil and a ruler. The hydrophobic walls of the reservoirs were fabricated by drawing on the chromatographic paper using the wax pencil guided by the ruler. The paper was then placed on a hot plate (80 °C for 10 min) to melt the wax so that it penetrated into the paper layer. The paper was then cooled to 20 °C. For glucose sensing, 40 µL of a solution

containing 125 mM $\text{K}_3\text{Fe}(\text{CN})_6$ and 500 U glucose oxidase in 0.01 M PBS buffer (pH 7.4) was dropcast onto the paper electrochemical cell and then dried at 20 °C. For H_2O_2 sensing, 40 μL of a solution containing 125 mM $\text{K}_4\text{Fe}(\text{CN})_6$ and 100 U horseradish peroxidase in 0.01 M PBS buffer (pH 7.4) was dropcast onto the paper electrochemical cell and then dried at 20 °C.

The sensors for glucose and H_2O_2 were fabricated by sandwiching the paper, which defined the sensing and battery reservoirs, between two ITO electrodes. A Nafion membrane was used to separate the sensing reagents from the ITO electrode on which the PB or PW spot was immobilized. A binder clip was used to clamp the ITO electrodes so that all layers were in contact with one-another. Electrochemical sensing was initiated after injecting the sample (contained in AU) into the sensing reservoir. Upon injection of battery electrolyte, the battery was then activated to report the sensing result.

4.4 Results and Discussion

Device overview. Figure 4.2a shows cyclic voltammograms (CVs) of ITO electrodes in 0.01 M PBS buffer (pH 7.4) and AU. In both cases no significant current is observed between 1.2 V and -0.6 V (vs. Ag/AgCl). However,

when a thin film of PB is electrodeposited on the ITO electrode,⁸⁰ a pair of redox peaks is observed at 0.207 V and 0.158 V. These are due to the reversible interconversion of PB (blue) to PW (clear, at more negative potentials).⁸⁰

When one ITO electrode modified with PB or PW is used to construct a two-electrode cell with a second, naked ITO electrode, the reduction of PB to PW can be used to visually report an oxidation reaction occurring on the naked ITO electrode. Likewise, the oxidation of PW to PB can be used to visually report a cathodic reaction on the naked ITO electrode. This is an important property of the device shown in Figure 4.1, and it is implemented here by separating the anode and cathode with a thin film of Nafion.

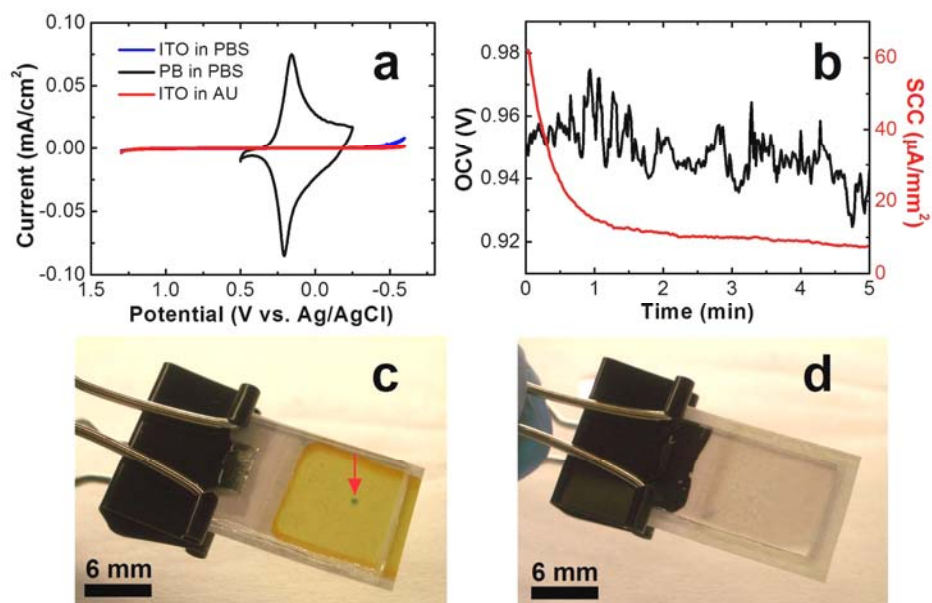


Figure 4.2. (a) CVs for a naked and a PB-coated ITO electrode in 0.01 PBS buffer (pH 7.4) and a CV for a naked ITO electrode in AU. (b) OCV and SCC measurements for the Al/air battery after activation by AU. (c) A photograph of the battery-powered electrochemical sensor used for glucose detection. A PB dot (diameter = 1.19 mm, indicated by the red arrow) is visible in the sensor region (10 mm by 10 mm, Figure 4.1) and surrounded by a wax barrier. The yellow color arises from preloaded $\text{Fe}(\text{CN})_6^{3-}$. (d) A photograph of the battery-powered electrochemical sensor used for H_2O_2 . The PW dot is colorless so that it is not visible at the sensing area. The binder clip was used to clamp the ITO electrodes together.

As shown in Figure 4.2c, the PB reporter dot used in this work was 1.19 mm in diameter, and it was electrodeposited on the ITO electrode through a hole punched on a PDMS thin film at a current density of 0.4 $\mu\text{A}/\text{mm}^2$ for 60 s (24 $\mu\text{C}/\text{mm}^2$). Unlike some colorimetric reagents, PB is stable indefinitely under ambient conditions. The total charge used to deposit the PB spot for each device reported here was uniform to ensure reproducible color changes. Importantly, the amount of charge stored in the PB or PW spot can be adjusted to match the detection limit and range of the sensor for specific clinical needs. Under optimal conditions, the relationship between the diameter of the PB or PW spot (d in mm) and the lowest detectable concentration (C in M) of analyte having a particular volume (V in L) is given by eq 1.

$$C = \frac{a\pi d^2 Q}{4nFV} \quad (1)$$

Here, Q is the charge density required for color transition of PB or PW in C/mm^2 , n is the number of electrons transferred for the sensing reaction, F is the Faraday constant, and a is a dimensionless empirical constant, which is larger than unity and related to experimental conditions such as sensing time, mass transfer,

and enzyme activity. For the devices reported here, C is given by eq 2.

$$C = 4.88 \times 10^{-6} ad^2 = 6.96 \times 10^{-6} a \quad (2)$$

The metal/air battery used in this work was easily fabricated using a piece of metal foil as the anode, high-surface area activated carbon as the cathode for oxygen reduction, and paper as the separator. The same ITO electrodes used for sensing were used as the current collectors for the battery. The battery was activated immediately prior to sensing by injecting 40 μ L of AU onto the paper reservoir. This eliminates the possibility of discharge during long-term storage, and the use of AU as both the battery electrolyte and sample matrix streamlines use of the sensor. Note that activation of a paper-based battery with AU has been reported previously.^{81,82} The voltage provided by the battery depends on the identity of the metal-foil anode. As shown in Figure 4.3, the open circuit voltages (OCV) for batteries, using Zn, Co, Pb, and Cu foils as the anodic materials, were 1.1, 0.68, 0.56 and 0.25 V, respectively, and the short-circuit currents (SCC) increased with increasing battery voltages (Figure 4.4). In the present study, a 5 mm x 5 mm piece of Reynolds Wrap Al foil was used as the anode for all sensors. The per-sensor cost of the foil is \$US 0.00006, and the total cost for each

battery, including the ITO current collectors, is \$US 0.95. As shown in Figure 4.2b, the average OCV of the Al/air battery was about 0.94 V with a maximum peak-to-peak variation of 50 mV over a period of 5 min. The SCC onset current was 60 $\mu\text{A}/\text{mm}^2$ and decreased to 8 $\mu\text{A}/\text{mm}^2$ after 5 min. For applications other than those described here, it might be advantageous to use different metals in the battery to lower its voltage and thereby avoid background redox processes.

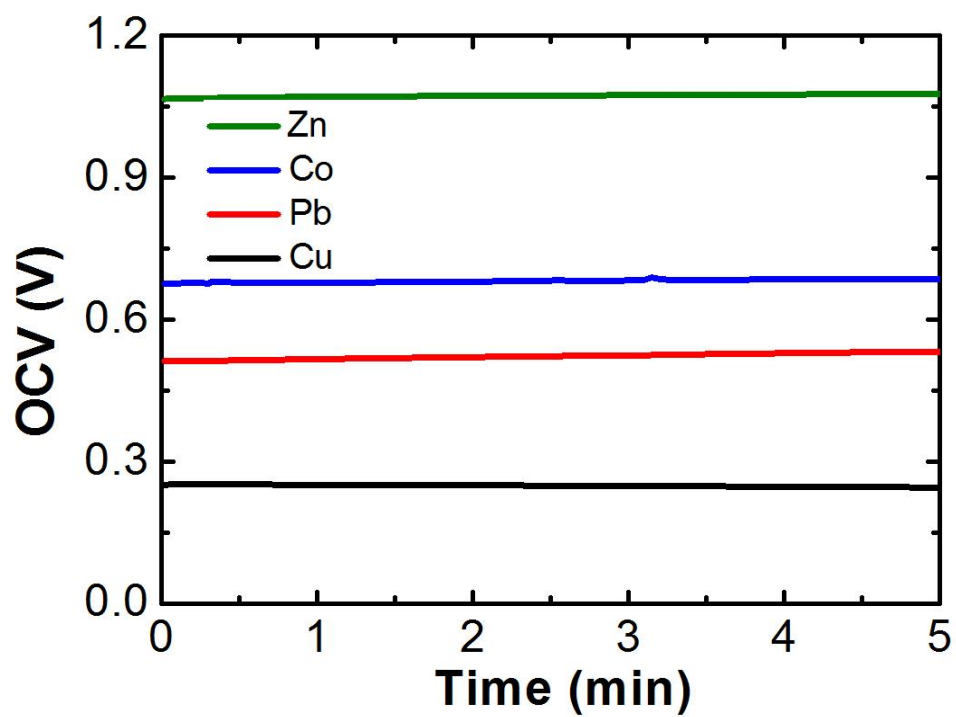


Figure 4.3. Open-circuit voltages (OCVs) as a function of time for batteries employing different metal foils (anodes) and 5 M NaCl as electrolyte.

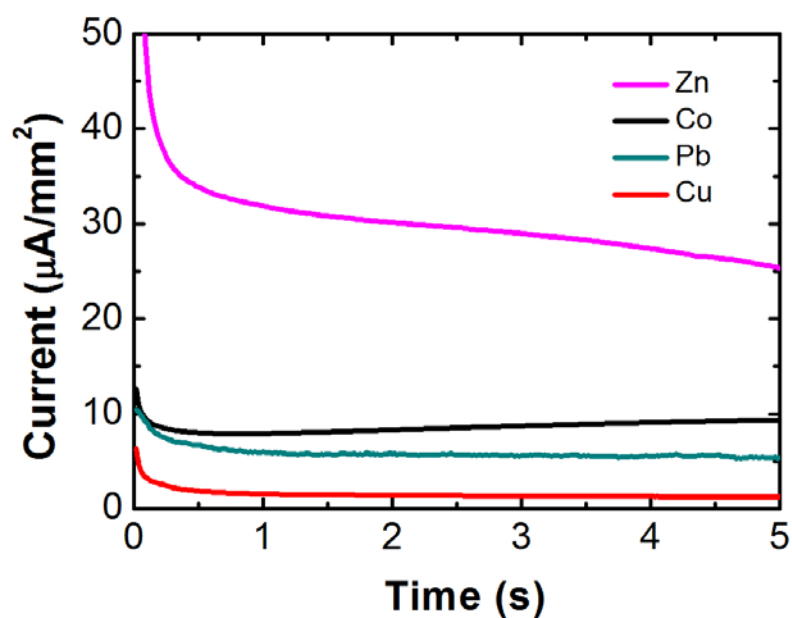


Figure 4.4. Short-circuit currents (SCC) as a function of time for batteries employing different metal foils (anodes) and 5 M NaCl as electrolyte.

The sensors shown in Figures 4.2c and 4.2d were configured for detection of glucose and H_2O_2 , respectively. The two ITO electrodes were clamped together using a binder clip to ensure reproducible contact between the different layers in the sensor. The top row of micrographs in Figure 4.5 show the electrochromic reporting areas of a glucose sensor before and after injecting 40 μL of an AU sample containing 0.10 mM glucose. The results from a glucose-free injection are also shown. After injecting the 0.10 mM glucose sample, the PB spot turned from blue to colorless, as shown in Figure 4.5b. However, under otherwise identical conditions the glucose-free control sample had no effect on the color of the PB spot (Figures 4.5c and 4.5d). Prior to use of the device for H_2O_2 sensing, the PB spot was reduced to PW (colorless) by holding the potential of the ITO electrode at -0.8 V vs. the other ITO electrode for 60 s in 0.01 M PBS buffer (pH 7.4). A slight coloring of the PW spot is present in Figure 4.5e, and this is due to air oxidation during the device fabrication process. Next, 40 μL AU samples containing 0.10 mM H_2O_2 , or a H_2O_2 -free solution, were injected onto the paper defining the sensing areas. The color of PW spot turned from nearly colorless to blue for the sample containing 0.10 mM H_2O_2 (Figure 4.4f), but no

color change was observed for the control sample (Figures 4.5g and 4.5h). The lowest detectable concentration of H_2O_2 and glucose was 0.10 mM, and therefore, according to eq 2, the empirical constant a is 14.4 for these sensors.

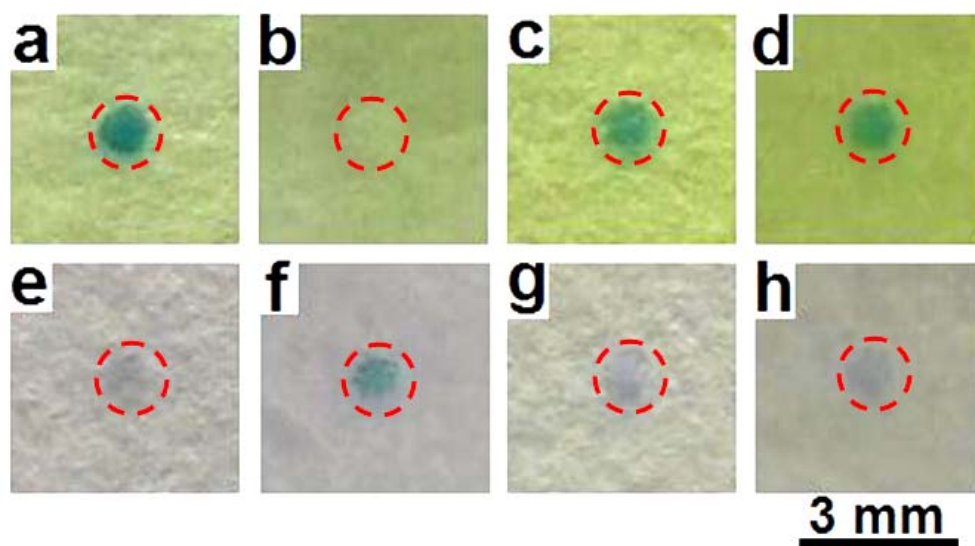


Figure 4.4 (Top row) Photographs of PB spots (highlighted in red circles) on a glucose sensor (a) before and (b) 50 s after injection of 40 μL of AU containing 0.10 mM glucose. The PB spot turned from blue to colorless due to the presence of glucose. Photographs of a PB spot on a glucose sensor (c) before and (d) 50 s after the injection of 40 μL of glucose-free AU. No color change is observed in the absence of glucose. (Bottom row) Photographs of a PW spot on a H_2O_2 sensor (e) before and (f) 50 s after injection of a 40 μL AU sample containing 0.10 mM H_2O_2 . The PW spot turned from nearly colorless to blue due to the presence of H_2O_2 . Photographs of a PW spot on a H_2O_2 sensor (g) before and (h) 50 s after the injection of 40 μL of H_2O_2 -free AU. No color change is observed in the absence of H_2O_2 .

4.5 Summary and Conclusion

We have reported the first paper-based microelectrochemical sensing platform that incorporates an integral power source. The on-board metal/air battery powers both the sensing reactions and the color conversion of the electrochromic spot used for read-out. The voltage provided by the battery is easily controlled by changing the identity of the metal foil, which means that different redox processes can be used for both the sensing chemistry and the electrochromic read-out. The detection limit and dynamic range of the sensor is controlled by matching the amount of charge stored in the PB/PW spot to the clinical threshold values required for different biomarkers. The fabrication of the sensor is very simple and does not require cleanroom facilities. The cost of the sensor, including the integral battery, is very low.

Here we have focused on using the device for obtaining qualitative results. However, studies presently underway are focused on quantitative detection of more realistic biomarkers over a broader range of analyte concentrations. It will also be possible to replace the ITO current collectors in the next generation of this platform, so that the entire device is constructed of paper. These

enhancements will improve the likelihood that this type of sensing platform will be useful for point-of-care clinical diagnosis and electrochemical sensing under resource-limited conditions.

Chapter 5: Aptamer-based Origami Paper Analytical Device for Electrochemical Detection of Adenosine

5.1 Synopsis

Here we report a self-powered origami paper analytical device (oPAD) that uses an aptamer to recognize an analyte, a glucose oxidase (GOx) tag to modify the relative concentrations of an electroactive redox couple, and a digital multimeter (DMM) to transduce the result of the assay. The sensor is self-powered in that it self-generates an electrical signal so that the read-out process is similar to testing a battery. The principle of the sensor is illustrated in Scheme 5.1. Briefly, the device is printed on a single piece of paper, folded into a three-dimensional (3D) configuration, and then laminated in plastic. An aliquot of sample is loaded at the inlet, split into two channels, and then directed to microbeads entrapped within the channels. In one channel, an aptamer immobilized on microbeads binds to the target and releases a GOx-labeled DNA strand that flows downstream. No aptamer is present on the microbeads in the other channel, which is used as a control. The split fluids terminate in an hour-glass-shaped, two-compartment electrochemical cell. The waist of the hour glass serves as a salt bridge between the two half cells. In one of the half

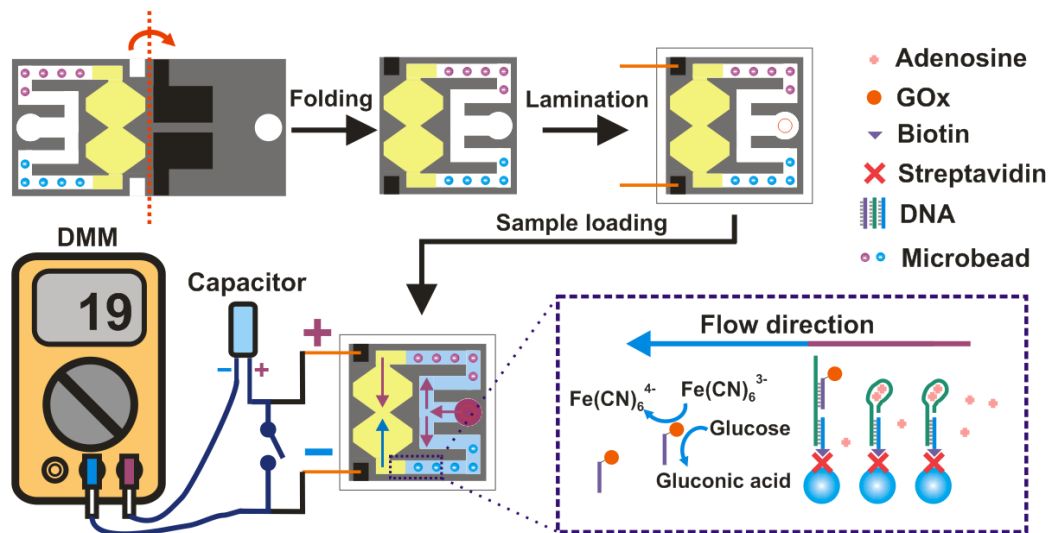
cells, GOx catalyzes the oxidation of glucose, which in turn results in conversion of $\text{Fe}(\text{CN})_6^{3-}$ to $\text{Fe}(\text{CN})_6^{4-}$. The difference in concentrations of $\text{Fe}(\text{CN})_6^{3-}$ and $\text{Fe}(\text{CN})_6^{4-}$ in the sensing half cell and control half cell results in a voltage that is used to charge a capacitor. When the switch (lower part of Scheme 5.1) is closed, the capacitor discharges through the DMM. The capacitor provides a high instantaneous current, in effect an amplified current, and hence a higher sensitivity than a direct current measurement.

5.2 Introduction

In this chapter, we report a self-powered origami paper analytical device (oPAD) that uses an aptamer to recognize an analyte, a glucose oxidase (GOx) tag to modify the relative concentrations of an electroactive redox couple, and a digital multimeter (DMM) to transduce the result of the assay. This device and its operational features are important for five reasons. First, the aptamer is immobilized on microbeads trapped within the paper fluidic channel. This design greatly simplifies probe introduction, compared to direct immobilization on paper,⁸³ because existing bead immobilization and characterization methods can be used for a range of different probe families including aptamers, DNazymes,⁸⁴⁻⁸⁸ and antibodies. Second, as

configured in this device, bead immobilization eliminates the need for a washing step. Third, although aptamers and other nucleic acid probes have been used on test strips,^{89,90} they have not been integrated with fluidic devices using patterned paper. Aptamers can bind to a wide range of targets, including those (like the adenosine target we report) that are not immunogenic.⁸⁴⁻⁸⁶ Moreover, nucleic acid probes are generally more stable than those based on proteins.⁵ Fourth, the transducer is based on a concentration cell, which acts like a battery to charge a capacitor that is subsequently read-out using a DMM. The latter has a very wide dynamic range, and the use of the capacitor results in a quantitative response that yields a 17-fold enhancement of sensitivity compared to a direct current measurement. Finally, the device is encapsulated in plastic using impulse edge thermal lamination, which solves many problems, including fluid evaporation, reagent deactivation, and device contamination.

Scheme 5.1



Paper fluidics have their genesis in the lateral flow test strip, which was first released commercially by Unipath in 1988 in the form of a home pregnancy test kit.⁹¹ The low cost and ease of use of this family of devices ensured an expansion in the number of types of assays available, particularly for point-of-care applications.⁵ In 2007, Whitesides and coworkers added functionality to the basic lateral flow design by developing a means for dividing the paper substrate into hydrophilic and hydrophobic regions.⁴ These types of devices are now known as microfluidic paper analytical devices (μ PADs).^{17,18,21,92-97} In 2008, Whitesides and co-workers introduced 3D PADs, which were constructed by alternating layers of patterned paper and double-sided tape.¹⁶ These devices introduced even more functionality, but the fabrication method does not lend itself to mass production. More recently, we reported an origami-based method that resolves the fabrication problems associated with multi-level μ PADs.⁹⁸ Origami PADs (*o*PADs) are fabricated (patterned) on a single sheet of chromatography paper and then folded into a 3D fluidic architecture using simple principles of origami (no adhesive tape or scissors are permitted).

Most paper-based assays transduce the sensing/recognition chemistry using colorimetry,^{95,98} fluorescence,⁹⁸ or electrochromism.⁹⁹ Therefore image recording using a camera or scanner, a computer, and appropriate software are required for quantification and unambiguous analyte determination.^{95,98} These add time, cost, complexity, and uncertainty (i.e. variation of light) to the assay. Electrochemical methods have also been used to transduce signals from paper-based devices.^{21,68} Such experiments normally involve a potentiostat, which limit applications for POC testing. Handheld readers have alleviated this drawback, and in particular, μ PADs have been integrated with personal glucose meters (PGM).²² However, the sensing chemistry in that case is based on direct oxidation of analytes using the relevant oxidases or dehydrogenases, and the applicability of such sensors to a specific analyte is limited by the availability of the redox enzyme. Note also that the PGM is designed to detect glucose in the millimolar concentration range, and thus requires significant signal amplification for trace analysis.⁷⁷

5.3 Experimental

Chemicals and materials All DNA was ordered from Integrated DNA Technologies, Inc. Streptavidin-labeled

glucose oxidase (sGOx) was purchased from Rockland Immunochemicals, Inc. (Gilbertsville, PA). Streptavidin-coated polystyrene microbeads and fluorescent polystyrene microbeads with Nile red inside were purchased from Spherotech, Inc. (Lake Forest, IL). Adenosine and Glucose oxidase (GOx) from *Aspergillus niger* were obtained from Sigma Aldrich. D-glucose and $K_3Fe(CN)_6$ was purchased from Fisher Scientific. All solutions were prepared with deionized water (18.0 M Ω cm, Milli-Q Gradient System, Millipore). Conductive carbon ink (Creative Materials, Inc. Tyngsboro, MA) was used to fabricate electrodes using a coating kit (RD Specialties, Inc. Webster, NY). All paper fluidic devices were fabricated using Grade 1 Whatman chromatographic paper. Scotch thermal laminating pouches (TP5851-20) and a Jorestech impulse thermal edge sealer were used for thermal lamination of the device. A 2.2 μ F electrolytic capacitor, a switch, and a breadboard with jumper wires were obtained from RadioShack. All reagents and materials were used as received.

Experimental procedures The patterning of paper is based on a slight modification of a wax printing procedure reported previously.¹¹ Briefly, a Xerox 8570DN inkjet printer was used to print wax-based solid ink on Whatman chromatography paper. The paper was then placed on a hot

plate with the wax side up for 15 s at 120 °C, and then cooled to 20 °C. For fabricating electrodes, the patterned paper was placed on a flat glass surface, and then covered with a home-made stencil. An aliquot of carbon ink was dropcast on the stencil. A coating rod was used to coat the carbon ink uniformly onto the patterned paper through the stencil. To cure the carbon ink, the stencil was removed from the paper, and the paper was placed in an oven at 80 °C for 30 min.

For preparing GOx-labeled DNA, 12.5 μM biotin-modified DNA (bDNA) solution was mixed with a 100 μM streptavidin-labeled GOx (sGOx) solution to yield a solution containing 1:1 bDNA and sGOx. The sGOx solution also contains 10 mg/mL bovine serum albumin (BSA) as a stabilizer and 0.1 mg/mL sodium azide as a preservative. After reaction for 24 h, an Amicon 50 K centrifugal filter (Millipore) was used to separate the GOx-labeled bDNA from free bDNA by centrifugal filtering. All solutions were diluted to the same volume for UV-vis characterization, which leads to a concentration of 0.46 μM for both bDNA and sGOx solutions. The UV-vis spectra were taken using a UV-vis spectrometer (Hewlett-Packard 8453).

As shown in Figure 5.1, the characteristic maximum absorptions of protein and DNA are at 280 nm and 260 nm

respectively. Note that the absorption of sGOx at 280 nm is significantly higher than that of bDNA at 260 nm at the same concentration due to the difference in extinction coefficients and excess BSA in the sGOx solution. For a solution containing both sGOx and bDNA at a 1:1 molar ratio, the absorption at 260 nm was higher than that of the solution containing only sGOx due to the presence of bDNA in the solution. After filtration using a 50 k cut-off centrifugal filter, all the sGOx-labeled bDNA was maintained in the retentate, but the free bDNA passed the filter into the filtrate. The absorption of the retentate at 260 nm was obviously higher than that of the solution containing only sGOx, which demonstrates the formation of the bDNA-sGOx conjugate that was left in the retentate. The absorption of the retentate overlapped with the absorption of the 1:1 sGOx and bDNA mixture, which demonstrates that the ratio of sGOx to bDNA in the final product was approximately 1:1. This agrees with the fact that the absorption of the filtrate at 260 nm was very small. Therefore, almost all bDNA binds to sGOx with minimal free bDNA in the filtrate.

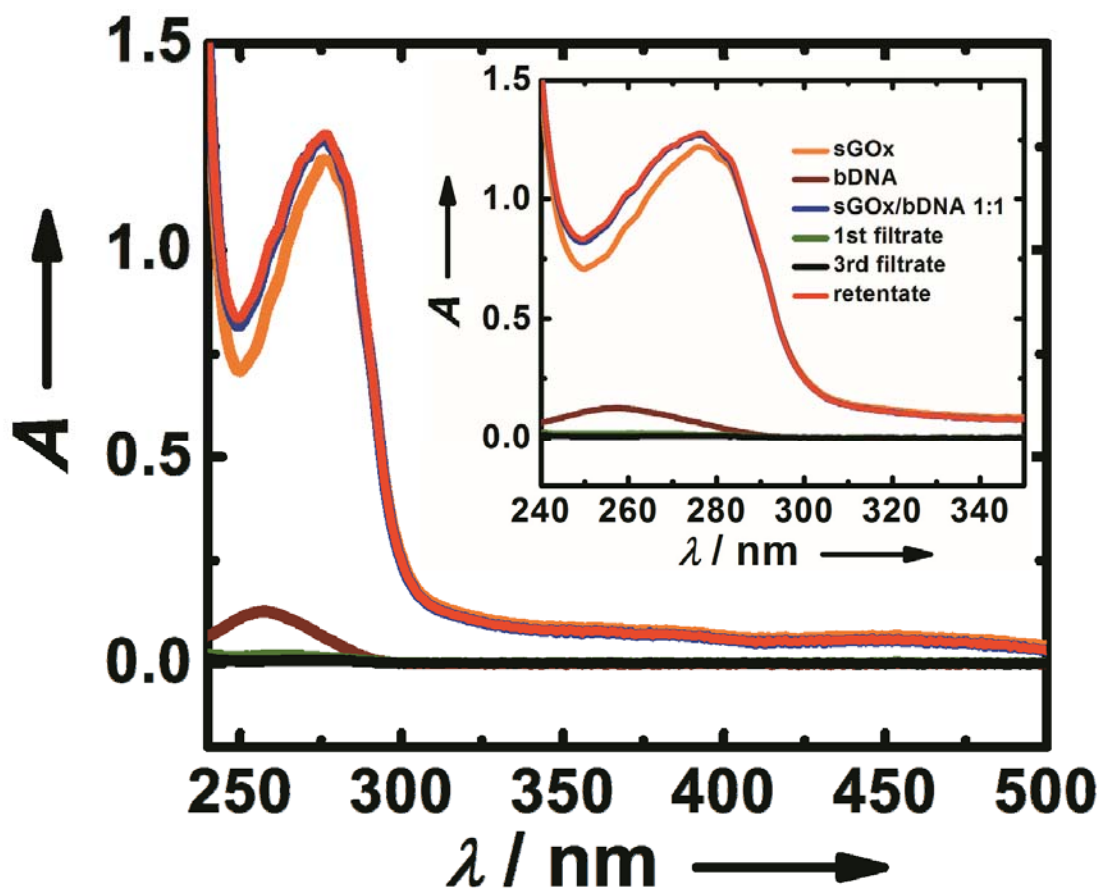


Figure 5.1. UV-vis spectra of 0.46 μM sGOx solution, 0.46 μM bDNA solution, a mixture of 0.46 μM sGOx and 0.46 μM bDNA, filtrate and retentate of the mixture after reacting for 24 hours obtained by filtering using a 50 K cut-off centrifugal filter. All solutions were diluted to the same volume for comparing the UV-vis spectra. Inset: the UV-vis spectra from 240 nm to 350 nm.

To prepare the device for electrochemical sensing, 12 μL of 100 mM glucose and 100 mM $\text{Fe}(\text{CN})_6^{3-}$ in 0.01 M PBS buffer (pH 6.0) was loaded into both halves of the electrochemical cell, and dried in air. A 20 μL solution containing 25 μM biotin-DNA strand was mixed with 20 μL 0.5% (w/v) streptavidin-labeled microbeads. After reaction in the dark for 24 h, the resulting solution was mixed with a 40 μL solution containing 8.4 μM GOx-DNA strand and 12 μM aptamer strand. The solution was dropcast in the split channel on the unfolded device, washed with 0.01 M PBS buffer (pH 7.4) containing 0.1% BSA, and dried in air.

To assemble the origami paper analytical devices (oPADs), the paper was folded by hand. The folded paper device was placed in a thermal laminating pouch, and the pouch was sealed at the edge of the paper device using the impulse thermal edge sealer. Three holes were punched on one side of the pouch. One of the holes was used as inlet and the other two were used to accommodate ohmic contact of the carbon electrodes to two copper wires using Ag adhesive. Five-minute epoxy was used to reinforce the contact.

To use the device for electrochemical sensing, a 20 μL sample aliquot was loaded at the inlet of the oPAD. After 10 min, when the sample fills the whole channel, the oPAD was

put on a breadboard. The current generated from it was measured by a Sinometer VA18B digital multimeter (DMM), and simultaneously the charge was accumulated on the capacitor. After 60 s, the switch was closed so that the capacitor discharges toward the DMM instantaneously. The DMM we used has a max/min button. If the button is pressed once, it only displays the maximum value of measurements. Based on this, the magnitude of the maximum discharge current from the capacitor was recorded. The rate at which DMM measures current depends on conversion rate of analog-to-digital converter, which is usually in the range of 1 - 100 s⁻¹. Although there is no way to measure the conversion rate, the time interval between two current measurements for the DMM used in these studies is about 0.1 s. This means the conversion rate should be > 10 s⁻¹.

Fluorescence measurements on the paper fluidic devices were made using a Typhoon Trio fluorescence imager (GE Healthcare, Piscataway, NJ). To quantify these results, the images were imported into Adobe Photoshop CS2 and transferred to gray-scale mode. The mean fluorescence intensity was determined from the image histogram for each detection reservoir, and then it was background-corrected by subtracting the average intensity measured at the center of the paper where no adenosine was present.

5.4 Results and Discussion

The second generation *o*PAD (*o*PAD 2) reported here is comprised of two layers as shown in Figure 5.2a. On the first layer, an inlet and a pair of identical channels originating at the inlet, were fabricated by wax printing.⁹⁶ On the second layer, two electrodes were fabricated by screen printing conductive carbon ink onto the paper. An additional fluidic inlet is also present on the second layer, and it can be used for adding additional sensing layers in the future. As discussed previously, incorporation of additional sensing layers to the *o*PADs does not require much fabrication overhead.⁹⁸ When the paper is folded at the predefined fold line, the electrodes contact the end of the fluidic channel where the two channels recombine to form two half cells connected by a thin fluidic channel that acts as a salt bridge. This strategy avoids direct printing of the electrodes onto the channel architecture, which would render the channels hydrophobic due to the binder present in the carbon ink.

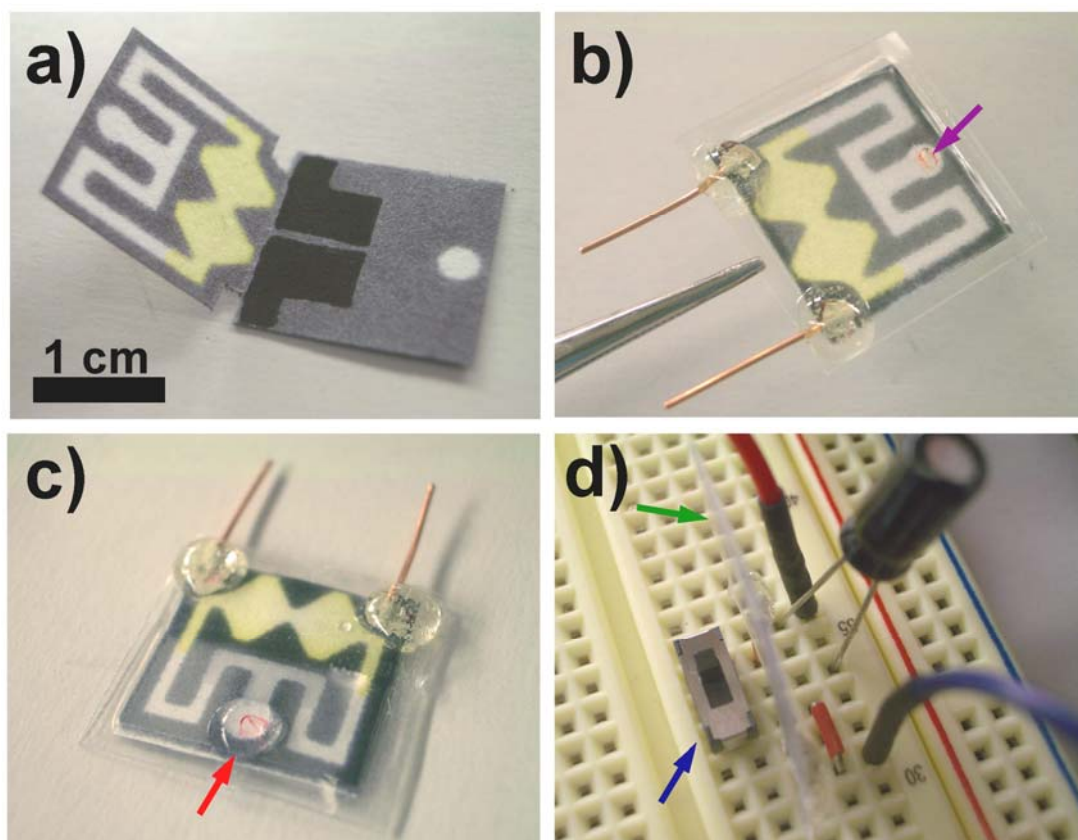


Figure 5.2. (a) A photograph of the unfolded oPAD fabricated by wax printing on chromatography paper. The two screen-printed carbon electrodes are visible on the bottom layer. The yellow color arises from the presence of $\text{Fe}(\text{CN})_6^{3-}$ preloaded in the channel for the electrochemical assay. (b) A photograph of the folded oPAD encapsulated in plastic using thermal edge lamination. The purple arrow indicates an opening for sample introduction, and the two copper wires are for electrical read-out. (c) A photograph of the oPAD after introducing a 20 μL sample at the inlet

(red arrow). The solution flows into the oPAD and splits into two channels. (d) A photograph of a 2.2 μF capacitor, a switch (blue arrow), an oPAD (edge view, green arrow), and jumper wires on a breadboard for measuring the output current of the device using a DMM and simultaneously accumulating charge onto the capacitor.

To test this general approach, we first constructed a concentration cell using the following methodology. GOx was preloaded in one of the channels, and then a solution containing 12 μL of 100 mM glucose and 100 mM $\text{Fe}(\text{CN})_6^{3-}$ in 0.01 M PBS buffer (pH 6.0) was loaded into both halves of the electrochemical cell. After drying in the dark, the device was folded and then encapsulated in plastic by impulse edge thermal lamination. As shown in Figure 5.2b, the oPAD was fully enclosed with the exception of a small opening for sample loading (marked by a purple arrow) and two copper leads that connected to the carbon electrodes. Note that lamination ensures vertical contact between adjacent layers, which eliminates the need for the type of metal clamp used in our earlier work.⁹⁸ After assembly of the oPAD, 20 μL of 0.01 M PBS buffer (pH 7.4) was introduced through the inlet (Figure 5.2c). After 10 min, when the fluid recombined in the electrochemical cell, the oPAD was placed onto a breadboard, as shown in Figure 5.2d. The electric circuit on the breadboard was designed to measure the current generated by the oPAD using the DMM while simultaneously accumulating the resulting charge on the capacitor. Of course, in the future, the capacitor would be directly fabricated on paper and integrated into the

laminated package. Upon closing the switch, the capacitor quickly discharges, and the resulting maximum current is recorded by the DMM. Information about the sampling frequency of the DMM is provided in the Experimental Section. The important point is that the magnitude of the discharge current increases linearly with increasing concentration of GOx (Figure 5.3), thereby demonstrating the applicability of the sensor to quantification. Note that making use of the capacitor discharge current increases the sensitivity of the assay by 15.5-fold compared to a simple current measurement (4.1 $\mu\text{A}/\text{pmol}$ vs. 0.26 $\mu\text{A}/\text{pmol}$, Figure 5.3).

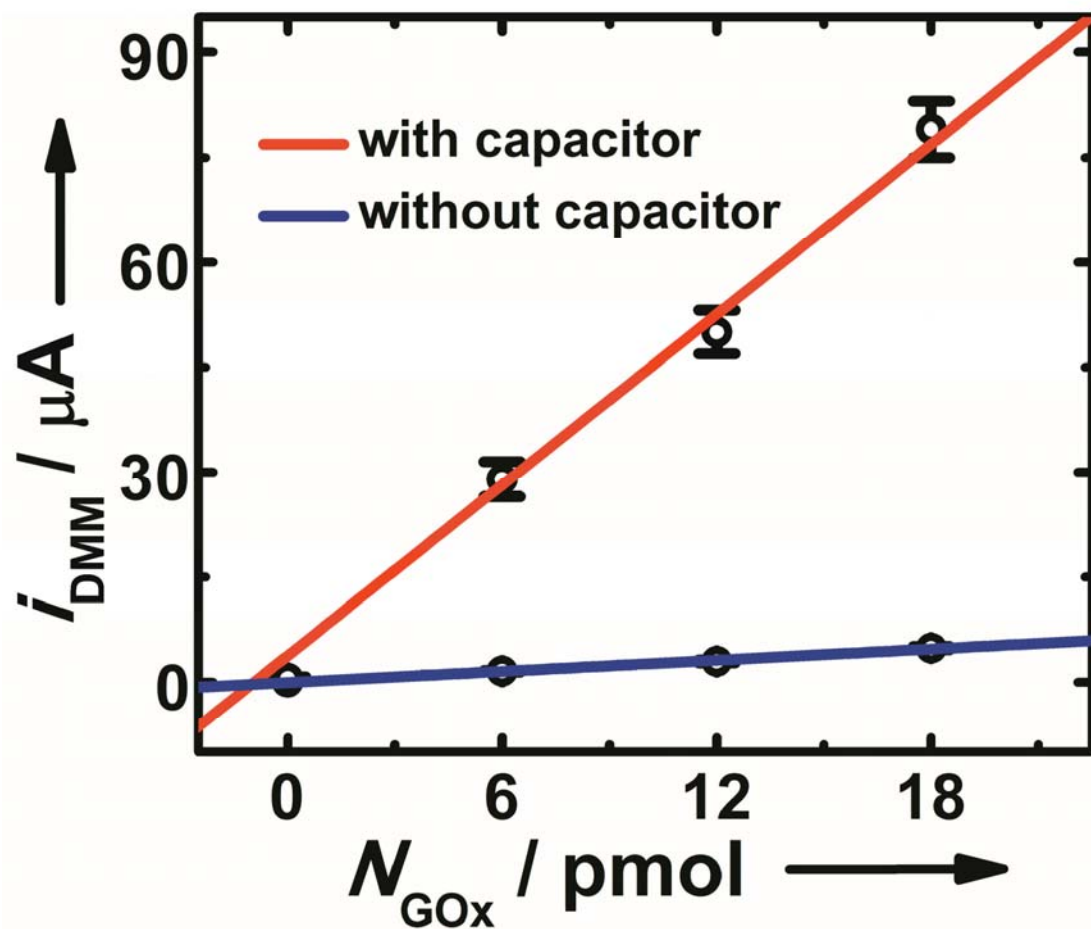


Figure 5.3. Calibration curve for detection of GOx using the oPAD with and without amplification by a capacitor. The error bars represent standard deviation of readings from a DMM for three measurements.

With these promising preliminary results in hand, we carried out a heterogeneous aptamer assay. Biotin-labeled aptamers for adenosine^{77,100,101} were immobilized on 10 μm -diameter polystyrene (PS) microbeads functionalized on their surface with streptavidin. It was possible to keep track of the location of the microbeads, because they contained fluorescent Nile Red. A 0.10 μL aliquot of the 0.25% (w/v) microbead solution was added to one of the channels and allowed to dry. To ensure that the microbeads did not move in the paper channels, we carried out the following simple experiment. First, the entire unfolded device was imaged in a fluorescence scanner to locate the beads (Figure 5.4a). Next, the device was folded and a PBS solution (0.01 M, pH 7.4) was added to the device inlet and allowed to flow to its end. Finally, the device was imaged a second time (Figure 5.4b). The results show minimal (and acceptable) bead displacement after exposure to the buffer solution.

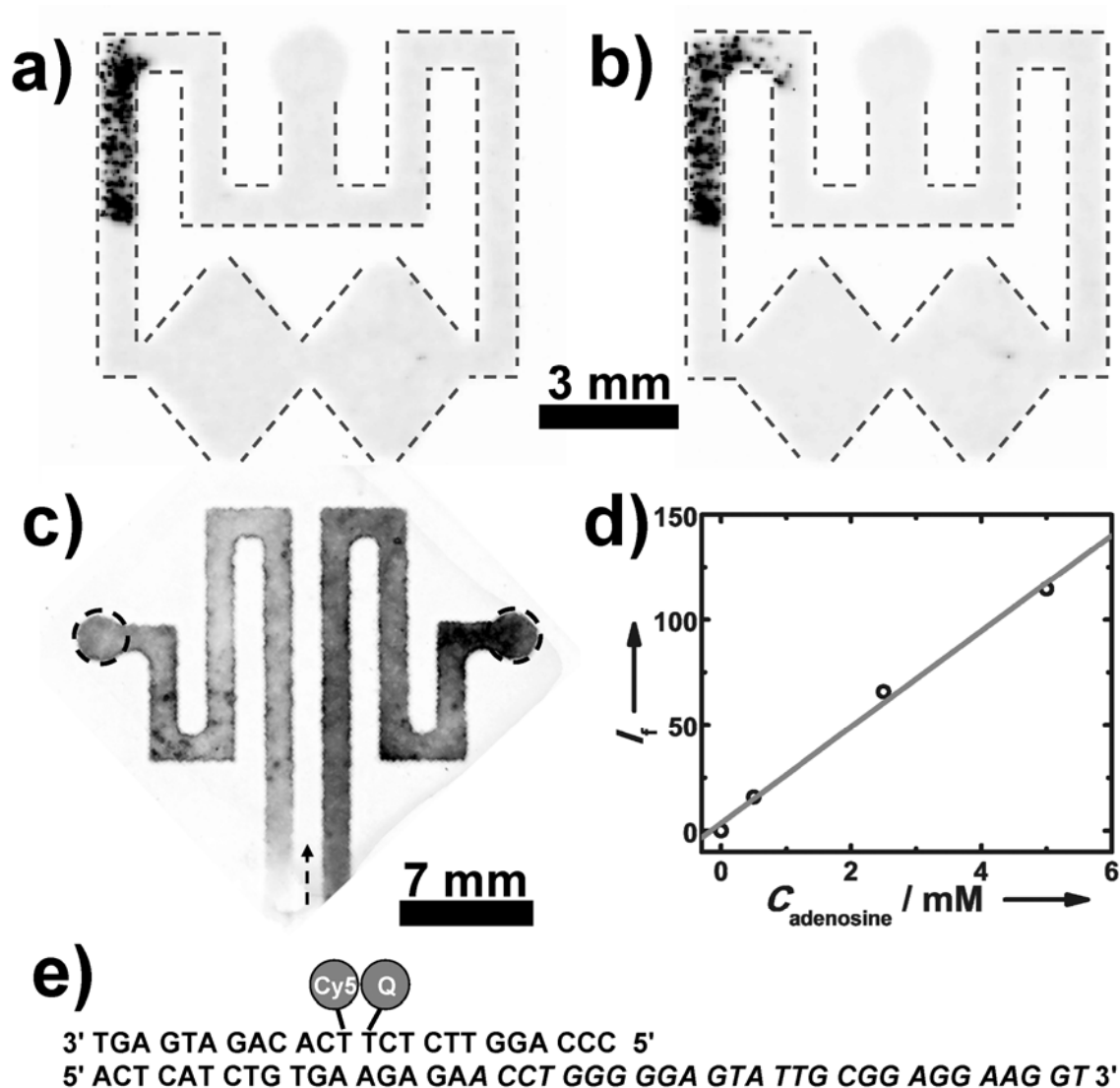


Figure 5.4. (Top row) Fluorescent images of the oPAD showing 10 μm fluorescent microbeads preloaded in one split channel (a) before and (b) after the introduction of 0.01 M PBS buffer (pH 7.4) at the inlet. For clarity, the channels are outlined using dash lines. (c) A fluorescence image of a paper fluidic device having two channels preloaded with 15

μL of a solution containing $0.32\ \mu\text{M}$ adenosine aptamer strand, $0.20\ \mu\text{M}$ fluorophore strand, and $0.40\ \mu\text{M}$ quencher strand. The right channel was filled with $15\ \mu\text{L}$ of $0.01\ \text{M}$ PBS buffer (pH 7.4) containing $5\ \text{mM}$ adenosine, and the left channel was filled with $15\ \mu\text{L}$ of adenosine-free PBS. The arrow shows the flow direction. The darker color in the right channel represents enhanced fluorescence due to the presence of adenosine. (d) A plot of fluorescent intensity (I_f) versus the concentration of adenosine ($C_{\text{adenosine}}$) in the sample. The intensity was measured in the right circle shown in (c) and subtracted from the intensity measured in the left circle. (e) Sequences of aptamer strand, the fluorophore strand, and the quencher strand. The sequence for binding to adenosine is in italics.

Heterogeneous assays generally require longer incubation times than homogeneous assays due to reduced mass transfer of reagents to the immobilized probes. Longer assay times can be a problem for paper devices due to water evaporation, but this issue has been addressed by encapsulating the device in an impermeable enclosure. For example, pressure-sensitive adhesives^{95,97} or printer toner⁹⁶ have been used for this purpose. We used a glossy and clear plastic envelope sealed with an impulse thermal edge laminator that only applies heat to the edge of the plastic. This approach avoids adhesives,^{95,97} which can lead to contamination or nonspecific adsorption of reagents or targets, and heat-induced deactivation.⁹⁶ Using this approach, we found that the channel stays wet in the enclosed device at 37 °C for > 2 h (Figure 5.5). To demonstrate the function of the aptamer probe in the enclosed *o*PADs, a fluorescent adenosine aptamer sensor (Figure 5.4e) was tested in the device. Adenosine is a crucial biological cofactor in many biological processes, such as those involved in kidney function. Normal levels of urinary adenosine are in the micromolar range, and elevated renal adenosine levels can be characteristic of disease.¹⁰² As shown in Figure 5.4c, two separate channels were

preloaded with 15 μL of aptamer solution containing 0.32 μM adenosine aptamer strand, 0.20 μM fluorophore strand and 0.40 μM quencher strand, and then the channels were allowed to dry in air. Next, a 15 μL buffer solution containing 5 mM adenosine was introduced into one of the channels, and buffer only was added to the other channel. After 15 min the fluorescence from both channels was measured. As shown in Figure 5.4c, fluorescence is enhanced in the channel where adenosine is present. Moreover, there is a linear relationship between the fluorescence intensity and the adenosine concentration between 0.5 mM to 5 mM.

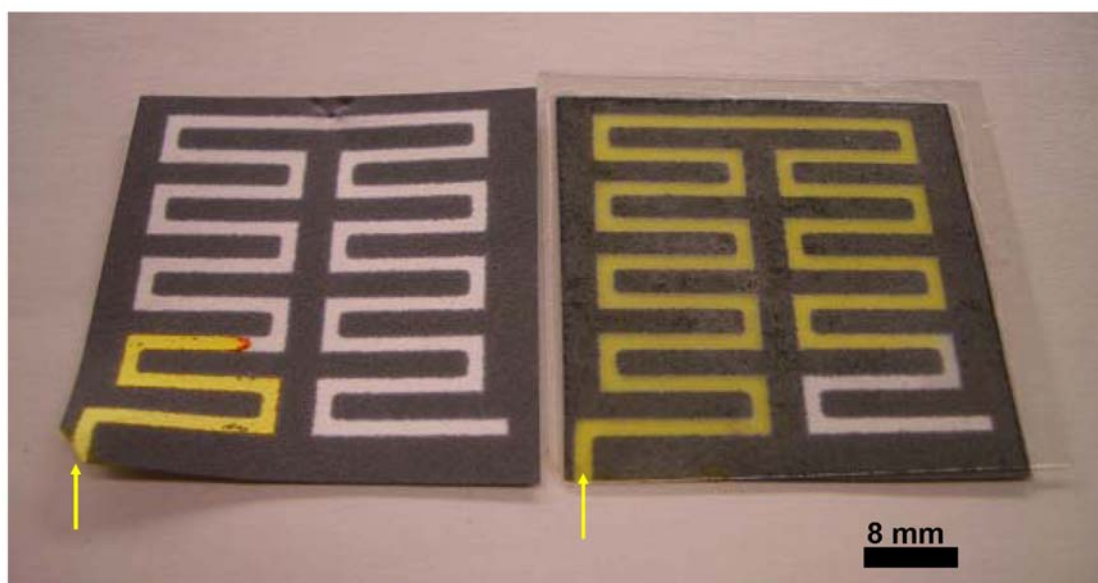


Figure 5.5. Photograph of two paper fluidic devices. The one on the left was open to the air, and the one on the right was encapsulated by thermal lamination. The devices were placed in an oven at 37 °C, and the openings at the bottom-left corner (marked by the yellow arrows) were dipped into 0.01 M PBS solution (pH 7.4) containing 0.1 mM tartrazine. It took more than 2 h for the solution to fill the entire channel on the right. This experiment shows that lamination prevents evaporation over the time required to carry out the assays reported in the main text.

For electrochemical read-out, we used 5' biotin-modified DNA (bDNA). The biotin group was used to link streptavidin-labeled GOx (sGOx). The sequences are shown in Figure 5.6b. UV-vis spectroscopy was used to characterize the product. Details about the synthesis, characterization and UV-vis spectra (Figure 5.1) are available in the Experimental Section. The key point is that bDNA binds to sGOx which is separated from free bDNA by centrifugal filtering. The whole process to make an μ PAD for electrochemical detection of adenosine is provided in the experimental section. The current increased with increasing adenosine concentration. The detection limit, calculated as 3-times the standard deviation of the blank divided by the slope, is 11.8 μ M. The sensitivity (0.48 μ A/ μ M) was enhanced by 17-fold compared to that without amplification (0.029 μ A/ μ M).

5.5 Summary and Conclusions

In this chapter, we have reported a μ PAD-type device that utilizes aptamers as the sensing probe and very simple electrochemical (DMM) read-out. The fabrication of the device is fast, easy, and inexpensive, and all fabrication steps could be easily automated. The sensor is self powered

in that it generates a current without the need for an external power source.⁷⁴ DMMs are ubiquitous and can be purchased for as little as \$US30. Moreover, DMMs integrated with an iPhone or iPod (known as iMultimeter) are now available.¹⁰³ Although we used an adenosine aptamer for this proof-of-concept study, a range of probes, including, antibodies, DNAzyme, or aptazymes, could also be integrated into the device using the same sensing platform. We believe the oPAD 2 will prove promising for applications such as point-of-care diagnosis and unambiguous sensing under resource-limited settings.

Chapter 6: Determination of Percent Hemoglobin A1c Using a Potentiometric Method

6.1 Synopsis

In this chapter we report a potentiometric method for measuring hemoglobin A1c (HbA1c, glycated hemoglobin) concentration, hemoglobin (Hb) concentration, and percent HbA1c (%HBA1c) in human blood. The %HBA1c is important for diagnosis and management of diabetes mellitus. Alizarin red s (ARS) is used as a redox indicator. Phenylboronic acid (PBA) binds to both ARS and HbA1c via diol-boronic acid complexation. The binding of PBA to ARS shifts its redox potential negative. However, when HbA1c competes with ARS for PBA binding, the solution potential shifts positive. This shift is linked to the HbA1c concentration. To determinate the concentration of Hb, Hb is allowed to react with $\text{Fe}(\text{CN})_6^{3-}$. The potential shift arising from the reduction of $\text{Fe}(\text{CN})_6^{3-}$ by Hb is proportional to the logarithm of the Hb concentration. The results obtained for %HBA1c in human blood are in good agreement with those determined using a reference method.

6.2 Introduction

Diabetes mellitus is a growing worldwide health problem.²³ Diagnosis and management of this disease require continuous monitoring of blood glucose level, usually using personal glucose meters (PGMs).²⁴ However, effective management requires three to four tests a day owing to the large fluctuation of glucose level, and hence this type of spot testing does not reflect average blood glucose level over a prolonged period. For the latter type of determination, testing for percent hemoglobin A1c (glycated hemoglobin, %HbA1c), which is the ratio of HbA1c to total hemoglobin (Hb) concentration, is more appropriate.²⁶

HbA1c is formed by a nonenzymatic reaction between blood glucose and the N-terminal valine of the Hb chain, followed by an Amadori rearrangement reaction.²⁸ The correlation between %HbA1c and average blood glucose level is well established.²⁵ Specifically, the %HbA1c provides a running average of the blood glucose level over the half-life of erythrocytes (i.e., ~60 days) and has therefore been recognized as a crucial parameter for the diagnosis and management of diabetes mellitus.²⁵ The 2010 American Diabetes Association Standards of Medical Care in Diabetes has included $\text{\%HbA1c} \geq 6.5\%$ as a criterion for the diagnosis of diabetes mellitus.²⁷

A wide range of methods have been developed for the determination of %HbA1c, including boronate affinity chromatography,^{29,30} ion-exchange chromatography,³¹ electrophoresis,³² fluorescence,^{33,34} UV-vis absorption,³⁴ chemiluminescence,²⁸ electrochemical methods,³⁵⁻³⁹ and immunoassays.^{40,41} However, most of these methods are based on chromatographic separations. Other methods usually require antibody reagents or commercially unavailable derivatives of boronic acid, which render these methods relatively vulnerable and expensive.^{28,33,34,38,40,41} Moreover, some of these methods only determine the absolute concentration of HbA1c rather than %HbA1c. Finally, it has recently been reported that the majority of commercially available HbA1c analyzers are unreliable.⁴²

Electrochemical methods, because of their low cost and simplicity, are particularly amenable to point-of-care sensing.^{19,99} For example, we previously reported electrogenerated chemiluminescent detection of HbA1c using a microelectrochemical bipolar electrode array on a microfluidic chip.³⁷ As discussed earlier, however, this approach leads to the absolute concentration of HbA1c rather than the more useful %HbA1c. Here, we report a method based on potentiometry for determination of HbA1c concentration, Hb concentration, and thus %HbA1c in human blood. The method

is simple, requires no separation, and all necessary reagents are inexpensive, stable (not biological), and commercially available. The quantitative determination of HbA1c is based on measuring the potential shift of a redox indicator, alizarin red s (ARS, US\$ ~2.1/g). When ARS binds to phenylboronic acid (PBA, US\$ ~2.3/g) through diol-boronic acid complexation, the redox potential shifts negative. In the presence of HbA1c, which is a competitor of ARS for PBA binding, the potential shifts back positive. The magnitude of this back shift is used for the quantification of HbA1c. For the determination of total Hb, the blood sample is allowed to react with $K_3Fe(CN)_6$, and the potential shift owing to the reduction of $K_3Fe(CN)_6$ by Hb is correlated quantitatively to the Hb concentration.

6.3 Experimental

Chemicals and materials Lyophilized Hb standard (13.2 g/dL) and an HbA1c calibrator kit with four lyophilized Hb samples containing 5.0, 8.0, 10.8, and 14.8% of HbA1c, respectively, were purchased from Pointe Scientific, Inc. (Canton, MI). The concentrations of total Hb in the HbA1c calibrator samples were determined using UV-vis spectroscopy by comparing the adsorption at 415 nm with Hb standards. The absolute concentration of HbA1c was then obtained by

multiplying the total Hb concentration and the %HbA1c. ARS, $\text{K}_3\text{Fe}(\text{CN})_6$ (99+%) and N-ethylmorpholine (99%) were purchased from Acros Organics. PBA ($\geq 97\%$) were purchased from Sigma-Aldrich. KCl and HCl were purchased from Fisher Scientific. All solutions were prepared using deionized water (18.0 $\text{M}\Omega\cdot\text{cm}$, Milli-Q Gradient System, Millipore). All reagents were used as received.

Electrochemical measurements All electrochemical measurements were made using a CHI650c potentiostat from CH Instrument (Austin, TX). For cyclic voltammetry (CV) and linear sweep voltammetry (LSV), a glassy carbon working electrode (3.0 mm in diameter), a Ag/AgCl reference electrode, and a platinum counter electrode were used. For potentiometric measurements, only the glassy carbon electrode and the Ag/AgCl electrode were required. The Ag/AgCl reference electrode was filled with saturated KCl solution. Before all electrochemical measurements, the glassy carbon electrode was polished with slurries of alumina (300 nm and then 50 nm) using a MetaServ-3000 polisher from Buehler (Lake Bluff, IL), rinsed with deionized water, and dried under nitrogen.

Determination of the dissociation constant of ARS-PBA
The dissociation constant for ARS-PBA complexation was

determined by nonlinear fitting of a titration curve using Origin 8.0 with the function given in eq 1.¹⁰⁴

$$C_{\text{PBA}} = C_{\text{ARS}}(j - j_0)/(j_{\infty} - j_0) + K_d(j - j_0)/(j_{\infty} - j) \quad (1)$$

Here, C_{PBA} is the total concentration of PBA and C_{ARS} is the total concentration of ARS. The measured peak current density is j , which is proportional to the concentration of free ARS. The peak current density measured in the absence of PBA is j_0 . The peak current measured when PBA is in excess j_{∞} .

Potentiometric detection of HbA1c 100 μL of the Hb sample was mixed with 50 μL of 0.10 M N-ethylmorpholine buffer (pH adjusted to 8.5 using HCl) containing 1.0 mM ARS and 0.10 M KCl in a glass vial with stirring (the ARS stock solution was freshly prepared each day). The solution was diluted to 500 μL using 0.10 M N-ethylmorpholine buffer (pH 8.5) containing 0.10 M KCl. The open-circuit potential (OCP) of the stirred solution was measured for a total of 1180 s at a sampling rate of 10/s. At 1000 s, 1.0 μL of 2.0 M PBA dissolved in ethanol was added into the glass vial. The resulting potential shift was recorded and the dose-response curve was plotted for the determination of the HbA1c concentration.

Potentiometric detection of total Hb 3.0 mL of 0.010 M PBS solution (pH 7.4) containing 10 mM $K_3Fe(CN)_6$ was freshly prepared and added into a glass vial with stirring. The OCP was measured at a sampling rate of 10/s while stirring. At 60 s, 3.0 μ L of Hb sample was added into the glass vial. After 200 s, an additional 3.0 μ L aliquot of the Hb sample was added into the glass vial. The resulting potential shift during the second addition of sample was used for the determination of the total hemoglobin concentration.

6.4 Results and Discussion

Electrochemistry of ARS and ARS-PBA. Schumacher et al. have examined the electrochemistry of ARS and ARS-PBA using CV, and they also used ARS as an amperometric indicator for studying the binding between PBA and fructose in phosphate buffer (pH 7.4).¹⁰⁵ The binding between diols and boronic acid is generally believed to be more favorable at higher pHs,¹⁰⁶ and therefore we used 0.10 M N-ethylmorpholine buffer (pH 8.5) containing 0.10 M KCl supporting electrolyte for all electrochemical experiments involving ARS. At pH 8.5, it is known that the 3-hydroxy group of ARS is deprotonated,¹⁰⁷ as shown in Figure 6.1.

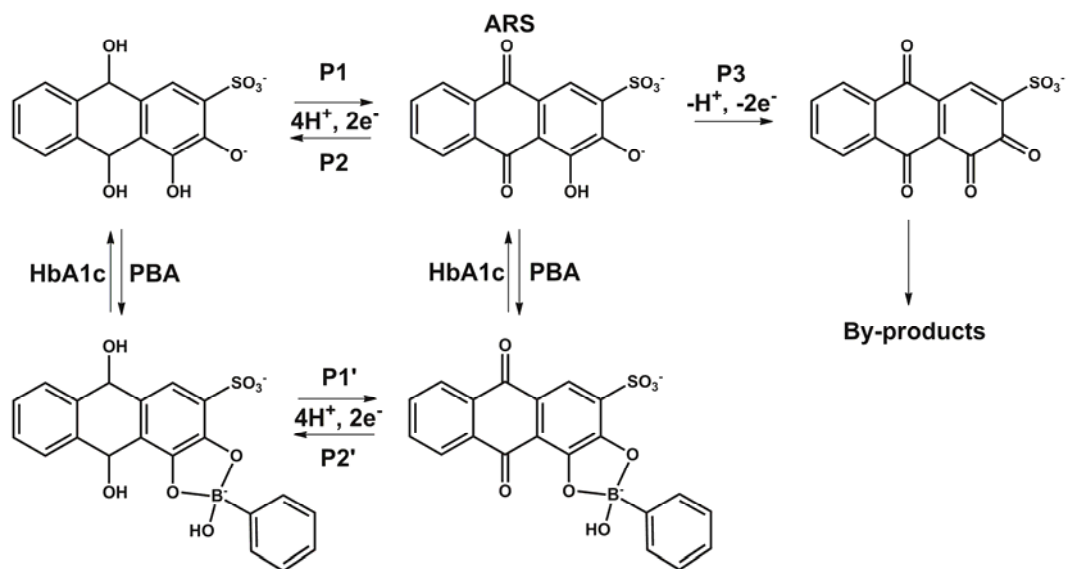


Figure 6.1. Reaction scheme showing the complexation and redox processes used for the HbA1c assay. P1, P2, P1', P2', and P3 correspond to the redox processes identified in Figure 6.2.

A CV of 1.0 mM ARS is shown in Figure 6.2a (black curve). A nearly reversible process is observed at $E_{1/2} = -704$ mV with $\Delta E = 53$ mV (P1 and P2 in Figure 6.2a). Recall that $E_{1/2} = (E_{pc} + E_{pa})/2$ and $\Delta E = E_{pc} - E_{pa}$ where E_{pc} and E_{pa} are the potentials corresponding to the cathodic and anodic current density peaks, respectively. An irreversible process is detected at $E_{pa} = 301$ mV (P3 in Figure 6.2a). The nearly reversible and the irreversible processes are attributable to the 2-proton-2-electron redox reactions of the orthoquinone moiety and the oxidation of the dihydroxyl moiety of the ARS, respectively (Figure 6.1).¹⁰⁵ The peak at $E_p = -592$ mV corresponds to the reduction of oxygen. This assertion is confirmed by Figure 6.3, which shows that this peak is absent in a deoxygenate solution. All subsequent electrochemical measurements were carried out in air-saturated solutions, because it is difficult to deoxygenate hemoglobin solutions.

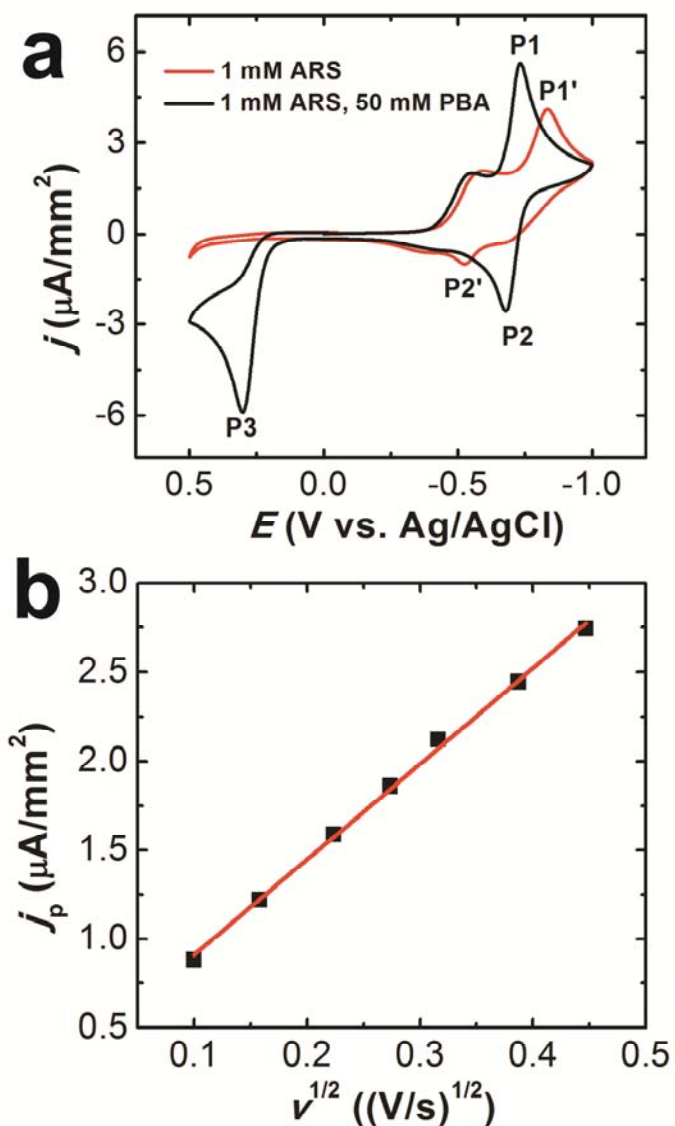


Figure 6.2. (a) CVs obtained in solutions containing 0.10 M N-ethylmorpholine buffer (pH 8.5), 1.0 mM ARS, and 0.10 M KCl. 50 mM PBA was added to this solution to obtain the red CV. Scan rate: 0.100 V/s. (b) Plot of peak current density (P3) as a function of the square root of scan rate.

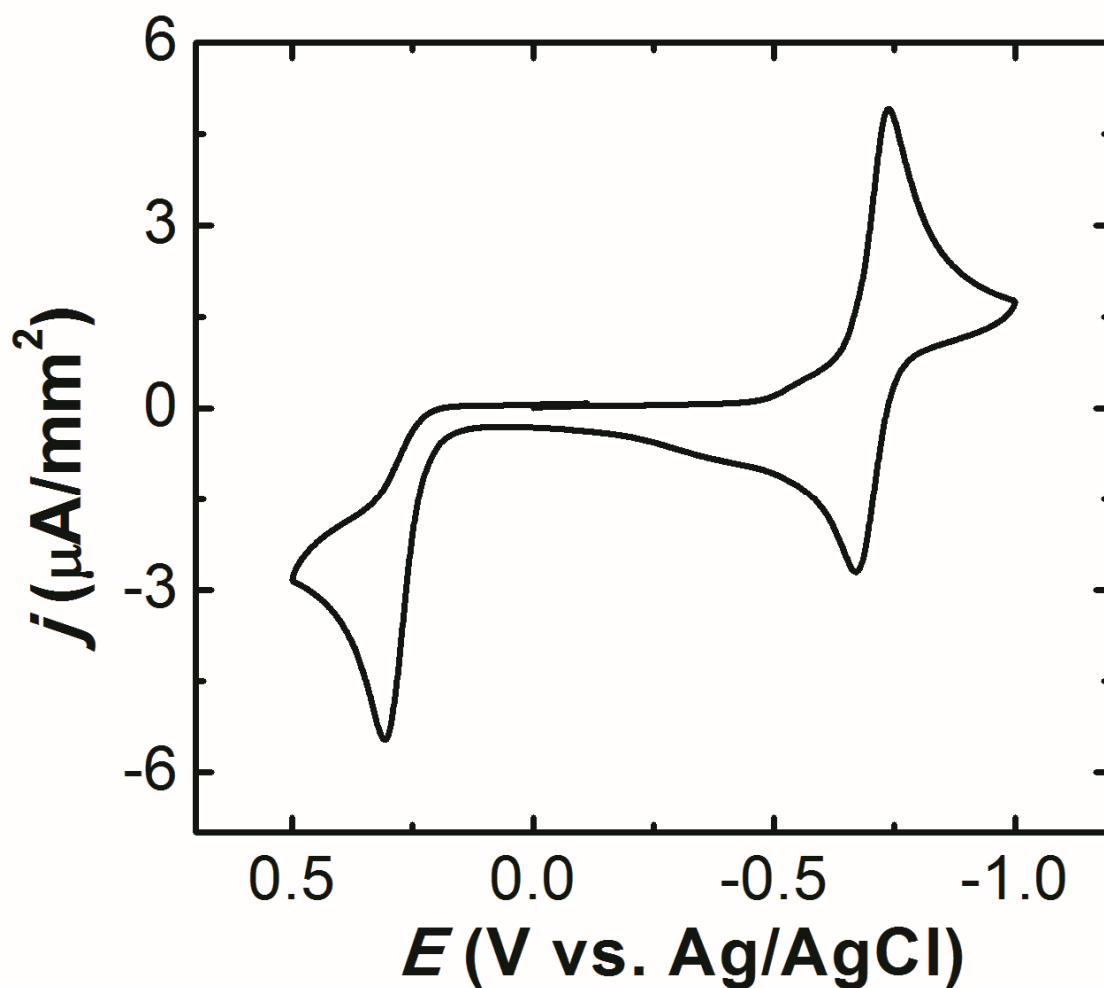


Figure 6.3. CV obtained in 0.10 M N-ethylmorpholine buffer (pH 8.5) containing 1.0 mM ARS and 0.10 M KCl. The solution was deoxygenated by bubbling nitrogen for 40 min. Scan rate: 0.100 V/s.

When 50 mM PBA is added to the 1.0 mM ARS solution, the voltammetry changes (red curve, Figure 6.2a). In this case, peak P3 is not present due to complexation between ARS and PBA via the diol-boronic acid interaction (Figure 6.1). Furthermore, the peak potentials of the orthoquinone redox process (P1' and P2' in Figure 6.2a) shift, they become more irreversible ($\Delta E=310$ mV and $E_{1/2}=-679$ mV), and the ORR shifts slightly negative ($E_p=-592$ mV).

As shown in Figure 6.2b, the peak current density arising from the dihydroxyl oxidation of ARS (peak P3) is proportional to the square root of the scan rate (10-200 mV/s), indicating that the redox reaction is diffusion limited.⁶¹ Therefore, the magnitude of peak current density P3 is proportional to the bulk concentration of free ARS in the solution, and hence it can be used to study the binding between ARS and PBA.

Complexation of ARS and PBA. A detailed fluorescence study of the complexation between PBA and a range of diols, including ARS, was reported by Wang et al.¹⁰⁶ One outcome of this study is that the pH and solution composition greatly influence the binding of PBA and diols.¹⁰⁶ Generally, the interactions are favored at high pHs when the boronic acid

is tetrahedral and negatively charged, as shown in Figure 6.1.¹⁰⁶

To determine the time required for the ARS-PBA complexation reaction to take place under electrochemical conditions, 10 μ L of 1.0 M PBA dissolved in ethanol was added to 10 mL of 0.10 M N-ethylmorpholine buffer containing 1.0 mM ARS and 0.10 M KCl. LSVs were obtained as a function of time, and the resulting peak current densities, j_p , as a function of time are presented in Figure 6.4a. The results show that the magnitude of the anodic current density decreases quickly with time, but after ~20 min achieves a plateau. Therefore, a reaction time of 20 min was used for the following experiments to determine the dissociation constant for the ARS-PBA complex.

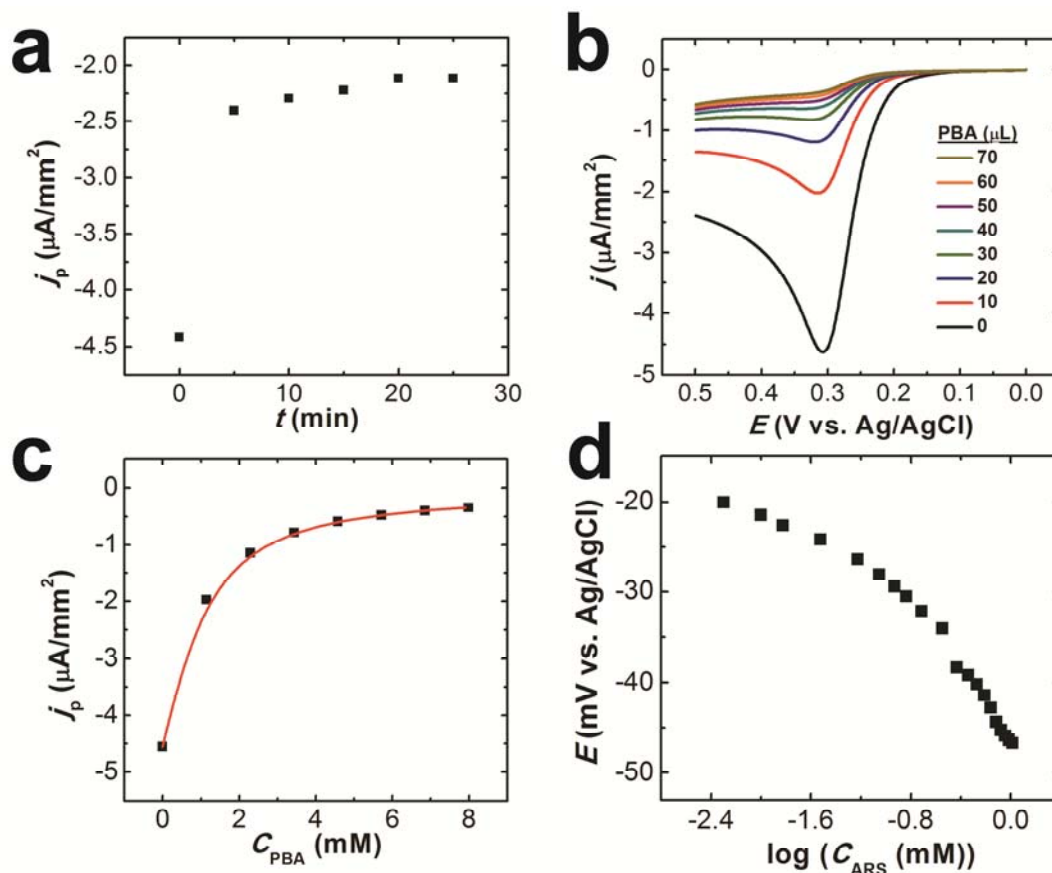


Figure 6.4. (a) Plot of peak current density (P3, Figure 6.2a) as a function of time measured in a solution containing 0.10 M N-ethylmorpholine buffer (pH 8.5), 1.0 mM ARS, 1.0 mM PBA, and 0.10 M KCl. Scan rate: 0.100 V/s. (b) LSVs obtained in a solution containing 0.10 M N-ethylmorpholine buffer (pH 8.5), 1.0 mM ARS, and 0.10 M KCl, and titrated with 10 μL aliquots of 1.0 M PBA dissolved in ethanol. Scan rate: 0.100 V/s. The total volume of PBA added is shown in legend. (c) Plot of peak current density (Figure

6.2b) as a function of PBA concentration. The red curve is a non-linear fit obtained using eq 1. (d) Plot of potential measured in a solution containing 0.10 M N-ethylmorpholine buffer (pH 8.5) and 0.10 M KCl as a function of the logarithm of the concentration of added ARS.

To determine the dissociation constant of the ARS-PBA complex, 10 μL of 1.0 M PBA dissolved in ethanol was added to 10 mL of 0.10 M N-ethylmorpholine buffer containing 1.0 mM ARS and 0.10 M KCl every 20 min. The resulting LSVs and corresponding titration curve are shown in Figures 6.4b and 6.4c, respectively. With increasing concentration of PBA, the anodic peak current density of the irreversible dihydroxyl oxidation (P3 in Figure 6.2a) decreases. The titration curve was fitted using eq 1, and the dissociation constant of the ARS-PBA complex was determined to be $(5.63 \pm 0.05) \times 10^{-4}$ M.

Potentiometric determination of HbA1c. The detection limit of potentiometric methods can be significantly lower than for LSV, and therefore this approach has been used to quantify trace amounts of analytes and weak interactions between molecules. For example, Shoji et al.¹⁰⁸ used potentiometry to determine the concentration of saccharides based on the binding of saccharides to poly(aniline boronic acid) (PABA)-modified glassy carbon electrodes. Like ARS, the electrochemistry of PABA involves both proton and electron transfers. Accordingly, complexation between saccharides and PABA shifts the redox potential due to changes in both the pK_a and the formal potential of PABA.

Specifically, formation of a negatively charged complex between the diols and boronic acid increases electron density and thus shifts the formal potential negative. However, the negative charge also decreases acidity, and thus shifts the redox potential positive. In this case, the shift of the pK_a is dominant.

In analogy to the saccharide/PABA system, we hypothesized that the binding of PBA to ARS might also change the redox potential of ARS and that this could be used to measure the competitive binding of HbA1c to PBA. Accordingly, we first measured the potential of a solution containing 0.10 M N-ethylmorpholine buffer (pH 8.5), 0.10 M KCl, and increasing concentrations of ARS. As shown in Figure 6.4d, the potential of this solution shifts negative with increasing ARS concentration. The correlation between potential and the logarithm of ARS concentration is not linear, because only one-half of the redox couple is present.

Next, we titrated a solution of the same composition (0.10 M N-ethylmorpholine and 0.10 M KCl), but this time containing 0.10 mM ARS, with aliquots of 2.0 M PBA dissolved in ethanol. As shown in Figure 6.5, the potential shifts negative, from 3.85 mV to 0.49 mV, with increasing concentration of PBA. Because PBA is redox inactive, the shift in potential should be due to the formation of an ARS-

PBA complex. The negative direction of the potential shift suggests that it is controlled by the change in the formal potential of ARS complex rather its pK_a .

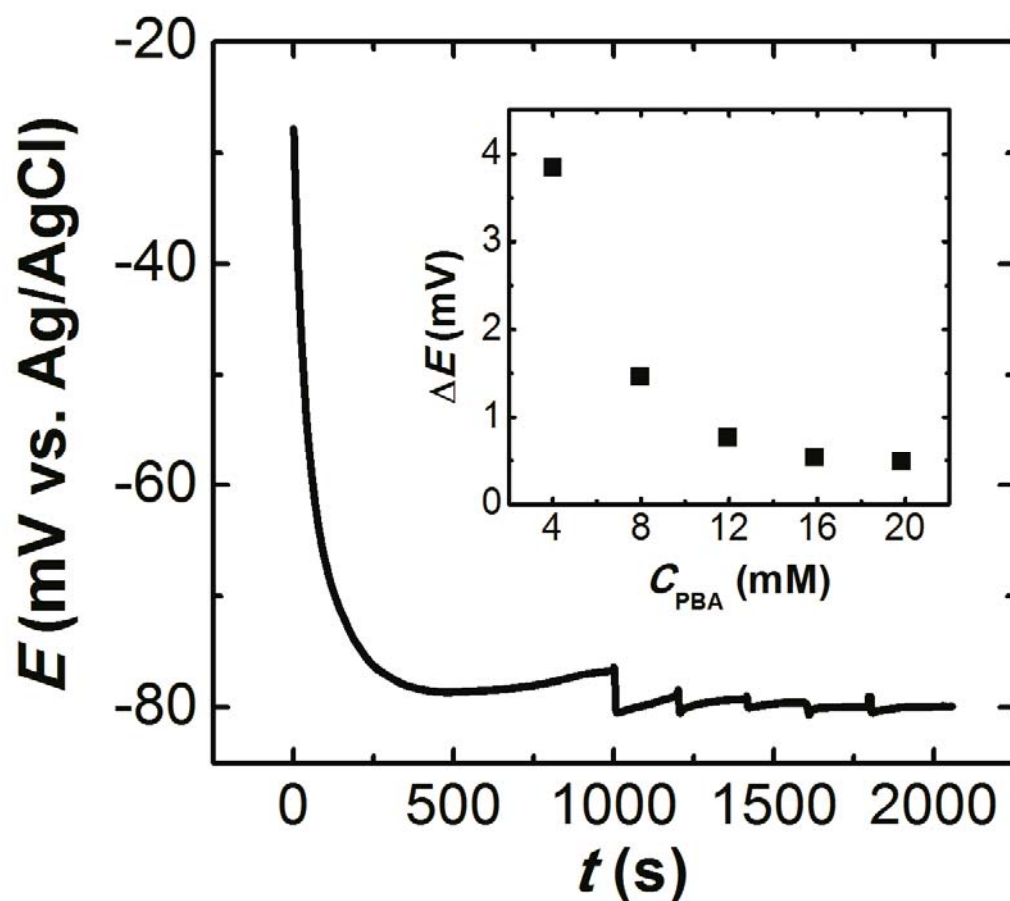


Figure 6.5. Potential measured in 500 μL of 0.10 M N-ethylmorpholine buffer (pH 8.5) containing 0.10 mM ARS and 0.10 M KCl. Starting at $t = 1000$ s, 1.0 μL aliquots of 2.0 M PBA in ethanol was added every 200 s. Inset: Plot of the potential shifts measured immediately after each addition of PBA as a function of PBA concentration in the solution.

We hypothesized that HbA1c would compete with ARS for binding to PBA, and hence the presence of HbA1c would alter the potential of a solution containing ARS and PBA. Accordingly, we prepared four solutions containing 0.10 M N-ethylmorpholine buffered at pH 8.5, 0.10 mM ARS, 0.10 M KCl, and different concentrations of HbA1c, and then added 1.0 L of 2.0 M PBA dissolved in ethanol. Figure 6.6 shows that the potential of these solutions quickly shift negative when PBA is added. This behavior is similar to that observed in the absence of HbA1c (Figure 6.5). However, in this case the potential slowly shifts back positive. The higher the concentration of HbA1c, the more the potential shifts, indicating that the potential shift is correlated to the competitive binding of HbA1c to PBA. Because the diffusion of HbA1c is much slower than ARS, due to the much larger size of HbA1c, the rate of formation of the HbA1c-PBA complex is much slower than for the ARS-PBA complex.

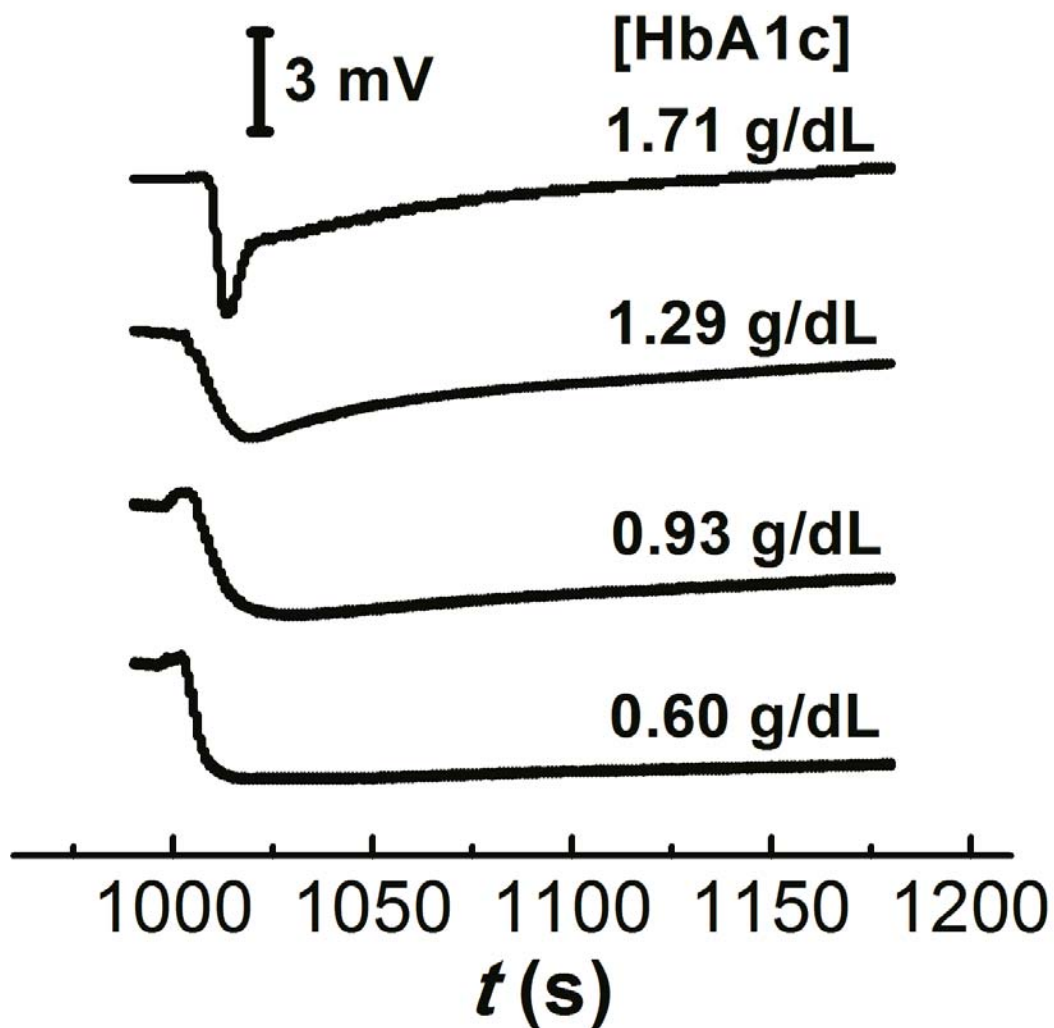


Figure 6.6. Potential as a function of time measured in each of four 500 μL aliquots of 0.10 M N-ethylmorpholine buffer (pH 8.5) containing 0.10 mM ARS, 0.10 M KCl, and 50 μL of HbA1c having the concentrations given in the legend. 1.0 μL of 2.0 M PBA in ethanol was added into the solution at 1000 s.

To quantitatively detect HbA1c, the potential shifts at different times (shown in Figure 6.6a) were plotted vs. the concentration of HbA1c. As shown in Figures 7b-c, ΔE_1 , which corresponds to the initial potential shift resulting from the binding of ARS to PBA, is not correlated to the concentration of HbA1c. However, ΔE_2 and ΔE_3 are clearly correlated to the HbA1c concentration. Specifically, increasing concentrations of HbA1c result in an increase in ΔE_2 from 0.5 mV to 4.0 mV, while ΔE_3 simultaneously decreases from 3.2 mV to 0.1 mV.

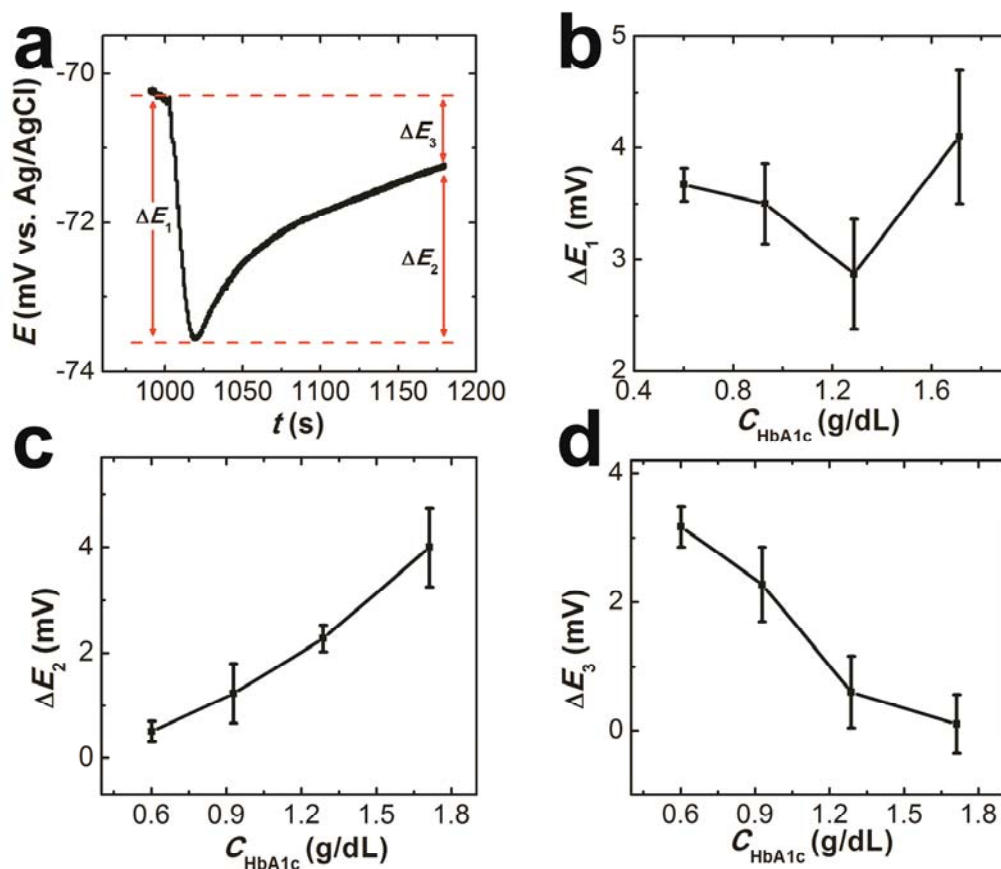


Figure 6.7. (a) Potential measured in 500 μL of 0.10 M N-ethylmorpholine buffer solution (pH 8.5) containing 0.10 mM ARS, 0.10 M KCl, and 50 μL of 1.29 g/dL HbA1c. 1.0 μL of 2.0 M PBA in ethanol was added at 1000 s. The potential shifts at different times are labeled as ΔE_1 , ΔE_2 , and ΔE_3 . (b-d) Plots of (b) ΔE_1 , (c) ΔE_2 , and (d) ΔE_3 as a function of HbA1c concentration. Each ΔE value is an average of three measurements, and the error bars represent standard deviations from the mean.

Determination of total Hb. The absolute concentration of HbA1c doesn't necessarily represent the real value of %HbA1c, because there is a large variation in the total Hb concentration across the population.¹⁰⁹ Therefore, for the determination of %HbA1c, measuring the concentration of total Hb is crucial. In this study we used $\text{Fe}(\text{CN})_6^{3-}$ as an oxidant to convert Hb to methemoglobin¹¹⁰ and $\text{Fe}(\text{CN})_6^{3-}$ to $\text{Fe}(\text{CN})_6^{4-}$. The resulting changes in the relative concentrations of the $\text{Fe}(\text{CN})_6^{3-}/4-$ redox couple leads to a potential shift that is used for quantitative determination of total Hb concentration. As shown in Figure 6.8a, after each addition of Hb into 0.010 M PBS buffer (pH 7.4) containing 10 mM $\text{Fe}(\text{CN})_6^{3-}$, the potential shifts quickly negative. A linear correlation between the potential shift and the logarithm of the Hb concentration is observed (Figure 6.8b).

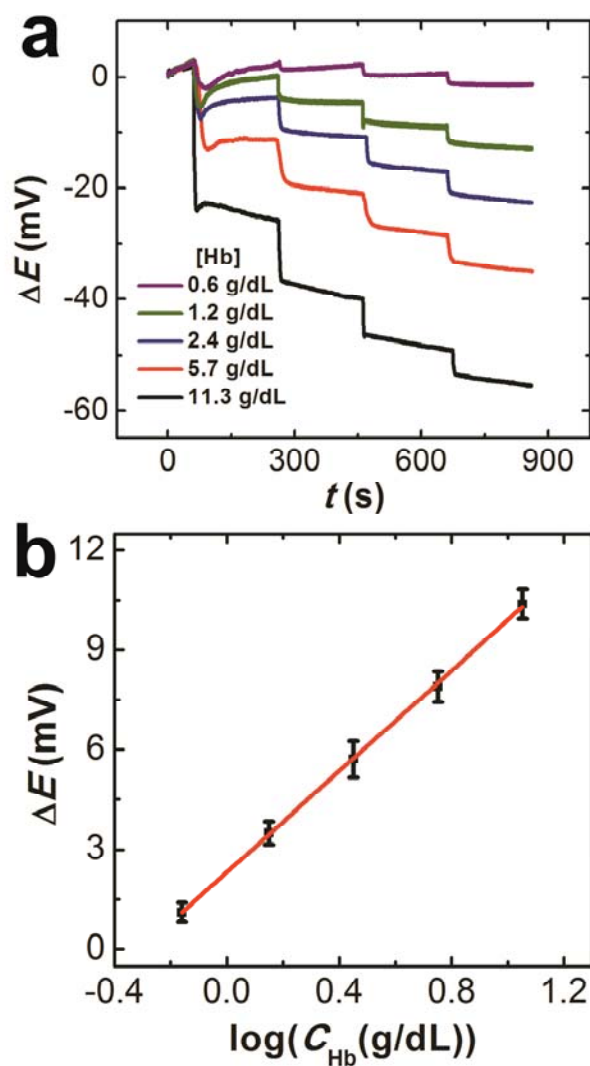


Figure 6.8. (a) Potential measured in 3.0 mL of 0.010 M PBS solution containing 10 mM $\text{Fe}(\text{CN})_6^{3-}$. 3.0 μL aliquots of Hb, present at the concentrations shown in the legend, were added every 200 s starting at $t = 60$ s. The potentials in the figure are normalized to their initial values. (b) Plot of the potential shifts at $t = 260$ s as a function of the logarithm of the Hb concentration in the sample.

Comparison of this potentiometric method to reference values for %HbA1c. Using the potentiometric methods described thus far, the HbA1c concentration, Hb concentration, and thus the %HbA1c in four blood samples were determined. The HbA1c concentrations were analyzed by measuring the potential shift, ΔE_2 (Figure 6.7a), and converting ΔE_2 to the HbA1c concentration by interpolating from the dose-response curve (Figure 6.7c) using eq 2.

$$C_{\text{HbA1c}} = C_{\text{HbA1c}}' + (C_{\text{HbA1c}}'' - C_{\text{HbA1c}}') \frac{\Delta E_2 - \Delta E_2'}{\Delta E_2'' - \Delta E_2'} \quad (2)$$

Here, $\Delta E_2'$ and $\Delta E_2''$ are two nearest potential shifts in Figure 6.7c, and C_{HbA1c}' and C_{HbA1c}'' are the corresponding HbA1c concentrations. The Hb concentrations were determined using the calibration curve shown in Figure 6.8b. The results obtained using the potentiometric and a reference method (Beckman CX, provided by the sample supplier) are provided in Table 6.1. The %HbA1c determined using the potentiometric method and the reference method are all within 0.5%.

Table 6.1. Assay results obtained using the reported potentiostatic method and a reference method (Beckman CX).

Sample	C_{HbA1c} (g/dL)	C_{Hb} (g/dL)	%HbA1c	Reference method
1	0.602	12.2	4.9%	5.0%
2	0.929	12.1	7.7%	8.0%
3	1.288	12.3	10.5%	10.8%
4	1.713	11.7	14.6%	14.8%

6.5 Summary and Conclusions

We have reported a potentiometric method for measuring the concentrations of HbA1c and Hb in human blood, and from these values the %HbA1c. The key to this method is that binding of ARS to PBA through diol-boronic acid complexation leads to a negative shift of the redox potential and competitive binding of HbA1c to PBA leads to the displacement of ARS and thus a positive shift of the redox potential. This positive shift in the solution potential is linked to the HbA1c concentration. The total hemoglobin concentration was determined by oxidizing Hb using $\text{Fe}(\text{CN})_6^{3-}$ and measuring the potential shift arising from the reduction of $\text{Fe}(\text{CN})_6^{3-}$. Four blood samples were tested using this method, and the results were in good agreement with that determined by a reference method. The method reported here is simple, low cost, and thus useful for point-of-care diagnosis and management of diabetes mellitus. To further improve the analytical performance of this method, we are searching for optimal indicator molecules (i.e., a replacement for ARS) as well as integrating the sensor onto a microfluidic platform. The results of these experiments will be reported in due course.

Chapter 7: Highly Reproducible Chronoamperometric Analysis in Microdroplets

7.1 Synopsis

This chapter describes a method for highly reproducible chronoamperometric analysis of the contents of microdroplets. Aqueous microdroplets having volumes on the order of 1 nL and separated by a fluorocarbon solvent are generated within a microfluidic device using a T-shaped junction. The key finding is that stable and reproducible quasi-steady-state currents are observed if the electrochemical measurements are made in a narrowed segment of a microchannel. Under these conditions, the microdroplets are stretched, here by a factor of 10, leading to desirable intradroplet mass transfer characteristics. Microdroplet frequencies up to 0.67 s^{-1} are accessible using this method. The quasi-steady-state currents resulting from chronoamperometric analysis of microdroplets containing $1.0\text{ mM Ru(NH}_3)_6^{3+}$ have relative standard deviations of just 1.8% and 2.8% at flow rates of 30 nL/min and 60 nL/min, respectively. Importantly, the design of the microelectrochemical device ensures direct contact between intradroplet redox molecules and the electrode surface. That is, the fluorocarbon between microdroplets does interfere with inner-sphere

electrocatalytic processes such as the oxygen reduction reaction. Finite-element simulations are presented that are in accord with the experimental findings.

7.2 Introduction

In this chapter we report an electrochemical method for detection of analytes in segmented microdroplets present within microfluidic channels. The significant new finding is that by stretching the microdroplet 10-fold in a narrow section of the microchannel, highly reproducible quasi-steady-state chronoamperometric currents are obtained. The magnitude of the experimentally determined current is confirmed by numerical simulation. Finally, inner-sphere electrochemical reactions, for example, the oxygen reduction reaction (ORR), are observed in the chronoamperometric analysis, which proves that there is intimate contact between redox molecules and the electrode surface.

Segmented flow for applications to microfluidics was originally reported by Quake and coworkers.⁴⁵ Since that time, it has been used to solve a number of problems associated with analytical applications of microfluidic systems. For example, due to laminar flow the rate of mixing in standard fluidic microchannels is limited by diffusional mass transport.^{46,47,48} However, mixing can be

accelerated by internal recirculating convection in a flowing microdroplet.¹¹¹ Moreover, pressure-driven flow in a microchannel is parabolic, which leads to axial Taylor dispersion and thus dilution of reagents.⁵⁰ In contrast, the immiscible organic phase between aqueous droplets encapsulates reagents, thereby avoiding dilution. Furthermore, nonspecific adsorption of reagents onto the walls of traditional microfluidic channels can be problematic,⁵¹ but this problem is avoided with segmented flow since the aqueous microdroplet does not contact the channel wall. Finally, poly(dimethylsiloxane) (PDMS), which is a common material used for fabricating microfluidic devices, is gas permeable and thus may lead to solvent evaporation problems.⁴⁷ This problem can also be solved by the encapsulation of microdroplet using an immiscible liquid. A number of methods have been reported for analyzing the contents of microdroplets: fluorescence spectroscopy,^{49,52,53} Raman spectroscopy,^{54,55} mass spectrometry,^{56,57} and electrochemical methods.⁵⁸⁻⁶⁰ Compared with other methods, electrochemistry is relative simple and low cost, and it provide information about mass transfer, electron transfer, and coupled chemical processes that are difficult or impossible to study using the aforementioned approaches.⁶¹ For example, Han et al.⁵⁸ reported on the enzymatic kinetics

of catalase confined within microdroplets by detecting H_2O_2 using wire electrodes inserted into the microchannel. In this case, the contact time between the electrodes and the droplets was short, and so the faradaic current was short and convoluted with a large capacitive current. Moreover, the electrode wires were forced to penetrate each droplet, and this resulted in a significant degree of droplet instability. The same group also reported a potentiometric method, using an ion-selective electrode, for studying rapid binding kinetics of Mg^{2+} to RNA in microdroplets.⁶² However, the potentiometric measurement was not carried out in droplets, but rather under continuous flow conditions. Electrochemical measurements in larger (millimeter-scale) droplets have also been reported. For example, Liu et al.⁵⁹ used chronoamperometry to study droplet size, frequency of droplet generation, and flow velocity of droplets in organic fluid containing redox species. Sassa et al.⁶⁰ used electrode arrays to enhance the sensitivity of coulometric detection of H_2O_2 and L-glutamate in aqueous droplets. However, it would be challenging to do these experiments when the size of the droplets decreased to micrometer scale. In this paper, we describe a method for highly reproducible ($\pm 2\%$) amperometric analysis in microdroplets having volumes on the order of 1 nL. In our method, microdroplets are

generated in a rectangular T-shaped microchannel (T-junction). Each microdroplet then flows into a narrower section of the microchannel where three microband electrodes are located (Figure 7.1a). Due to the reduction in volume imposed by the narrow channel, the microdroplet is stretched longitudinally. The electrochemical analysis is carried out by holding the potential of the working electrode at a value that ensures mass-transfer-limited current. Because the length of the stretched microdroplet is much larger than the width and height of the microdroplet, mass transfer within each droplet has a mass-transfer profile that is similar to that in a continuous pressure-driven flow. This facilitates reproducible current measurement and simplifies the model for numerical simulation. Accordingly, we present a three-dimensional (3-D) numerical simulation that correlates well to the observed experimental results.

7.3 Experimental

Chemicals. The silicone elastomer and curing agent (Sylgard 184) used to prepare the PDMS microfluidic devices were obtained from Dow Corning, (Midland, MI). A fluorocarbon solution (PFDO) containing a 10:1 (v/v) mixture of perfluorodecalin (mixture of cis and trans, 95%, Acros Organics) and 1H,1H,2H,2H-perfluoro-1-octanol (97%, Sigma-Aldrich) was used as the fluorocarbon carrier solution. Hexamine ruthenium (III) chloride ($\text{Ru}(\text{NH}_3)_6^{3+}$, >99.9%) and ferrocenemethanol (FcMeOH, 97%) were purchased from Sigma-Aldrich. KNO_3 (Fisher Scientific) was used as the supporting electrolyte. All aqueous solutions were prepared with deionized water (18.0 M Ω ·cm, Milli-Q Gradient System, Millipore). All reagents were used as received without further purification.

Microelectrochemical devices. The hybrid PDMS/glass microelectrochemical devices were fabricated using a previously published procedure.^{112,113} Briefly, the T-junction (Figure 7.1a) was fabricated from PDMS using the replica micromolding method.¹¹² The main microchannel was 100 μm wide and 21 μm high. A smaller channel segment (10 μm wide and 21 μm high), which was used to stretch the microdroplets, was inserted in the middle of the main

channel (Figure 7.1a). Reservoirs (1.0 mm in diameter) were punched at each end of the microchannel to accommodate the ingress and egress of fluids. Three Au microband electrodes were microfabricated from Au-coated glass slide (100 nm Au atop a 5 nm Cr adhesion layer, Evaporated Metal Films, Ithaca, NY) using standard photolithography.¹¹³ The electrodes were 25 μm wide with an edge-to-edge spacing of 10 μm . Finally, the PDMS and the glass side were exposed to an O_2 plasma (60 W, model PDC-32F, Harrick Scientific, Ossining, NY) for 15 s and then bonded together permanently with the Au electrodes oriented perpendicular to the narrow section of the microchannel. Two gas-tight, glass syringes (Hamilton Company, Reno, NV), having maximum volumes of 25 μL and 50 μL , were driven by a syringe pump (Pump 11 pico plus elite, Harvard Apparatus, Holliston, MA) and used for injecting fluorocarbon and aqueous solutions, respectively, into the microchannel. The syringes were connected to the reservoirs using Teflon tubing.

Silanization of microchannel. After assembly, the microchannel was silanized.¹¹⁴ Briefly, the vapor of 1H,1H,2H,2H-perfluorooctyl-trichlorosilane (Sigma-Aldrich) was entrained within a N_2 gas stream and then introduced into the microchannel at a flow rate of 5.0 $\mu\text{L}/\text{min}$ for 60 min. Next, the device was heated to 80 $^\circ\text{C}$ for 30 min, and

then it was rinsed sequentially with acetone and water. A separate experiment was undertaken to study the surface properties of the glass, PDMS, and Au electrodes before and after silanization. In this case, the silanization procedure was carried out prior to assembly of the microfluidic device. For these experiments, 10 μL of the PFDO solution or deionized water was dropcast onto each of the three surfaces, and a micrograph of the droplet was immediately imaged using a contact-angle goniometer (Model 100-00-115, Rame Hart, Netcong, NJ).

Electrodeposition of Ag. A Ag quasi-reference (QRE) was prepared within the microchannel by electrodepositing Ag onto the central Au microband (Figure 7.1a).¹¹⁵ Briefly, a Ag wire (0.25 mm in diameter, 99.9%, Sigma-Aldrich) was inserted into the downstream reservoir to act as a QRE and counter electrode for the electrodeposition. An aqueous solution containing 0.050 M AgNO_3 (Sigma-Aldrich), 1.0 M NaNO_3 (Fisher Scientific), and 0.50 M NH_4OH (Sigma-Aldrich) was introduced into the microchannel at a flow rate of 0.60 $\mu\text{L}/\text{min}$. Next, the central Au microband was cleaned electrochemically by holding its potential at 0.950 V vs. Ag QRE for 30 s. Finally, Ag was electrodeposited by holding the electrode potential at -0.200 V vs. Ag QRE for 15 s, and

then the microchannel was rinsed using 0.50 M NH_4OH aqueous solution followed by water.

Optical imaging and electrochemistry. An inverted microscope (Eclipse TE 2000-U, Nikon, Tokyo, Japan) configured with a CCD camera (Cascade, Photometrics Ltd., Tucson, AZ) was used to image the microdroplets and the three microband electrodes in the narrow section of the microchannel. Micrographs of Au microband electrodes with and without an electrodeposited Ag layer were obtained using an optical microscope (Nikon AZ 100, Nikon, Tokyo, Japan) equipped with a CCD camera (Cascade, Photometrics Ltd., Tucson, AZ). The optical micrographs were processed using V++ Precision Digital Imaging software (Digital Optics, Auckland, New Zealand). A potentiostat (Model 650c, CH Instruments, Austin, TX) was used for all electrochemical experiments. Quasi-steady-state currents of redox species in microdroplets were measured at the end of current transients.

Numerical simulation. 3-D numerical simulation of the electrochemical experiment was carried out using the COMSOL multiphysics software package (Burlington, MA). The fluidic dynamics and the mass transfer problems were solved using the incompressible Navier-Stokes and convection-diffusion equations, respectively. A portion of the narrow microchannel having the electrode boundary was chosen as the

subdomain. A free mesh method using triangular elements was used for meshing the subdomain. The mesh was optimized by gradually reducing the size of mesh unit near the electrode boundary until a convergent solution of current was obtained. The steady-state current was calculated based on the integral of the normal concentration gradient of redox species at the electrode boundary.

7.4 Results and Discussion

Silanization of microchannel. Reproducible generation of size-monodisperse microdroplets flowing at a relatively low rate is crucial for quantitative electrochemical measurements. To generate microdroplets in the microchannel, the surface of the microchannel must be rendered hydrophobic or else two immiscible fluids may flow parallel to each other without forming microdroplets.¹¹⁶ Here, we used a PDMS-glass hybrid microfluidic chip, and the surface of the microchannel was modified by silanization using 1H,1H,2H,2H-perfluorooctyl-trichlorosilane. The effects of silanization on the surface properties of glass, PDMS, and Au slides were studied using contact-angle measurements. The results (Figure 7.2) show that the water contact angles for the glass and PDMS surfaces increase after the silanization, while the PFDO contact angles decrease. These measurements

demonstrate that the PDMS and glass surfaces were rendered hydrophobic and fluorophilic by the silanization procedure. Consequently, these modified surfaces were preferentially wetted by the PFDO phase, which is required for generating microdroplets. In contrast there was no significant change of the contact angles before and after silanization for the Au electrodes. This is important, because silanization would likely make the Au surface less wettable by microdroplets, and thus have an adverse effect on subsequent electrochemical measurements (especially for inner-sphere redox reactions).

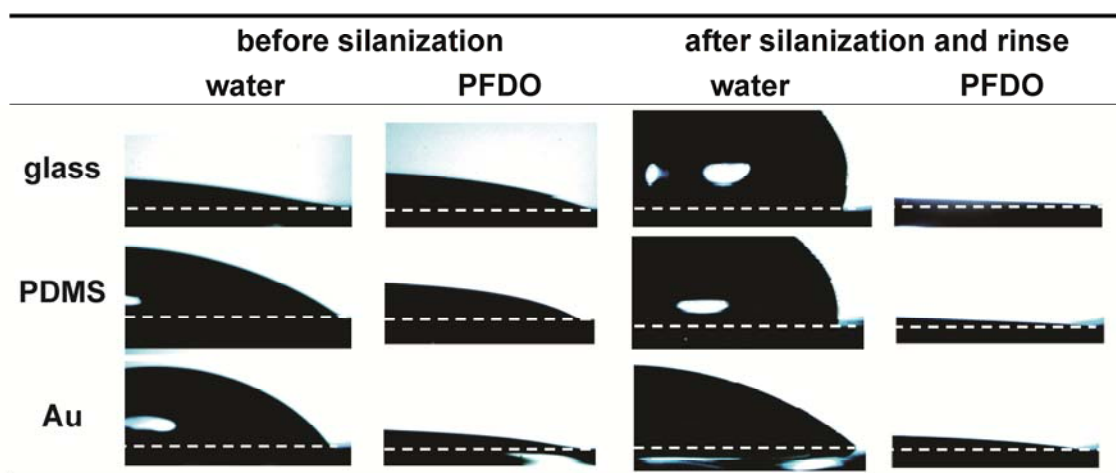


Figure 7.2. Optical micrographs obtained after 10 μL of deionized water or PFDO were dropcast onto glass, PDMS, and Au surfaces, respectively. The micrographs were obtained (left side) before and (right side) after silanization and rinsing with PFDO. The liquid-solid interface is highlighted by dashed white lines.

Generation of microdroplets. As shown in Figures 7.1 and 7.3, a T-junction was fabricated and silanized to generate microdroplets. This part of the microchannel is 100 μm wide and 21 μm high. The PFDO solution containing a 10:1 (v/v) mixture of perfluorodecalin and 1H,1H,2H,2H-perfluoro-1-octanol was injected into the main channel at 10 nL/min, and an aqueous solution containing 1.0 mM $\text{Ru}(\text{NH}_3)_6^{3+}$ and 0.10 M KNO_3 was injected into the side channel at 20 nL/min. The microdroplets spontaneously formed at the intersection of these two channels.

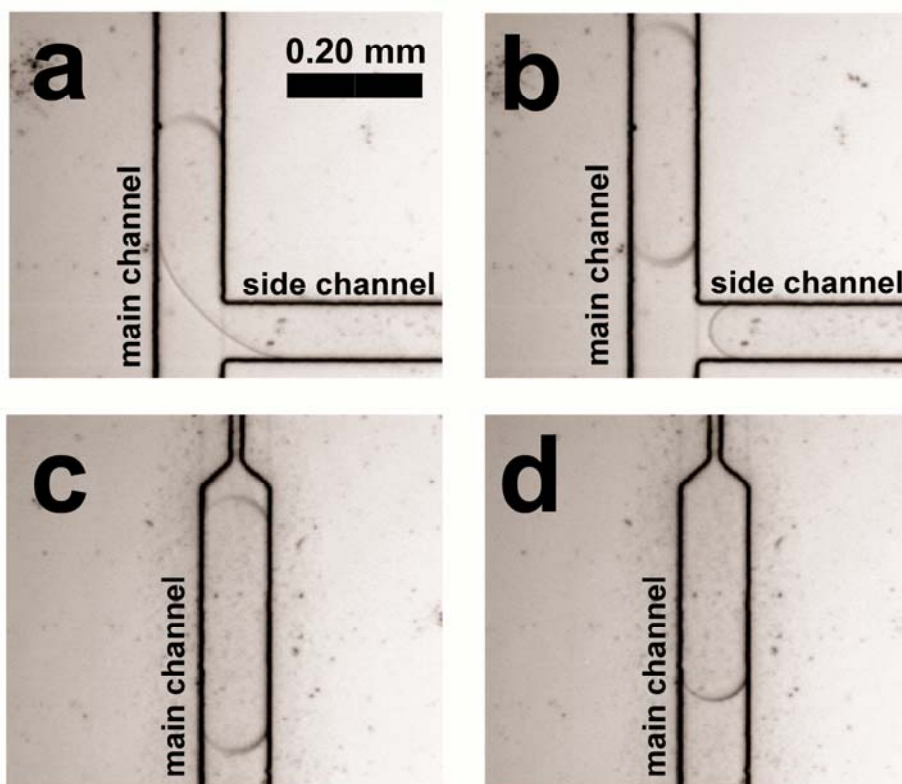


Figure 7.3. Optical micrographs showing the evolution of an individual microdroplet. (a) Water containing 1.0 mM $\text{Ru}(\text{NH}_3)_6^{3+}$ and 0.10 M KNO_3 is injected from a side channel into the main channel containing PFDO. Both channels are 100 μm wide and the flow rates were 20 and 10 nL/min, respectively. (b) Generation of an aqueous microdroplet (0.84 nL) under the conditions described in (a). (c) The microdroplet moving toward the narrowed (10 μm wide) section of the microchannel at a flow rate of 30 nL/min. (d) The microdroplet entering the narrow segment of the channel at 30 nL/min. All the microchannels are 21 μm high.

The formation of microdroplets in a microfluidic T-junction has been studied.^{111,117} Due to the small capillary number ($Ca < 0.01$) of fluid in a microfluidic channel, the microdroplets only form when the aqueous fluid blocks almost the entire main microchannel thereby causing a substantial upstream pressure increase. In this situation, the shape of the microdroplets is defined by the microchannel geometry, and the length of the microdroplets can be expressed by eq 1.¹¹⁷

$$L/w = 1 + aQ_{in}/Q_{out} \quad (1)$$

Here, L is the axial length of the microdroplet, w is the width of the microchannel, a is a constant determined by the channel geometry, and Q_{in} and Q_{out} are the volume flow rates of the aqueous and fluorocarbon fluids, respectively. Eq. 1 indicates that the size of the microdroplets can be controlled by manipulating the ratio of volume flow rates of two immiscible fluids (i.e., Q_{in}/Q_{out}). For all ensuing experiments, $Q_{in}/Q_{out} = 2$, so that microdroplets of the same size could be generated at different total volume flow rates (thereby varying their linear velocity). On the basis of optical micrographs (Figures 7.3b and 7.3c) and the height

of the microchannel, the volume of the microdroplets was determined to be 0.84 nL.

Stretching of microdroplets. The microdroplets generated in the T-junction were directed into a narrow downstream microchannel (10 μm wide and 21 μm high, Figures 7.1 and 7.4) for chronoamperometric measurement of redox molecules entrained within the aqueous phase. Because the cross-sectional area of the narrow segment of the main microchannel is ten times smaller than that of the wide segment, and because the fluids are incompressible, the microdroplets were stretched ten-fold along the axial direction. The presence of 1H,1H,2H,2H-perfluoro-1-octanol in the PFDO phase, which is a surfactant, reduces the surface tension at the water-PFDO interface.¹¹¹ Therefore, no breaking of microdroplets was observed during the stretching process. The time required for a microdroplet to completely enter the narrow channel was ~ 0.75 s and that the time separation between two microdroplets was ~ 3.1 s.

Fabrication of the QRE and electrochemical characterization. To enable chronoamperometric analysis of the stretched microdroplets, Au microband electrodes (each 25 μm wide) were microfabricated on the glass slide and oriented perpendicular to the narrow microchannel. As shown in Figure 7.1, the upstream Au electrode was the working

electrode, the one in the middle was the QRE, and the counter electrode was downstream. As discussed in the Experimental Section, the QRE was prepared by electrodepositing Ag onto the surface of the central Au microband. As shown in Figure 7.4a, Ag electrodeposition changed the optical contrast of the underlying Au microband, which confirmed the presence of the Ag layer. On the basis of the charge passed during electrodeposition (1.57 C) and the exposed area of the microband ($250\text{ }\mu\text{m}^2$), the thickness of the electrodeposited Ag layer was $\sim 770\text{ nm}$.¹¹⁵ Because the channel height is $21\text{ }\mu\text{m}$ and the working electrode is $10\text{ }\mu\text{m}$ upstream of the QRE, the presence of the Ag layer should not affect electrochemical measurements.

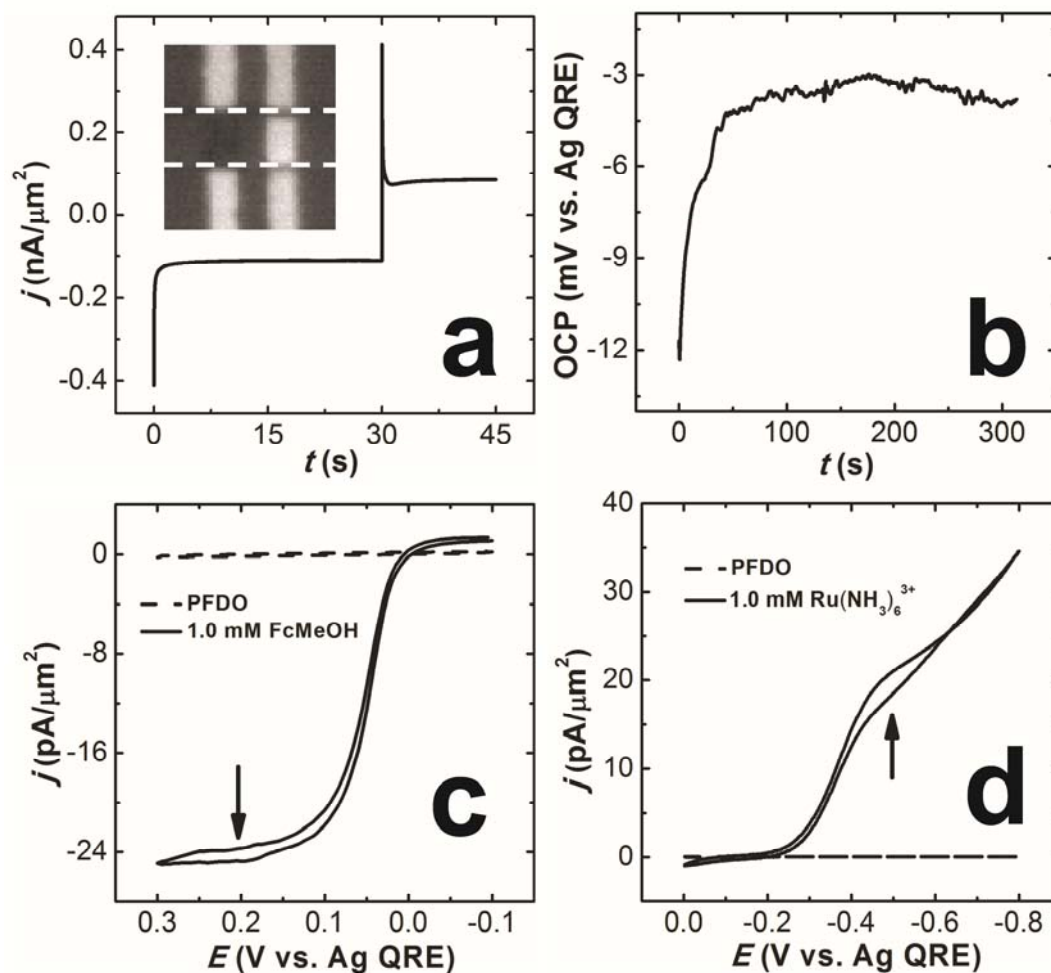


Figure 7.4. (a) Current as a function of time during the electrodeposition of Ag onto the center Au microband electrode (Figure 7.1). The aqueous solution contained 0.050 M AgNO_3 , 1.0 M NaNO_3 , and 0.50 M NH_4OH , and the flow rate was 0.60 $\mu\text{L}/\text{min}$. The potential of the electrode was held for 30 s at 0.95 V vs. a Ag wire QRE inserted in a downstream reservoir, and then it was stepped to -0.20 V for 15 s. Inset: optical micrograph of the Au microbands showing

Ag electrodeposited on the leftmost electrode. The location of the microchannel is highlighted by the dashed white lines. (b) The OCP of the Ag-coated microband electrode as a function of time. The potential was measured using a Ag wire QRE inserted into the downstream reservoir immediately after electrodeposition of Ag. (c) Cyclic voltammograms obtained in an aqueous solution containing 1.0 mM FcMeOH and 0.10 M KNO₃ (solid line) or PFDO (dashed line). The flow rate was 300 nL/min, the potential was measured using the electrodeposited Ag QRE, and the scan rate was 10 mV/s. (d) Cyclic voltammograms obtained in an aqueous solution containing 1.0 mM Ru(NH₃)₆³⁺ and 0.10 M KNO₃ (solid line) or in PFDO (dash line). The flow rate was 300 nL/min, the potential was measured using the electrodeposited Ag QRE, and the scan rate was 50 mV/s. The potentials used to obtain the chronoamperometric measurements in Figures 7.5 and 7.6 are marked by arrows.

The open-circuit potential (OCP) of the electrodeposition solution measured using the electrodeposited Ag QRE was found to be sufficiently stable. This measurement was made by inserting a Ag wire QRE into the downstream reservoir, and recording the OCP as a function of time immediately after electrodeposition of Ag. As shown in Figure 7.4b, the potential drifted from -12 mV to -4 mV in > 5 min.

The three-electrode system illustrated in Figure 7.1 was tested by carrying out cyclic voltammetric analysis of 1.0 mM FcMeOH (Figure 7.4c) and 1.0 mM $\text{Ru}(\text{NH}_3)_6^{3+}$ (Figure 7.4d) using 0.10 M KNO_3 as the supporting electrolyte in a continuous, flowing (300 nL/min) aqueous stream. The onset of current arising from oxidation of 1.0 mM FcMeOH is at 0 V vs. Ag QRE, and the current reaches a steady-state, mass-transfer-limited current at ~0.200 V vs. Ag QRE. In Figure 7.4d, the onset current arising from the reduction of 1.0 mM $\text{Ru}(\text{NH}_3)_6^{3+}$ was observed at ~ -0.200 V vs. Ag QRE. In this case, no well-defined mass-transfer-limited current was observed due to the onset of the ORR. The ORR is difficult to avoid in PDMS microchannels due to its high O_2 permeability.¹¹⁸ When the aqueous solution was replaced with

PFDO under the same conditions used for Figures 7.4c and 7.4d, no current was observed.

Chronoamperometry in microdroplets. Chronoamperometric analysis of $\text{Ru}(\text{NH}_3)_6^{3+}$ in microdroplets was carried out by holding the working electrode at the potential marked in Figure 7.4d and measuring the resulting current. Figure 7.5 shows the chronoamperometric response obtained from a series of microdroplets containing 1.0 mM $\text{Ru}(\text{NH}_3)_6^{3+}$ and 0.10 M KNO_3 at total flow rates of 30 and 60 nL/min. First consider the data obtained at the flow rate of 30 nL/min (Figures 7.5a and 7.5b). A series of current transients, each lasting ~ 0.30 s, is observed during the time that the aqueous microdroplets are present within the narrow microchannel segment. The duration of these current excursions is smaller than the overall residence time (~ 0.75 s) of the microdroplets within the narrow segment of the channel. However, the time between current pulses, ~ 3.0 s, is in good agreement with the temporal separation of the microdroplets (~ 3.0 s and 3.1 s, respectively). Figure 7.5b shows that the initial current is high for each droplet, then it decreases with time, and finally it approaches a quasi-steady-state value of 33.7 ± 0.6 pA/ m^2 (relative standard deviation = 1.8%).

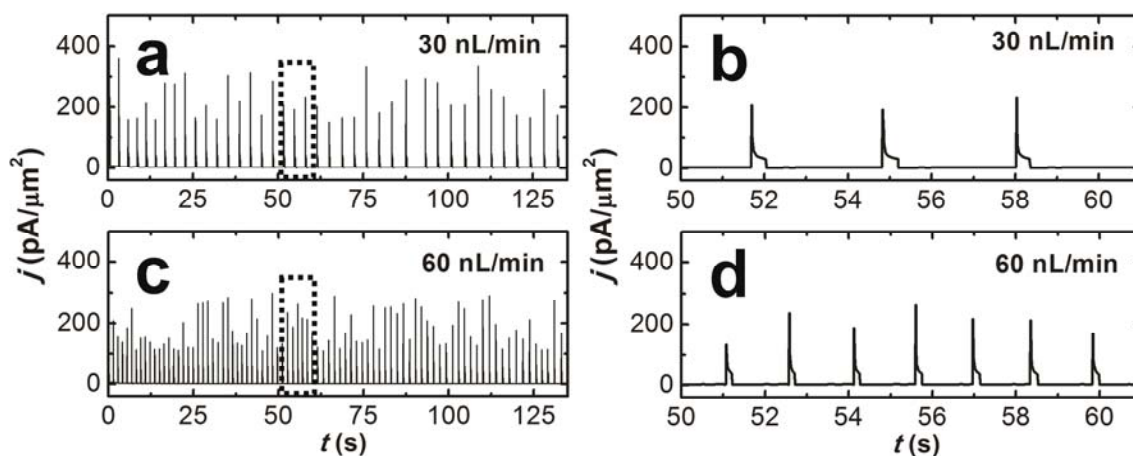


Figure 7.5. Chronoamperometric currents obtained from a series of aqueous microdroplets using the microelectrochemical device shown in Figure 7.1. The microdroplets contained 1.0 mM $\text{Ru}(\text{NH}_3)_6^{3+}$ and 0.10 M KNO_3 (a) Flow rate = 30 nL/min. (b) Expanded section (dashed black lines) of the data in (a). (c) Flow rate = 60 nL/min. (d) Expanded section (dashed black lines) of the data in (c).

Next, consider the data obtained at a flow rate of 60 nL/min (Figures 7.5c and 7.5d). As for the higher flow rate, Figures 7.5d shows that the initial current is high for each droplet, but that it decreases with time and finally approaches a quasi-steady-state value of 43.2 ± 1.2 nA (relative standard deviation = 2.8%). Comparing the two sets of data, the ratio of the quasi-steady-state currents at 30 and 60 nL/min is 0.78, which equals the cubed root of the ratio of flow rates $(30/60)^{1/3} = 0.79$ and is therefore in accord with that anticipated by the Levich equation for steady-state transport under flow.¹¹⁹ It is also noteworthy that when the flow rate is 60 nL/min (Figure 7.5c and 7.5d), the time separation between current transients is ~ 1.5 s (frequency = 0.67 s^{-1}), and the duration of each current response is ~ 0.15 s. At a flow rate of 30 nL/min these times are 3.0 s and 0.31 s, respectively, or about double their value at 60 nL/min.

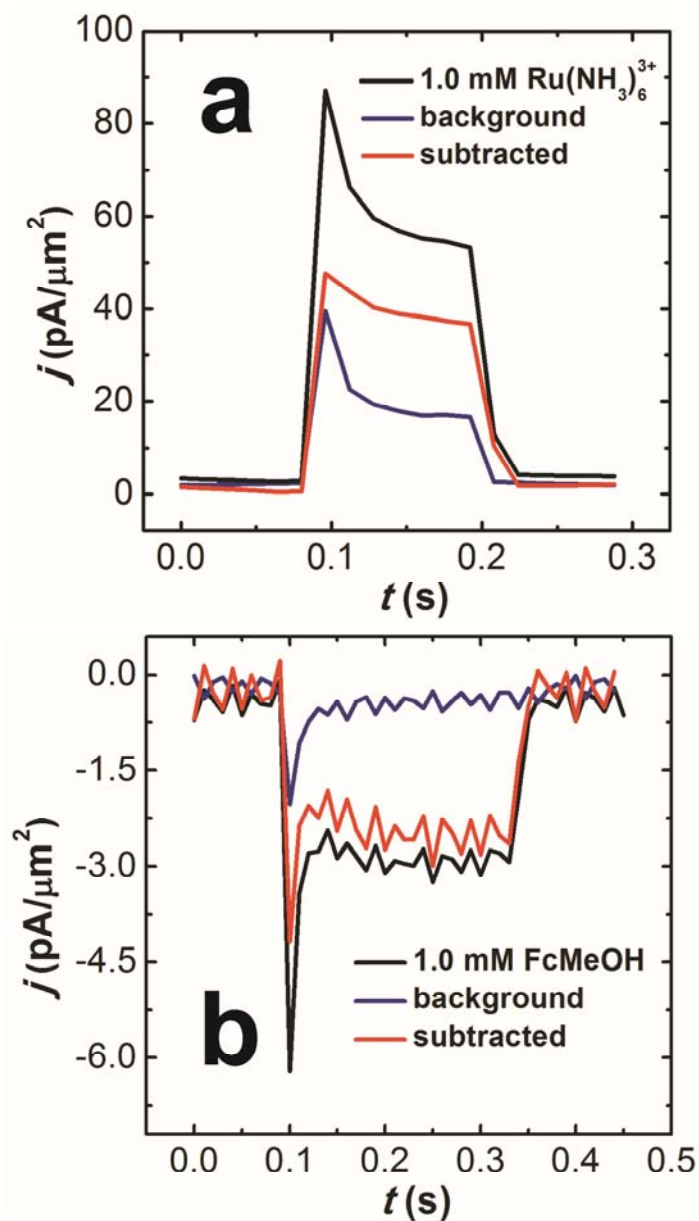


Figure 7.6. Current transients obtained from individual microdroplets. (a) The droplet contained $1.0 \text{ mM Ru(NH}_3)_6^{3+}$ and 0.10 M KNO_3 (black line) or 0.1 M KNO_3 only (blue line). The flow rate was 60 nL/min . The red line is the background-

subtracted current arising from reduction of $\text{Ru}(\text{NH}_3)_6^{3+}$. (b) The droplet contained 1.0 mM FcMeOH and 0.10 M KNO_3 (black line) or 0.1 M KNO_3 only (blue line). The flow rate was 30 nL/min. The red line is the background-subtracted current arising from oxidation of FcMeOH. The working electrodes were held at the potentials marked by the arrows in Figures 7.4d and 7.4c, respectively.

A chronoamperometric analysis was conducted in a microdroplet containing only 0.10 M KNO₃ (no Ru(NH₃)₆³⁺) to better understand the shape of the current transients shown in Figure 7.5. The blue curve in Figure 7.6a shows the result of this experiment. Compared to the case with Ru(NH₃)₆³⁺ present (black curve), the current is obviously lower, and the difference in the current densities for these two experiments (37 pA/μm², red) should represent the faradaic current arising from the reduction of Ru(NH₃)₆³⁺. The rather high background current originates mainly from the ORR (Figure 7.4d), which also occurs at the potential (-0.500 V vs. Ag QRE) used to obtain these data. The observation that the ORR is operative in the microdroplet is an important finding, because it means there is intimate contact between redox molecules and the electrode surface (the ORR is an inner-sphere process on Au electrodes).¹²⁰ Given the presence of the fluorocarbon that separates the aqueous droplets, and its potential for coating the Au electrode with a thin film, this was not obvious *a priori*. We speculate that water, rather than the fluorocarbon, wets the electrode for two reasons. First, Figure 7.2 shows that the Au electrode is not modified by the hydrophobic fluorinated silane that is used to control the surface

properties of the glass and the PDMS. Second, chronoamperometric analysis of $\text{Ru}(\text{NH}_3)_6^{3+}$ is carried out at a potential (-0.500 V vs. Ag QRE) negative of the point-of-zero charge for Au.¹²¹ This results in a charged surface which is preferentially wetted by aqueous solution.¹²²

We also carried out a chronoamperometric analysis of microdroplets containing 1.0 mM FcMeOH and 0.10 M KNO_3 (black curve in Figure 7.6b). Similar to the $\text{Ru}(\text{NH}_3)_6^{3+}$ experiments, the initial current is high for each droplet, then it decreases with time, and finally it approaches a quasi-steady-state value of $\sim -2.80 \text{ pA}/\mu\text{m}^2$. A control experiment was carried out in microdroplets containing only 0.10 M KNO_3 (blue curve in Figure 7.6b). Because the working electrode was held at a positive potential (0.200 V vs. Ag QRE) where the ORR is not operative (Figure 7.4c), the current obtained was just capacitive. This background current decayed to zero in $\sim 0.10 \text{ s}$. By subtraction, the current density for the oxidation of 1.0 mM FcMeOH was determined to be $-2.65 \text{ pA}/\mu\text{m}^2$ (red curve in Figure 7.6b). The current was more than one order of magnitude smaller than the current obtained in 1.0 mM $\text{Ru}(\text{NH}_3)_6^{3+}$ solution ($36.7 \text{ pA}/\mu\text{m}^2$), presumably because of the high solubility of FcMeOH in fluorocarbon phase,¹²³ in other words, it leaks from the aqueous microdroplets into the PFDO phase.

Numerical simulation. Internal convection within a flowing microdroplet has been simulated previously.¹²⁴ The results indicated that unless at two extremities of the microdroplet, the mass transfer in the flowing microdroplet is similar to a continuous pressure-driven flow. In our case, the microdroplet has been stretched by a factor of 10, and therefore its length is much larger than its width and height. Consequently, the stretched microdroplet approximates a continuous fluidic stream (i.e., not segmented) having only parabolic axial convection. For simplicity, the effect of the fluorocarbon phase on convection was not considered in the treatment discussed below.¹²⁴

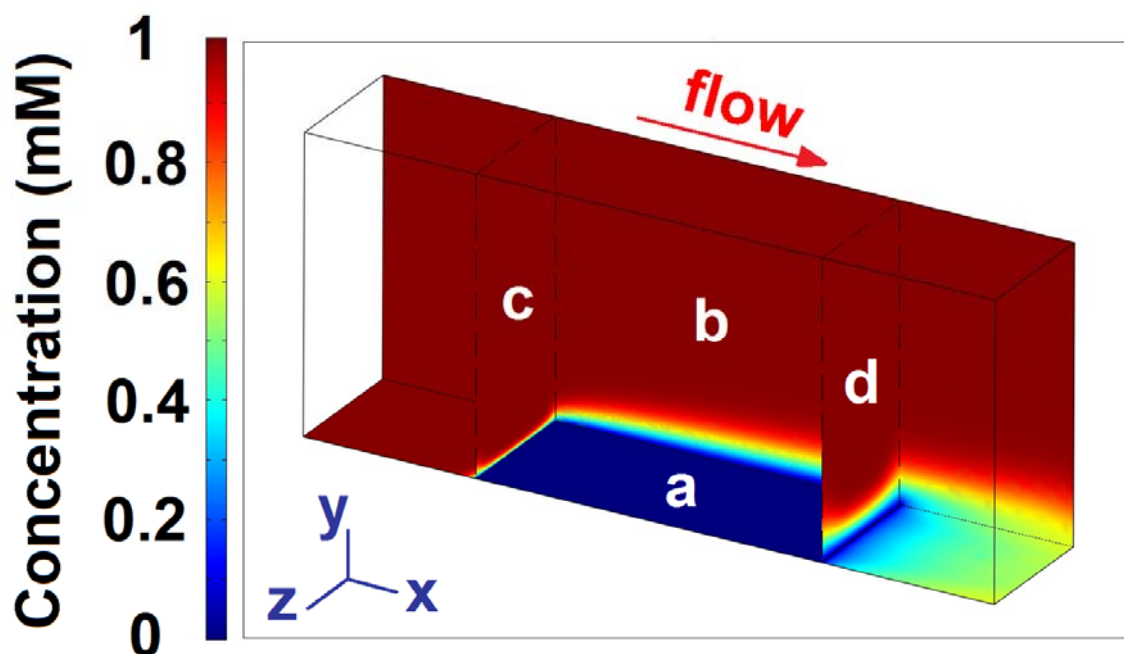


Figure 7.7. Slice plot of the simulated steady-state concentration profile of 1.0 mM $\text{Ru}(\text{NH}_3)_6^{3+}$ (a) at the bottom of the channel where the microelectrode is located, (b) on the channel wall, (c) on the plane normal to the front edge of the microelectrode, and (d) on the plane normal to the rear edge of the microelectrode. The channel was 21 μm high and 10 μm wide with a 25 μm wide embedded microelectrode. $\text{Ru}(\text{NH}_3)_6^{3+}$ is reduced at the microelectrode boundary under mass transfer-limited condition.

A 3-D model was constructed for the simulation of the experiments represented in Figure 7.6a (red curve). The slice plot of the simulated steady-state concentration profile of $\text{Ru}(\text{NH}_3)_6^{3+}$ in the selected subdomain is shown in Figure 7.7. Because the working electrode is held at potential where the reduction of $\text{Ru}(\text{NH}_3)_6^{3+}$ is limited by mass transfer (Figure 7.4d), the concentration of $\text{Ru}(\text{NH}_3)_6^{3+}$ at the electrode goes to zero. Consequently, $\text{Ru}(\text{NH}_3)_6^{3+}$ in the bulk solution diffuses toward the electrode forming a diffusion layer, as shown by the color gradient in Figure 7.7. Due to the parabolic flow velocity in the microchannel, the concentration profile has a parabolic shape along the z axis. The steady-state current density, which was calculated based on the concentration gradient normal to the electrode surface, is 36 pA/ m^2 . This value is in good agreement with the experimentally determined, background-subtracted quasi-steady-state current of 37 pA/ m^2 (Figure 7.6a).

7.5 Summary and Conclusions

We have reported a method for highly reproducible chronoamperometric analysis of the contents of microdroplets generated within a microelectrochemical device. The key finding is that stable and reproducible quasi-steady-state

currents are observed for microdroplets having volumes of ~1 nL if electrochemical measurements are made within a narrowed segment of the microchannel. Under these conditions, the microdroplets are stretched, and this leads to desirable intradroplet mass transfer characteristics.

Importantly, the design of the microelectrochemical device ensures direct contact between intradroplet redox molecules and the electrode surface. That is, the fluorocarbon separating microdroplets does not interfere with inner-sphere electrocatalytic processes such as the oxygen reduction reaction. This means the device is appropriate for studying electrocatalytic reactions in small volumes and under well-defined conditions of mass transfer. Moreover, because the droplets are so small, the concentration of even small numbers of redox molecules within each droplet is sufficient for electrochemical detection. Hence, this approach also has applications to electroanalytical chemistry. Results demonstrating these principles will be reported in due course.

Chapter 8: Summary and Conclusion

In this dissertation, three types of paper-based analytical devices for point-of-care biosensing, a potentiometric method for analyzing percent hemoglobin A1c (%HbA1c) and a PDMS-glass microelectrochemical device for highly reproducible amperometric measurement in microdroplet, are described.

The Chapter 3 describes the first paper-based sensing device which is fabricated using the principles of origami (paper folding). The three-dimensional (3-D) origami paper analytical device (oPAD) is fabricated on a single sheet of flat paper in a single photolithographic step and assembled by simply folding the paper by hand. Following analysis, the device can be unfolded to reveal each layer for optical assays.

The Chapter 4 describes the second type of paper-based device which has an integral aluminum/air battery as the power source and reports its output using Prussian blue as an electrochromic indicator. The integrated aluminum/air battery powers both the electrochemical sensor and the electrochromic read-out. The applicability of the device to point-of-care sensing is demonstrated by qualitative detection of glucose and H_2O_2 in artificial urine.

The Chapter 5 describes the third type of paper-based device (oPAD 2) which uses an aptamer to recognize the analyte, adenosine, a glucose oxidase tag to modify the relative concentrations of an electroactive redox couple, and a digital multimeter to transduce the result of the assay. Adenosine is quantitatively determined using this device with a detection limit of 11.8 μM .

The Chapter 6 describes a simple and low-cost potentiometric method for measuring HbA1c concentration, hemoglobin (Hb) concentration, and thus %HbA1c in human blood is developed for diagnosis and management of diabetes. We use alizarin red s (ARS) as a redox indicator. The potential shift of ARS owing to diol-boronic acid complexation is used to determine the HbA1c, which is a competitor of ARS for the complexation reaction. The concentration of Hb is determined by reacting it with $\text{Fe}(\text{CN})_6^{3-}$ and measuring the potential shift arising from the reduction of $\text{Fe}(\text{CN})_6^{3-}$ by Hb. The results obtained for %HbA1c in human blood are in good agreement with those determined using a reference method.

The Chapter 7 describes a method for highly reproducible chronoamperometric analysis of the contents of microdroplets is developed. Aqueous microdroplets ($\sim 1 \text{ nL}$) and separated by a fluorocarbon solvent are generated within

a microfluidic device using a T-shaped junction. Highly reproducible quasi-steady-state currents are observed when the microdroplets are stretched by a factor of 10 in a narrowed segment of a microchannel (relative standard deviations = $\sim 2\%$). The stretching leads to desirable intradroplet mass transfer characteristics. Importantly, the design of the microelectrochemical device ensures direct contact between intradroplet redox molecules and the electrode surface to study inner-sphere electrocatalytic processes such as the oxygen reduction reaction. Finite-element simulations are presented that are in accord with the experimental findings.

References

1. Biermann, C. J. *Handbook of Pulping and Papermaking*. Academic Press: San Diego, 1993.
2. Klemm, D.; Heublein, B.; Fink, H. P.; Bohn, A. Cellulose: Fascinating biopolymer and sustainable raw material. *Angew. Chem. Int. Ed.* **2005**, *44*, 3358-3393.
3. Partington, J. R. J. L. Gay-Lussac (1778-1850). *Nature* **1950**, *165*, 708-709
4. Martinez, A. W.; Phillips, S. T.; Butte, M. J.; Whitesides, G. M. Patterned paper as a platform for inexpensive, low-volume, portable bioassays. *Angew. Chem. Int. Ed.* **2007**, *46*, 1318-1320.
5. Gubala, V.; Harris, L. F.; Ricco, A. J.; Tan, M. X.; Williams, D. E. Point of Care Diagnostics: Status and Future. *Anal. Chem.* **2012**, *84*, 487-515.
6. Muller, R. H.; Clegg, D. L. Automatic Paper Chromatography. *Anal. Chem.* **1949**, *21*, 1123-1125.
7. Bruzewicz, D. A.; M., R.; Whitesides, G. M. Low-Cost Printing of Poly(dimethylsiloxane) Barriers To Define Microchannels in Paper. *Anal. Chem.* **2008**, *80*, 3387-3392.

8. Abe, K.; Suzuki, K.; Citterio, D. Inkjet-Printed Microfluidic Multianalyte Chemical Sensing Paper. *Anal. Chem.* **2008**, *80*, 6928-6934.
9. Li, X.; Tian, J. F.; Nguyen, T.; Shen, W. Paper-Based Microfluidic Devices by Plasma Treatment. *Anal. Chem.* **2008**, *80*, 9131-9134.
10. Lu, Y.; Shi, W. W.; Qin, J. H.; Lin, B. C. Fabrication and Characterization of Paper-Based Microfluidics Prepared in Nitrocellulose Membrane By Wax Printing. *Anal. Chem.* **2010**, *82*, 329-335.
11. Carrilho, E.; Martinez, A. W.; Whitesides, G. M. Understanding Wax Printing: A Simple Micropatterning Process for Paper-Based Microfluidics. *Anal. Chem.* **2009**, *81*, 7091-7095.
12. Delaney, J. L.; Hogan, C. F.; Tian, J. F.; Shen, W. Electrogenerated Chemiluminescence Detection in Paper-Based Microfluidic Sensors. *Anal. Chem.* **2011**, *83*, 1300-1306.
13. Olkkonen, J.; Lehtinen, K.; Erho, T. Flexographically Printed Fluidic Structures in Paper. *Anal. Chem.* **2010**, *82*, 10246-10250.
14. Dungchai, W.; Chailapakul, O.; Henry, C. S. A low-cost, simple, and rapid fabrication method for paper-based

- _____. *Analyst* **2011**, *136*, 77-82.
15. Chitnis, G.; Ding, Z. W.; Chang, C. L.; Savran, C. A.; Ziaie, B. Laser-treated hydrophobic paper: an inexpensive microfluidic platform. *Lab Chip* **2011**, *11*, 1161-1165.
16. Martinez, A. W.; Phillips, S. T.; Whitesides, G. M. Three-dimensional microfluidic devices fabricated in layered paper and tape. *Proc. Natl. Acad. Sci. U.S.A.* **2008**, *105*, 19606-19611.
17. Martinez, A. W.; Phillips, S. T.; Whitesides, G. M.; Carrilho, E. Diagnostics for the Developing World: Microfluidic Paper-Based Analytical Devices. *Anal. Chem.* **2010**, *82*, 3-10.
18. Martinez, A. W.; Phillips, S. T.; Nie, Z. H.; Cheng, C. M.; Carrilho, E.; Wiley, B. J.; Whitesides, G. M. Programmable diagnostic devices made from paper and tape. *Lab Chip* **2010**, *10*, 2499-2504.
19. Liu, H.; Xiang, Y.; Lu, Y.; Crooks, R. M. Aptamer-Based Origami Paper Analytical Device for Electrochemical Detection of Adenosine. *Angew. Chem. Int. Ed.* **2012**, *51*, 6925-6928.
20. Wang, J. Electrochemical glucose biosensors. *Chem. Rev.* **2008**, *108*, 814-825.

21. Dungchai, W.; Chailapakul, O.; Henry, C. S. Electrochemical Detection for Paper-Based Microfluidics. *Anal. Chem.* **2009**, *81*, 5821-5826.
22. Nie, Z. H.; Deiss, F.; Liu, X. Y.; Akbulut, O.; Whitesides, G. M. Integration of paper-based microfluidic devices with commercial electrochemical readers. *Lab Chip* **2010**, *10*, 3163-3169.
23. Chen, L.; Magliano, D. J.; Zimmet, P. Z. The worldwide epidemiology of type 2 diabetes mellitus-present and future perspectives. *Nat. Rev. Endocrinol.* **2012**, *8*, 228-236.
24. Heller, A.; Feldman, B. Electrochemical glucose sensors and their applications in diabetes management. *Chem. Rev.* **2008**, *108*, 2482-2505.
25. Nathan, D. M.; Turgeon, H.; Regan, S. Relationship between glycated haemoglobin levels and mean glucose levels over time. *Diabetologia* **2007**, *50*, 2239-2244.
26. Krishnamurti, U.; Steffes, M. W. Glycohemoglobin: A primary predictor of the development or reversal of complications of diabetes mellitus. *Clin. Chem.* **2001**, *47*, 1157-1165.
27. Zinman, B.; Gerich, J.; Buse, J. B.; Lewin, A.; Schwartz, S.; Raskin, P.; Hale, P. M.; Zdravkovic, M.;

- Blonde, L. Standards of medical care in diabetes-2010
Diabetes Care **2010**, *33*, s4-s10.
28. Adamczyk, M.; Chen, Y. Y.; Johnson, D. D.; Mattingly, P. G.; Moore, J. A.; Pan, Y.; Reddy, R. E.
Chemiluminescent acridinium-9-carboxamide boronic acid probes: Application to a homogenous glycated hemoglobin assay. *Bioorg. Med. Chem. Lett.* **2006**, *16*, 1324-1328.
29. Frantzen, F.; Grimsrud, K.; Heggli, D. E.; Faaren, A. L.; Lovli, T.; Sundrehagen, E. Glycohemoglobin filter assay for doctors' offices based on boronic acid affinity principle. *Clin. Chem.* **1997**, *43*, 2390-2396.
30. Psotova, J.; Janiczek, O. Boronate Affinity-Chromatography and the Applications. *Chem. Listy* **1995**, *89*, 641-648.
31. Eckerbom, S.; Bergqvist, Y.; Jeppsson, J. O. Improved Method for Analysis of Glycated Hemoglobin by Ion-Exchange Chromatography. *Ann. Clin. Biochem.* **1994**, *31*, 355-360.
32. Jenkins, M.; Ratnaike, S. Capillary electrophoresis of hemoglobin. *Clin. Chem. Lab. Med.* **2003**, *41*, 747-754.
33. Blincko, S.; Edwards, R. Non-separation assay for glycohemoglobin. *Clin. Chem.* **1998**, *44*, 1302-1308.
34. Frantzen, F.; Grimsrud, K.; Heggli, D. E.; Sundrehagen, E. Soluble highly coloured phenylboronic acids and

- _____. *Clin. Chim. Acta* **1997**, *263*, 207-224.
35. Park, J. Y.; Chang, B. Y.; Nam, H.; Park, S. M.
Selective Electrochemical Sensing of Glycated Hemoglobin (HbA(1c)) on Thiophene-3-Boronic Acid Self-Assembled Monolayer Covered Gold Electrodes. *Anal. Chem.* **2008**, *80*, 8035-8044.
36. Son, S. U.; Seo, J. H.; Choi, Y. H.; Lee, S. S.
Fabrication of a disposable biochip for measuring percent hemoglobin Alc (%HbAlc). *Sens. Actuators, A* **2006**, *130*, 267-272.
37. Chang, B. Y.; Chow, K. F.; Crooks, J. A.; Mavre, F.; Crooks, R. M. Two-channel microelectrochemical bipolar electrode sensor array. *Analyst* **2012**, *137*, 2827-2833.
38. Qu, L.; Xia, S. H.; Bian, C.; Sun, J. Z.; Han, J. H. A micro-potentiometric hemoglobin immunosensor based on electropolymerized polypyrrole-gold nanoparticles composite. *Biosens. Bioelectron.* **2009**, *24*, 3419-3424.
39. Liu, S. Q.; Wollenberger, U.; Katterle, M.; Scheller, F. W. Ferroceneboronic acid-based amperometric biosensor for glycated hemoglobin. *Sens. Actuators, B* **2006**, *113*, 623-629.
40. Ikeda, K.; Sakamoto, Y.; Kawasaki, Y.; Miyake, T.; Tanaka, K.; Urata, T.; Katayama, Y.; Ueda, S.; Horiuchi,

- S. Determination of glycated albumin by enzyme-linked boronate immunoassay (ELBIA). *Clin. Chem.* **1998**, *44*, 256-263.
41. Metus, P.; Ruzzante, N.; Bonvicini, P.; Meneghetti, M.; Zaninotto, M.; Plebani, M. Immunoturbidimetric assay of glycated hemoglobin. *J. Clin. Lab. Anal.* **1999**, *13*, 5-8.
42. Lenters-Westra, E.; Slingerland, R. J. Six of Eight Hemoglobin A(1c) Point-of-Care Instruments Do Not Meet the General Accepted Analytical Performance Criteria. *Clin. Chem.* **2010**, *56*, 44-52.
43. Whitesides, G. M. The origins and the future of microfluidics. *Nature* **2006**, *442*, 368-373.
44. Weibel, D. B.; Whitesides, G. M. Applications of microfluidics in chemical biology. *Curr. Opin. Chem. Biol.* **2006**, *10*, 584-591.
45. Thorsen, T.; Roberts, R. W.; Arnold, F. H.; Quake, S. R. Dynamic pattern formation in a vesicle-generating microfluidic device. *Phys. Rev. Lett.* **2001**, *86*, 4163-4166.
46. Song, H.; Tice, J. D.; Ismagilov, R. F. A microfluidic system for controlling reaction networks in time. *Angew. Chem. Int. Ed.* **2003**, *42*, 768-772.

47. Chiu, D. T.; Lorenz, R. M.; Jeffries, G. D. M. Droplets for Ultrasmall-Volume Analysis. *Anal. Chem.* **2009**, *81*, 5111-5118.
48. Huebner, A.; Sharma, S.; Srisa-Art, M.; Hollfelder, F.; Edel, J. B.; Demello, A. J. Microdroplets: A sea of applications? *Lab Chip* **2008**, *8*, 1244-1254.
49. Song, H.; Ismagilov, R. F. Millisecond kinetics on a microfluidic chip using nanoliters of reagents. *J. Am. Chem. Soc.* **2003**, *125*, 14613-14619.
50. Song, H.; Chen, D. L.; Ismagilov, R. F. Reactions in droplets in microfluidic channels. *Angew. Chem. Int. Ed.* **2006**, *45*, 7336-7356.
51. Wu, D. P.; Zhao, B. X.; Dai, Z. P.; Qin, J. H.; Lin, B. C. Grafting epoxy-modified hydrophilic polymers onto poly(dimethylsiloxane) microfluidic chip to resist nonspecific protein adsorption. *Lab Chip* **2006**, *6*, 942-947.
52. Courtois, F.; Olguin, L. F.; Whyte, G.; Theberge, A. B.; Huck, W. T. S.; Hollfelder, F.; Abell, C. Controlling the Retention of Small Molecules in Emulsion Microdroplets for Use in Cell-Based Assays. *Anal. Chem.* **2009**, *81*, 3008-3016.
53. Huebner, A.; Srisa-Art, M.; Holt, D.; Abell, C.; Hollfelder, F.; Demello, A. J.; Edel, J. B.

- Quantitative detection of protein expression in single cells using droplet microfluidics. *Chem. Commun.* **2007**, *12*, 1218-1220.
54. Cristobal, G.; Arbouet, L.; Sarrazin, F.; Talaga, D.; Bruneel, J. L.; Joanicot, M.; Servant, L. On-line laser Raman spectroscopic probing of droplets engineered in microfluidic devices. *Lab Chip* **2006**, *6*, 1140-1146.
55. Strehle, K. R.; Cialla, D.; Rosch, P.; Henkel, T.; Kohler, M.; Popp, J. A reproducible surface-enhanced Raman spectroscopy approach. Online SERS measurements in a segmented microfluidic system. *Anal. Chem.* **2007**, *79*, 1542-1547.
56. Fidalgo, L. M.; Whyte, G.; Ruotolo, B. T.; Benesch, J. L. P.; Stengel, F.; Abell, C.; Robinson, C. V.; Huck, W. T. S. Coupling Microdroplet Microreactors with Mass Spectrometry: Reading the Contents of Single Droplets Online. *Angew. Chem. Int. Ed.* **2009**, *48*, 3665-3668.
57. Kelly, R. T.; Page, J. S.; Marginean, I.; Tang, K. Q.; Smith, R. D. Dilution-Free Analysis from Picoliter Droplets by Nano-Electrospray Ionization Mass Spectrometry. *Angew. Chem. Int. Ed.* **2009**, *48*, 6832-6835.
58. Han, Z. Y.; Li, W. T.; Huang, Y. Y.; Zheng, B. Measuring Rapid Enzymatic Kinetics by Electrochemical

-
- Pneumatic Valves. *Anal. Chem.* **2009**, *81*, 5840-5845.
59. Liu, S. J.; Gu, Y. F.; Le Roux, R. B.; Matthews, S. M.; Bratton, D.; Yunus, K.; Fisher, A. C.; Huck, W. T. S. The electrochemical detection of droplets in microfluidic devices. *Lab Chip* **2008**, *8*, 1937-1942.
60. Sassa, F.; Laghzali, H.; Fukuda, J.; Suzuki, H. Coulometric Detection of Components in Liquid Plugs by Microfabricated Flow Channel and Electrode Structures. *Anal. Chem.* **2010**, *82*, 8725-8732.
61. Bard, A. J.; Faulkner, L. R. *Electrochemical Methods: Fundamentals and Applications*; 2nd edn ed. John Wiley & Sons, Inc.: New York, 2001.
62. Han, Z. Y.; Chang, Y. Y.; Au, S. W. N.; Zheng, B. Measuring rapid kinetics by a potentiometric method in droplet-based microfluidic devices. *Chem. Commun.* **2011**, *48*, 1601-1603.
63. Xia, Y. N.; Rogers, J. A.; Paul, K. E.; Whitesides, G. M. Unconventional methods for fabricating and patterning nanostructures. *Chem. Rev.* **1999**, *99*, 1823-1848.
64. Williams, K. R.; Gupta, K.; Wasilik, M. Etch rates for micromachining processing - Part II. *J. Microelectromech. Syst.* **2003**, *12*, 761-778.

65. Unger, M. A.; Chou, H. P.; Thorsen, T.; Scherer, A.; Quake, S. R. Monolithic microfabricated valves and pumps by multilayer soft lithography. *Science* **2000**, *288*, 113-116.
66. Kartalov, E. P.; Walker, C.; Taylor, C. R.; Anderson, W. F.; Scherer, A. Microfluidic vias enable nested bioarrays and autoregulatory devices in Newtonian fluids. *Proc. Natl. Acad. Sci. U.S.A.* **2006**, *103*, 12280-12284.
67. Martinez, A. W.; Phillips, S. T.; Wiley, B. J.; Gupta, M.; Whitesides, G. M. FLASH: A rapid method for prototyping paper-based microfluidic devices. *Lab Chip* **2008**, *8*, 2146-2150.
68. Nie, Z. H.; Nijhuis, C. A.; Gong, J. L.; Chen, X.; Kumachev, A.; Martinez, A. W.; Narovlyansky, M.; Whitesides, G. M. Electrochemical sensing in paper-based microfluidic devices. *Lab Chip* **2010**, *10*, 477-483.
69. Cheng, C. M.; Martinez, A. W.; Gong, J. L.; Mace, C. R.; Phillips, S. T.; Carrilho, E.; Mirica, K. A.; Whitesides, G. M. Paper-Based ELISA. *Angew. Chem. Int. Ed.* **2010**, *49*, 4771-4774.
70. Osborn, J. L.; Lutz, B.; Fu, E.; Kauffman, P.; Stevens, D. Y.; Yager, P. Microfluidics without pumps:

-
- Lab Chip* **2010**, *10*, 2659-2665.
71. Siegel, A. C.; Phillips, S. T.; Dickey, M. D.; Lu, N. S.; Suo, Z. G.; Whitesides, G. M. Foldable Printed Circuit Boards on Paper Substrates. *Adv. Funct. Mater.* **2010**, *20*, 28-35.
72. Bell, P. J. L.; Karuso, P. Epicocconone, a novel fluorescent compound from the fungus *Epicoccum nigrum*. *J. Am. Chem. Soc.* **2003**, *125*, 9304-9305.
73. Wang, J. Portable electrochemical systems. *Trends Anal. Chem.* **2002**, *21*, 226-232.
74. Katz, E.; Buckmann, A. F.; Willner, I. Self-powered enzyme-based biosensors. *J. Am. Chem. Soc.* **2001**, *123*, 10752-10753.
75. Germain, M. N.; Arechederra, R. L.; Minter, S. D. Nitroaromatic Actuation of Mitochondrial Bioelectrocatalysis for Self-Powered Explosive Sensors. *J. Am. Chem. Soc.* **2008**, *130*, 15272-+.
76. Zaccaro, B. A.; Crooks, R. M. Self-Powered Sensor for Naked-Eye Detection of Serum Trypsin. *Anal. Chem.* **2011**, *83*, 1185-1188.
77. Xiang, Y.; Lu, Y. Using personal glucose meters and functional DNA sensors to quantify a variety of analytical targets. *Nat. Chem.* **2011**, *3*, 697-703.

78. Hu, L. B.; Choi, J. W.; Yang, Y.; Jeong, S.; La Mantia, F.; Cui, L. F.; Cui, Y. Highly conductive paper for energy-storage devices. *Natl. Acad. Sci. U.S.A.* **2009**, *106*, 21490-21494.
79. Hilder, M.; Winther-Jensen, B.; Clark, N. B. Paper-based, printed zinc-air battery. *J. Power Sources* **2009**, *194*, 1135-1141.
80. Itaya, K.; Ataka, T.; Toshima, S. Spectroelectrochemistry and Electrochemical Preparation Method of Prussian Blue Modified Electrodes. *J. Am. Chem. Soc.* **1982**, *104*, 4767-4772.
81. Lee, K. B. Urine-activated paper batteries for biosystems. *J. Micromech. Microeng.* **2005**, *15*, S210-S214.
82. Lee, K. B. Two-step activation of paper batteries for high power generation: design and fabrication of biofluid- and water-activated paper batteries. *J. Micromech. Microeng.* **2006**, *16*, 2312-2317.
83. Araújo, A. C.; Song, Y. J.; Lundeborg, J.; Stahl, B. L.; Brumer, H. Activated Paper Surfaces for the Rapid Hybridization of DNA through Capillary Transport. *Anal. Chem.* **2012**, *84*, 3311-3317.
84. Liu, J. W.; Cao, Z. H.; Lu, Y. Functional Nucleic Acid Sensors. *Chem. Rev.* **2009**, *109*, 1948-1998.

85. Cho, E. J.; Lee, J. W.; Ellington, A. D., *Annu. Rev. Anal. Chem.*, in c. 2009. p. 241-264.
86. Navani, N. K.; Li, Y. F. Nucleic acid aptamers and enzymes as sensors. *Curr. Opin. Chem. Biol.* **2006**, *10*, 272-281.
87. Willner, I.; Shlyahovsky, B.; Zayats, M.; Willner, B. DNAzymes for sensing, nanobiotechnology and logic gate applications. *Chem. Soc. Rev.* **2008**, *37*, 1153-1165.
88. Lubin, A. A.; Plaxco, K. W. Folding-Based Electrochemical Biosensors: The Case for Responsive Nucleic Acid Architectures. *Acc. Chem. Res.* **2010**, *43*, 496-505.
89. Liu, J. W.; Mazumdar, D.; Lu, Y. A simple and sensitive "dipstick" test in serum based on lateral flow separation of aptamer-linked nanostructures. *Angew. Chem. Int. Ed.* **2006**, *45*, 7955-7959.
90. Su, S. X.; Ali, M.; Filipe, C. D. M.; Li, Y. F.; Pelton, R. Microgel-based inks for paper-supported biosensing applications. *Biomacromolecules* **2008**, *9*, 935-941.
91. Davies, R. J.; Eapen, S. S.; Carlisle, S. J., *Lateral-Flow Immunochromatographic Assays*, in *Handbook of Biosensors and Biochips*. 2008, John Wiley & Sons, Ltd.

92. Noh, H.; Phillips, S. T. Fluidic Timers for Time-Dependent, Point-of-Care Assays on Paper. *Anal. Chem.* **2010**, *82*, 8071-8078.
93. Fu, E.; Lutz, B.; Kauffman, P.; Yager, P. Controlled reagent transport in disposable 2D paper networks. *Lab Chip* **2010**, *10*, 918-920.
94. Lutz, B. R.; Trinh, P.; Ball, C.; Fu, E.; Yager, P. Two-dimensional paper networks: programmable fluidic disconnects for multi-step processes in shaped paper. *Lab Chip* **2011**, *11*, 4274-4278.
95. Vella, S. J.; Beattie, P.; Cademartiri, R.; Laromaine, A.; Martinez, A. W.; Phillips, S. T.; Mirica, K. A.; Whitesides, G. M. Measuring Markers of Liver Function Using a Micropatterned Paper Device Designed for Blood from a Fingertstick. *Anal. Chem.* **2012**, *84*, 2883-2891.
96. Schilling, K. M.; Lepore, A. L.; Kurian, J. A.; Martinez, A. W. Fully Enclosed Microfluidic Paper-Based Analytical Devices. *Anal. Chem.* **2012**, *84*, 1579-1585.
97. Fenton, E. M.; Mascarenas, M. R.; Lopez, G. P.; Sibbett, S. S. Multiplex Lateral-Flow Test Strips Fabricated by Two-Dimensional Shaping. *ACS Appl. Mater. Interfaces* **2009**, *1*, 124-129.

98. Liu, H.; Crooks, R. M. Three-Dimensional Paper Microfluidic Devices Assembled Using the Principles of Origami. *J. Am. Chem. Soc.* **2011**, *133*, 17564-17566.
99. Liu, H.; Crooks, R. M. Paper-Based Electrochemical Sensing Platform with Integral Battery and Electrochromic Read-Out. *Anal. Chem.* **2012**, *84*, 2528-2532.
100. Huizenga, D. E.; Szostak, J. W. A DNA Aptamer That Binds Adenosine and Atp. *Biochemistry* **1995**, *34*, 656-665.
101. Nutiu, R.; Li, Y. F. Structure-switching signaling aptamers. *J. Am. Chem. Soc.* **2003**, *125*, 4771-4778.
102. Vallon, V.; Muhlbauer, B.; Osswald, H. Adenosine and kidney function. *Physiol. Rev.* **2006**, *86*, 901-940.
103. *iMultimeter By HMB-TEC*. 2011, Apple.com.
104. Wang, Y.; Hamasaki, K.; Rando, R. R. Specificity of aminoglycoside binding to RNA constructs derived from the 16S rRNA decoding region and the HIV-RRE activator region. *Biochemistry* **1997**, *36*, 768-779.
105. Schumacher, S.; Nagel, T.; Scheller, F. W.; Gajovic-Eichelmann, N. Alizarin Red S as an electrochemical indicator for saccharide recognition. *Electrochim. Acta* **2011**, *56*, 6607-6611.

106. Springsteen, G.; Wang, B. H. A detailed examination of boronic acid-diol complexation. *Tetrahedron* **2002**, *58*, 5291-5300.
107. Turcanu, A.; Bechtold, T. pH Dependent redox behaviour of Alizarin Red S (1,2-dihydroxy-9,10-anthraquinone-3-sulfonate) - Cyclic voltammetry in presence of dispersed vat dye. *Dyes Pigm.* **2011**, *91*, 324-331.
108. Shoji, E.; Freund, M. S. Potentiometric saccharide detection based on the pKa changes of poly(aniline boronic acid). *J. Am. Chem. Soc.* **2002**, *124*, 12486-12493.
109. Pearson, T. C. Normal ranges for packed cell volume and haemoglobin concentration in adults: Relevance to "apparent polycythaemia" (vol 67, pg 56, 2001). *Eur. J. Haematol.* **2001**, *67*, 203-204.
110. Stadie, W. C. A method for the determination of methemoglobin in whole blood. *J. Biol. Chem.* **1920**, *41*, 237-241.
111. Tice, J. D.; Song, H.; Lyon, A. D.; Ismagilov, R. F. Formation of droplets and mixing in multiphase microfluidics at low values of the Reynolds and the capillary numbers. *Langmuir* **2003**, *19*, 9127-9133.
112. McDonald, J. C.; Duffy, D. C.; Anderson, J. R.; Chiu, D. T.; Wu, H. K.; Schueller, O. J. A.; Whitesides, G. M.

- Fabrication of microfluidic systems in poly(dimethylsiloxane). *Electrophoresis* **2000**, *21*, 27-40.
113. Anand, R. K.; Sheridan, E.; Knust, K. N.; Crooks, R. M. Bipolar Electrode Focusing: Faradaic Ion Concentration Polarization. *Anal.Chem.* **2011**, *83*, 2351-2358.
114. Chen, D.; Du, W. B.; Liu, Y.; Liu, W. S.; Kuznetsov, A.; Mendez, F. E.; Philipson, L. H.; Ismagilov, R. F. The chemistode: A droplet-based microfluidic device for stimulation and recording with high temporal, spatial, and chemical resolution. *Proc. Natl. Acad. Sci. U. S. A.* **2008**, *105*, 16843-16848.
115. Polk, B. J.; Stelzenmuller, A.; Mijares, G.; MacCrehan, W.; Gaitan, M. Ag/AgCl microelectrodes with improved stability for microfluidics. *Sens. Actuators, B* **2006**, *114*, 239-247.
116. Kenis, P. J. A.; Ismagilov, R. F.; Takayama, S.; Whitesides, G. M.; Li, S. L.; White, H. S. Fabrication inside microchannels using fluid flow. *Acc. Chem. Res.* **2000**, *33*, 841-847.
117. Garstecki, P.; Fuerstman, M. J.; Stone, H. A.; Whitesides, G. M. Formation of droplets and bubbles in a microfluidic T-junction - scaling and mechanism of break-up. *Lab Chip* **2006**, *6*, 437-446.

118. Theberge, A. B.; Courtois, F.; Schaerli, Y.; Fischlechner, M.; Abell, C.; Hollfelder, F.; Huck, W. T. S. Microdroplets in Microfluidics: An Evolving Platform for Discoveries in Chemistry and Biology. *Angew. Chem. Int. Ed.* **2010**, *49*, 5846-5868.
119. Levich, V. G. *Physicochemical Hydrodynamics*. Prentice-Hall: Englewood Cliffs, NJ, 1962.
120. Ye, H. C.; Crooks, R. M. Electrocatalytic O₂ reduction at glassy carbon electrodes modified with dendrimer-encapsulated Pt nanoparticles. *J. Am. Chem. Soc.* **2005**, *127*, 4930-4934.
121. Bode, D. D.; Andersen, T. N.; Eyring, H. Anion and pH effects on the potentials of zero charge of gold and silver electrodes. *J. Phys. Chem.* **1967**, *71*, 792-797.
122. Pollack, M. G.; Shenderov, A. D.; Fair, R. B. Electrowetting-based actuation of droplets for integrated microfluidics. *Lab Chip* **2002**, *2*, 96-101.
123. Burdeniuc, J.; Crabtree, R. H. Catalytic photodefluorination of perfluoroalkanes to perfluoroalkenes with a ferrocene photosensitizer. *Organometallics* **1998**, *17*, 1582-1586.
124. Rhee, M.; Burns, M. A. Drop mixing in a microchannel for lab-on-a-chip platforms. *Langmuir* **2008**, *24*, 590-601.

Vita

Hong Liu received his Bachelor of Science and Master of Science degrees from Nanjing University, China in 2006 and 2009. He is expected to receive his doctoral of philosophy degree in Chemistry under the guidance of Professor Richard M. Crooks from The University of Texas at Austin in December 2012.

Permanent address: Room 302, Building 2, 21 Jiuhuashan,
Nanjing, Jiangsu 210008, China

This dissertation was typed by Hong Liu.